

Synthesis, Characterization, and Spectroscopy of Lanthanide-Doped Inorganic
Nanocrystals; Radiant Flux and Absolute Quantum Yield Measurements of
Upconversion Nanocrystals, and Fabrication of a Fiber-Optic Radiation Detector
Utilizing Synthetically Optimized, Linearly Responsive Nanoscintillators

by

Ian Nicholas Stanton

Department of Chemistry
Duke University

Date: _____

Approved: _____

Michael J. Therien, Supervisor

David N. Beratan

Martin C. Fischer

Tuan Vo-Dinh

Dissertation submitted in partial fulfillment of
the requirements for the degree of Doctor
of Philosophy in the Department of
Chemistry in the Graduate School
of Duke University

2013

ABSTRACT

Synthesis, Characterization, and Spectroscopy of Lanthanide-Doped Inorganic
Nanocrystals; Radiant Flux and Absolute Quantum Yield Measurements of
Upconversion Nanocrystals, and Fabrication of a Fiber-Optic Radiation Detector
Utilizing Synthetically Optimized, Linearly Responsive Nanoscintillators

by

Ian Nicholas Stanton

Department of Chemistry
Duke University

Date: _____
Approved: _____

Michael J. Therien, Supervisor

David N. Beratan

Martin C. Fischer

Tuan Vo-Dinh

An abstract of a dissertation submitted in partial
fulfillment of the requirements for the degree
of Doctor of Philosophy in the Department of
Chemistry in the Graduate School of
Duke University

2013

Copyright by
Ian Nicholas Stanton
2013

Abstract

The ability to interrogate structure-function photophysical properties on lanthanide-doped nanoscale materials will define their utility in next-generation applications and devices that capitalize on their size, light-conversion efficiencies, emissive wavelengths, syntheses, and environmental stabilities. The two main topics of this dissertation are (i) the interrogation of laser power-dependent quantum yield and total radiant flux metrics for a homogeneous, solution phase upconversion nanocrystal composition under both continuous wave and femtosecond-pulsed excitation utilizing a custom engineered absolute measurement system, and (ii) the synthesis, characterization, and power-dependent x-ray excited scintillation properties of $[\text{Y}_2\text{O}_3;\text{Eu}]$ nanocrystals, and their integration into a fiber-optic radiation sensing device capable of *in vivo* dosimetry.

Presented herein is the laser power-dependent total radiant flux and absolute quantum yield measurements of homogeneous, solution-phase $[\text{NaYF}_4;\text{Yb (15\%), Er (2\%)}]$ upconversion nanocrystals, and further compares the quantitative total radiant flux and absolute quantum yield measurements under both 970 nm continuous-wave and 976 nm pulsed Ti-Sapphire laser excitation (140 fs pulse-width, 80 MHz). This study demonstrates that at comparable excitation densities under continuous-wave and fs-pulsed excitation from 42 - 284 W/cm^2 , the absolute quantum yield is higher under fs-pulsed laser excitation, whereas the total radiant flux is higher under continuous-wave excitation, when spectra are integrated over the 500 - 700 nm wavelength regime. This study further establishes the radiant flux as the true unit of merit for quantifying emissive output intensity of upconverting nanocrystals for application purposes, especially given the high uncertainty in solution phase upconversion nanocrystal

quantum yield measurements due to their low absorption cross-section. Additionally, a commercially available bulk $[\text{NaYF}_4; \text{Yb (20\%), Er (3\%)}]$ upconversion sample was measured in the solid-state to provide a total radiant flux and absolute quantum yield standard. The measurements were accomplished utilizing a custom-engineered, multi-detector integrating sphere measurement system that can measure spectral sample emission in Watts on a flux-calibrated (W/nm) CCD-spectrometer, enabling the direct measurement of the total radiant flux without need for an absorbance or quantum yield value.

Also presented is the development and characterization of a scintillating nanocrystalline composition, $[\text{Y}_{2-x}\text{O}_3; \text{Eu}_x, \text{Li}_y]$, in which Eu and Li dopant ion concentrations were systematically varied in order to define the most emissive compositions under specific x-ray excitation conditions. It is shown that these optimized $[\text{Y}_{2-x}\text{O}_3; \text{Eu}_x, \text{Li}_y]$ compositions display scintillation responses that: (i) correlate linearly with incident radiation exposure at x-ray energies spanning from 40 - 220 kVp, and (ii) manifest no evidence of scintillation intensity saturation at the highest evaluated radiation exposures [up to 4 Roentgen per second]. X-ray excitation energies of 40, 120, and 220 kVp were chosen to probe the dependence of the integrated emission intensity upon x-ray exposure-rate in energy regimes where either the photoelectric or the Compton effect governs the scintillation mechanism on the most emissive $[\text{Y}_{2-x}\text{O}_3; \text{Eu}_x, \text{Li}_y]$ composition, $[\text{Y}_{1.9}\text{O}_3; \text{Eu}_{0.1}, \text{Li}_{0.16}]$. These experiments demonstrate for nanoscale $[\text{Y}_{2-x}\text{O}_3; \text{Eu}_x]$, that for comparable radiation exposures, when scintillation is governed by the photoelectric effect (120 kVp excitation), greater integrated emission intensities are recorded relative to excitation energies where the Compton effect regulates scintillation (220 kVp excitation).

The nanoscale $[\text{Y}_{1.9}\text{O}_3; \text{Eu}_{0.1}, \text{Li}_{0.16}]$ was further exploited as a detector material in a prototype fiber-optic radiation sensor. The scintillation intensity from a $[\text{Y}_{1.9}\text{O}_3; \text{Eu}_{0.1}, \text{Li}_{0.16}]$ -modified optical fiber tip, recorded using a CCD-photodetector or a Si-photodiode, was correlated with radiation exposure using a Precision XRAD 225Cx small-animal image guided radiation therapy (IGRT) system, an orthovoltage cabinet-irradiator, and a clinical X-ray Computed Tomography (CT) machine. For all x-ray energies tested from 80 - 225 kVp, this near-radiotransparent device recorded scintillation intensities that tracked linearly with total radiation exposure, highlighting its capability to provide alternately accurate dosimetry measurements for both diagnostic imaging and radiation therapy treatment. Because Si-based CCD and photodiode detectors manifest maximal sensitivities over the emission range of nanoscale $[\text{Y}_{1.9}\text{O}_3; \text{Eu}_{0.1}, \text{Li}_{0.16}]$, the timing speeds, sizes, and low power-consumption of these devices, coupled with the detection element's linear dependence of scintillation intensity with radiation dose, demonstrates the opportunity for next-generation radiation exposure measuring devices for *in/ex vivo* applications that are ultra-small, inexpensive, and accurate.

Dedication

To my parents and sister, who have supported me in all of life's endeavors in the pursuit of happiness, love, and education, and to my best friend and the love of my life, Jessica, for her everlasting companionship, love, encouragement, humor, and ability to make me smile even after the longest day, I will be eternally grateful.

Contents

Abstract.....	iv
List of Tables	xi
List of Figures	xii
Acknowledgements	xvi
1. Introduction to the Dissertation.....	1
1.1 Measuring Absolute Emissive Values of Upconverting Nanocrystals for Quantitative Comparison.....	2
1.1.1 Upconverting Nanocrystals and their Absolute Measurements.....	2
1.1.2 Motivation	5
1.1.3 Summary and Goals.....	6
1.2 Scintillating Nanocrystals and Their Integration Into Radiation Sensing Device Architectures	7
1.2.1 Scintillating Nanocrystals.....	7
1.2.2 Medical Dosimetry	9
1.2.3 Motivation	12
1.2.4 Summary and Goals.....	12
1.3. Additional Chapters.....	14
2. Power-Dependent Total Radiant Flux and Absolute Quantum Yield Measurements of Solution-Phase [NaYF ₄ ; Yb, Er] Upconversion Nanocrystals Under Continuous and Femtosecond-Pulsed Laser Excitation	17
2.1 Introduction.....	18
2.2 Experimental	23
2.3 Results and Discussion	29
2.4 Conclusions	42
3. Dual energy converting nano-phosphors: upconversion luminescence and X-ray excited scintillation from a single composition of lanthanide-doped yttrium oxide.....	45

3.1 Introduction.....	45
3.2 Experimental	47
3.3 Results and Discussion	50
3.4 Conclusion.....	57
4. A Fiber-Optic Radiation Detector Based on Europium-Doped Yttrium Oxide Nanocrystals that Provides a Linear Emissive Response to X-ray Radiation Exposure ..	59
4.1 Introduction.....	60
4.2 Experimental	61
4.3 Results and Discussion	64
4.4 Conclusion.....	73
5. Characterization of a Nano-Scintillator Terminated Fiber-Optic Dosimeter for <i>in vivo</i> Diagnostic and Radiation Therapy Dosimetry	76
5.1 Introduction.....	77
5.2 Experimental	81
5.3 Results	87
5.4 Discussion.....	93
5.5 Conclusion.....	95
Appendix A. Fluorescence and Raman Spectroscopy of Single-Walled Carbon Nanotubes Helically Wrapped by Ionic, Semiconducting Polymers In Different Dielectric and Electrophilic Environments.....	97
A.1 Introduction.....	97
A.2 Experimental	101
A.3 Results and Discussion	104
A.4 Conclusion.....	114
Appendix B. Establishing The Absolute Quantum Yield Efficiency of Free Base Tetraphenylporphyrin.....	116
B.1 Introduction	116

B.2 Experimental.....	121
B.3 Results and Discussion.....	125
B.4 Conclusion.....	129
References.....	130
Biography	140

List of Tables

Table 1: Absolute quantum yield and total radiant flux measurements of the as prepared and CW excited commercially available [NaYF ₄ : Yb (20%), Er (3%)] upconversion phosphor at 25 W/cm ² . This radiant flux was not converted to a volume as it was measured in the solid-state.....	32
Table 2: Theoretical amounts of precursors for [Y ₂ O ₃ ; Yb (2%), Er (1%)] based on a 25 mL solution.	47
Table 3: ICS-AES compositional analysis of the [Y ₂ O ₃ ; Eu _x], [Y ₂ O ₃ ; Eu _{0.1} , Li _y], and [Y ₂ O ₃ ; Li _y] samples, comparing the pre-combustion starting material predicted composition (theoretical) to the as-synthesized nanocrystal composition (actual). These data show that Eu ions are easily incorporated into the lattice with the anticipated stoichiometry; Li ion concentrations in the pre-combustion solution, however, exceed that found for the as-synthesized nanocrystals.	65
Table 4: Dose measurements and statistics from the tissue equivalent block phantom...	87
Table 5: Dose measurements and statistics from the tissue equivalent breast phantom.	89
Table 6: Dose measurements and statistics from the tissue equivalent body phantom in a clinical GE-VCT.	92
Table 7: Tabulated emission efficiencies (I/A) from the excitation (Ex (nm)) and emission (Em (nm)) peaks and their associated optical densities (A (OD)) and emission intensities (Em (I)). Data taken from the absorption spectra and two-dimensional excitation-emission mapping spectra.	108
Table 8: Solvent-dependent radial-breathing mode (RBM) frequency positions for the 785 nm resonant nanotubes in the PNES and SDS suspended SWNTs. The RBM peak positions show no significant RBM frequency shifts upon PNES wrapping of SWNTs compared to the benchmark SDS surfactant solution, and no further effect on the RBM vibrational frequencies with different solvent environments.	112
Table 9: Comparisons of quantum yield values of H ₂ TPP and other standard fluorophores in aerated solvent obtained in this study versus previous literature.	126
Table 10: H ₂ TPP absolute quantum yields from different excitation wavelengths in aerated benzene.	128

List of Figures

Figure 1: Notable upconversion mechanisms contributing to 540 nm centered $^2H_{11/2}/^4S_{3/2} \rightarrow ^4I_{15/2}$ and 670 nm centered $^4F_{9/2} \rightarrow ^4I_{15/2}$ radiative transitions in Er-Yb co-doped upconversion nanocrystals. 980 nm laser excitation populates the Yb³⁺ ion $^2F_{5/2}$ state, and the more weakly absorbing Er³⁺ $^4I_{11/2}$ state (solid vertical arrows); appropriately high laser fluences drive population of higher energy Er³⁺ excited states via processes that include Er³⁺ excited state absorption (ESA) (solid vertical arrows) and energy transfer upconversion (ETU) involving the electronically excited Yb³⁺ $^2F_{5/2}$ state (solid curved arrows) between energy-matched excited states of Er³⁺ and Yb³⁺. Phonon relaxations (wavy lines) result in populations at intermediate ($^4I_{13/2}$) and emitting ($^2H_{11/2}/^4S_{3/2}$) Er³⁺ excited states. Subsequent radiative transitions within the Er³⁺ *f*-block states produce green [$^2H_{11/2} \rightarrow ^4I_{15/2}$; $^4S_{3/2} \rightarrow ^4I_{15/2}$: 515 – 570 nm] and red [$^4F_{9/2} \rightarrow ^4I_{15/2}$: 645 – 690 nm] emission lines..... 3

Figure 2: X-ray excited emission (scintillation) stems from initial x-ray absorption, electron-hole (e⁻-h⁺) pair generation, subsequent valence and conduction band energy trapping and collection, and ensuing radiative emission from lanthanide *f*-block states lying within the valence and conduction band gap..... 8

Figure 3: (A) A machine press with the [NaYF₄: Yb (20%), Er (3%)] bulk powder sample placed in-between two pieces of weigh-paper (inset), and (B) an approximate 8 x 8 mm wafer cut and mounted in a 1 cm cuvette for absolute quantum yield and radiant flux measurements of the pressed [NaYF₄: Yb (20%), Er (3%)] bulk sample. 24

Figure 4: (A) Schematic representation of the three measurement methodology where purely the excitation laser (L_a), and the indirect (L_b) and direct (L_c) sample absorption and emission are measured, and (B) the sphere design viewing down from the top and to the side showing placement of the intensity calibrated lamp, power meter, CCD-spectrometer detector, and baffles to ensure photons bounce twice before being detected. (C) The absolute quantum yield and total radiant flux measurement system featuring an integrating sphere with a calibrated spectral flux lamp and a Germanium power meter, a fiber-coupled CCD spectrometer, and electronics necessary for the measurements (no lasers shown). 26

Figure 5: (A) TEM image of the [NaYF₄: Yb (15%), Er(2%)] nanocrystals, and the corresponding XRD trace confirming formation of the hexagonal phase. 29

Figure 6: Upconversion spectra acquired for both direct (L_c) and indirect (L_b) laser excitation of 28 nm diameter [NaYF₄: Yb (15%), Er (2%)] nanocrystals in toluene solution: (A) CW light source; (B) fs-pulsed light source (140 fs pulse-width, 80 MHz). Experimental conditions: laser power = 225 W / cm²; sample concentration = 1 mg / mL solution. (C) The absorbance value, A, plotted as a function of laser excitation type and power, with associated error bars..... 34

Figure 7: Contour plot of the emission intensity with respect to time and wavelength (A), lifetime fitting of the $^2H_{11/2} \rightarrow ^4I_{15/2}$ (510 - 525 nm), the $^4S_{3/2} \rightarrow ^4I_{15/2}$ (535 - 565 nm), and the

fully integrated $^2H_{11/2}/^4S_{3/2} \rightarrow ^4I_{15/2}$ (510 – 565 nm) transitions showing a rise-time of 62 μ s and decay time of 302 μ s (B) and the normalized overlap of the fitting traces (B, inset), and the lifetime fitting of the $^4F_{9/2} \rightarrow ^4I_{15/2}$ (645 – 680 nm) transition with a 161 μ s rise and 488 μ s decay lifetime. The raw data is presented by open shapes, with solid lines for the exponential fitting in B,C. 37

Figure 8: The absolute quantum yield and sample volume corrected total radiant flux under 970 nm CW and 976 nm fs-pulsed laser (140 fs pulse-width, 80 MHz) excitation of: (A, B) the $^2H_{11/2}/^4S_{3/2} \rightarrow ^4I_{15/2}$ luminescence integrated from 510 - 565 nm, (C, D) the $^4F_{9/2} \rightarrow ^4I_{15/2}$ luminescence integrated from 645 - 680 nm, and (E, F) the averaged quantum yield and total radiant flux results of the entire visible spectrum by addition of both the $^2H_{11/2}/^4S_{3/2} \rightarrow ^4I_{15/2}$ and $^4F_{9/2} \rightarrow ^4I_{15/2}$ transitions. Figures B,D have been fit with power law functions to highlight the number of photons responsible for each transition, while Figures A,C,E,F have added trend-lines to guide the eye. Figures E,F have error bars respective of the measurements' uncertainty. 39

Figure 9: X-ray diffraction patterns of Yb2Er1 (A), Yb2Er1Li5 (B) and Yb10Er1 (C). These spectra match the JCPDS-88-1040 Index for cubic yttrium oxide demonstrating all compositions are crystalline and cubic. 50

Figure 10: Exemplar SEM images of Yb2Er1 (A), Yb2Er1Li5 (B), and Yb10Er1 (C), highlighting the small, individualized nanocrystals as well as the micron sized “coral-like” structures present in all samples with and without lithium. 51

Figure 11: TEM images of Yb2Er1 (A) and Yb2Er1Li5 (B), showing how the micron-sized structures are actually composed of nanocrystallites. This further shows the effects of Li-doping, as the Yb2Er1Li5 nanocrystals feature larger size and better particle crystallinity than their Yb2Er1 parent structures. 53

Figure 12: (A) Solid-state UCL spectra of Yb2ErLi5, Yb2Er1, and Yb10Er1 nanocrystals excited at 980 nm (laser power = 400 W / cm²), and the power-dependent integrated upconversion luminescence intensity of (B) Yb2Er1, (C) Yb2Er1Li5, and (D) Yb10Er1 over the green [$^2H_{11/2} \rightarrow ^4I_{15/2}$; $^4S_{3/2} \rightarrow ^4I_{15/2}$: 515 – 570 nm] and red [$^4F_{9/2} \rightarrow ^4I_{15/2}$: 645 – 690 nm] centered emission lines. Yb2Er1 and Yb2Er1Li5 both display green (565 nm) and red (670 nm) centered emissions, with the lithium-doped composition nearly an order of magnitude more emissive. Yb10Er1 displays red (670 nm) centered emission near intensity of Yb2Er1Li5, but displays almost no green (565 nm) emission. 54

Figure 13: Solid-state x-ray excited scintillation (XES) spectra recorded for Yb2Er1Li5, Yb2Er1, and Yb10Er1 nanocrystals. Experimental conditions: x-ray source, 130 kVp (5 mA); T = 20 °C. 56

Figure 14: X-ray diffraction (XRD) spectra of the $[Y_{1.9}O_3; Eu_{0.1}, Li_y]$ compositions. All material compositions display the cubic phase, space group Ia $\bar{3}$, JCPDS-88-1040. 64

Figure 15: TEM images of $[Y_{1.9}O_3; Eu_{0.1}, Li_y]$ nanocrystals with increasing lithium-doping content. The amorphous content gradually disappears as Li ion concentration is

increased; with these increasing Li^+ concentrations, isolated nanoparticles feature larger diameters as well as more well-defined crystalline boundaries. 66

Figure 16: Raman spectra of $[\text{Y}_2\text{O}_3; \text{Li}_x]$ compositions acquired at a 632 nm irradiation wavelength. The increases in size and crystallinity observed in the TEM images as a function of increased Li concentration correlate with an observed increase in the Raman scattering intensity measured at 376 cm^{-1} 67

Figure 17: Integrated, solid-state x-ray emission spectral intensities determined over a 575 - 675 nm range for: (A) $[\text{Y}_2\text{O}_3; \text{Eu}_x]$ and (B) $[\text{Y}_{1.9}\text{O}_3; \text{Eu}_{0.1}, \text{Li}_y]$ compositions (note: trend lines added for visualization purposes). (C) The x-ray emission spectra of the most emissive Eu and Eu/Li co-doped samples, recorded for 130 kVp (5 mA) x-ray excitation. 68

Figure 18: Integrated solid-state x-ray emission spectral intensity recorded over the 500 - 700 nm range as a function of radiation exposure (R/s) for: (A) 40, (B) 120, and (C) 220 kVp excitation. 69

Figure 19: (A) A schematic of the sub-mm-sized optical fiber prototype dosimeter based on nanoscale $[\text{Y}_{1.9}\text{O}_3; \text{Eu}_{0.1}, \text{Li}_{0.16}]$. (B) An x-ray CT image acquired at 40 kVp, showing the optical fiber device adjacent to an ion-chamber radiation detector. (C) The linear scintillation intensity recorded by the device integrated over 605 - 617 nm that measures the total dose deposited at 80 kVp (imaging) and 225 kVp (therapy) energies. The CT image was acquired in a Precision XRAD 225Cx small-animal image guided radiation therapy (IGRT) system; the scintillation data were recorded using IGRT 80 and 225 kVp excitation. Note that all data points were measured in triplicate, and the standard deviation for a given data point was $< 0.9\%$. The inset of (C) shows that the device scintillation response tracks linearly with exposure to the highest levels tested (117.8 Roentgen at 225 kVp). 72

Figure 20: (A) A picture of the NS-FOD in front of the ion-chamber and (B) the calibration curve during Xrad320 calibration, and (C) a picture of the NS-FOD next to the ion-chamber and (D) the calibration curve during GE-VCT calibration. Both calibrations display a high level of linearity over the broad dose range that each x-ray machine is capable of producing. 84

Figure 21: An example of a real-time calibration plot for the Xrad320 (A) and GE-VCT (B), from which a linear slope of the intensities can be correlated to a dose. 86

Figure 22: The 150 mm x 150 mm x 25 mm tissue equivalent block with the ion-chamber, MOSFET, and NS-FOD inserted at the same relative depth, and (B) the 300 cc breast phantom with the MOSFET and NS-FOD inserted at the same location. 87

Figure 23: (A) The ATOM adult male anthropomorphic phantom placed on the GE-VCT bed, and close-up images of the parallel (B) and perpendicular (C) placements of the NS-FOD, holding constant the ion-chamber parallel to the bed. 91

Figure 24: Real-time data acquisition during with the NS-FOD placed parallel to the ion-chamber on the body phantom, comparing scintillation power (W) to time (s). The

timing resolution of the NS-FOD enables dose monitoring as the x-ray tube circles the body multiple times, evinced by the two sharp peaks in the original data plot highlighted in the yellow region.....	91
Figure 25: Exemplar Lorentzian fitting of the SWNT radial breathing modes of the PNES-SWNT sample in methanol (PNES-MeOH). The upper plot shows the quality of the fit line (blue) to the recorded data (red) with a linear background baseline (green). The bottom plot shows the individual SWNT radial breath mode fits, whose peak position was utilized for the comparison.	103
Figure 26: Absorption spectra of the original and re-suspended PNES-SWNT samples used for the two-dimensional excitation-emission mapping.	104
Figure 27: Two-dimensional excitation-emission contour plot mapping of (A) origD ₂ O, (B) resD ₂ O, (C) resMeOH, and (D) resDMSO. Individual SWNT species are labeled directly below their peak excitation-emission band. Samples were measured in standard T-geometry luminescence in 3x3 mm cells at room temperature (25 degrees Celsius)..	106
Figure 28: Relative emission efficiencies of the (7,5), (8,4), (7,6), (9,4), (9,5), and (8,7) PNES-SWNTs from the origD ₂ O, resD ₂ O, resMeOH, and resDMSO samples plotted as a function of (A) the solvent dielectric constant and (B) the solvent acceptor number. The solid lines in both plots are guides for the eye.	109
Figure 29: Raman spectra of directly solvent-suspended PNES-SWNTs in D ₂ O:DMF (PNES-D ₂ O:DMF), DMSO (PNES-DMSO), and methanol (PNES-MeOH). SDS-surfactant-suspended SWNTs (SDS-D ₂ O) are also shown and used as the benchmark standard to correlate the radial-breathing mode vibrational frequencies.	112
Figure 30: Schematic diagram of the Hamamatsu absolute quantum yield measurement system.	122
Figure 31: Representative set of measurements for H ₂ TPP excited at 546 nm. The OD at 546 nm of each sample is listed in the plot. The 600 - 800 nm range has been magnified to easily see the emission and show its decrease in intensity as the concentration decreases. Note that the sample absorption is also evident at 546 nm, as the sample concentration increases, the intensity of light at 546 nm decreases.....	124
Figure 32: The representative ground state absorption (dashed line) and emission (solid line) spectra synthesized for this study, as well as the molecular structure of H ₂ TPP. The fluorescence spectra were obtained by 546 nm excitation of the Q _y (0,0) band. The absorption of the Q band region has been magnified by 15 times to show the distinct structure of each Q band.....	125
Figure 33: Representative absolute quantum yield measurement of H ₂ TPP excited at 546 nm. The OD at the excitation wavelength was 0.018. The absorption of H ₂ TPP at the excitation peak can clearly be seen in the difference of the reference (just benzene solvent) versus the sample, and the region from 600 – 800 nm has been magnified (x 100) to easily see the H ₂ TPP emission with respect to the background. The high sensitivity of the BT-CCD makes this measurement possible well into the near-infrared.	127

Acknowledgements

Firstly, I would like to acknowledge my advisor, Dr. Michael J. Therien, for giving me the opportunity to conduct the research presented herein under his direction, and for his commitment to the betterment of myself as a scientist, researcher, and person. I especially thank him for the freedom to work within the presented subject areas, and his continued enthusiasm in my pursuit of scientific and personal discovery.

I would like to also acknowledge Dr. Terry T. Yoshizumi for his expertise, interest, and camaraderie in my work towards engineering radiation sensors and dosimeters.

I am very fortunate to have had discussions with Duke Professors contributing to my various research topics, and would like to thank committee members Dr. David Beratan, Dr. Tuan Vo-Dinh, and Dr. Martin Fischer, as well as Dr. David Kirsch, Dr. Barry Myers, Dr. Mark Dewhirst, and Dr. Warren Warren, who all have been more than willing to offer me guidance and support throughout my stay at Duke. I would also like to thank former undergraduate professors Dr. Bret Findley, Dr. Kathleen Mondanaro, Dr. Alain Brizard, Dr. Josh Van Houten, Jennifer Paone-Vogt and Dr. Alayne Schroll from St. Michael's College, who pushed me to strive for academic excellence and provided me the educational foundation to succeed in graduate school.

I would finally like to thank my colleagues Joshua T. Stecher, Dr. Jennifer A. Ayres, Mary G. Glesner, and Matthew D. Belley, who have helped me acquire the skills and knowledge needed to pursue my research goals, and provided collaborative support and friendship during my graduate work. I would also like to thank all of the Therien Group members and personnel I have encountered, as each has made a lasting impression on my scientific and personal life.

1. Introduction to the Dissertation

The design, synthesis, characterization, and interrogation of materials that display unique and advantageous light-based properties has long intrigued scientists in almost every field. The ability of certain materials to generate light under various types of electrical, chemical, or optical stimulation over specific wavelength regimes of interest has had significant impact on every facet of modern day life, from lighting to medical imaging to electronics. My interest in material-based light-interactions started early on in my scientific career, having the opportunity to conduct undergraduate research on the absorption properties of weak electron-donor-acceptor complexes, as well as having a substantial interest in material physics. It was then that I realized my true curiosities in science: how materials generate and interact with light, and how best to measure and utilize their associated response. I also realized then that I wanted to work on research projects that have a direct route to applications, where the design and development of the materials, instruments, or subsequent devices could positively impact scientific discovery, measurement, or human life through their implementation. The work presented in this dissertation combines all of my above interests and goals for providing novel materials, devices, and instruments to better understand and utilize photophysical properties of rare-earth (lanthanide) doped inorganic nanocrystals.

The two main topics of this dissertation are (i) the interrogation of laser power-dependent quantum yield and total radiant flux metrics for a homogeneous, solution phase upconversion nanocrystal composition under both continuous wave and femtosecond-pulsed excitation utilizing a custom engineered absolute measurement system, and (ii) the synthesis, characterization, and power-dependent x-ray excited scintillation properties of $[\text{Y}_2\text{O}_3; \text{Eu}]$ nanocrystals, and their integration into a fiber-optic radiation sensing device capable of *in vivo* dosimetry. Both of these topics will be

introduced below from their respective chapters to give an overview of the highlighted work contained herein.

1.1 Measuring Absolute Emissive Values of Upconverting Nanocrystals for Quantitative Comparison

1.1.1 Upconverting Nanocrystals and their Absolute Measurements

Upconversion nanocrystals (UCNCs) represent a unique class of materials capable of absorbing multiple near-infrared (NIR) excitation photons to generate higher-energy photons spanning the ultraviolet (UV), visible (vis), or a higher energy NIR spectral region.¹⁻⁹ These upconverted emissions are achieved through both quasi-resonant and non-resonant energy transfers involving rare-earth ion pairs doped within a crystalline matrix; multiple quanta of NIR photons of approximately 976 nm are resonantly absorbed by the Yb³⁺ ion, populating the Yb³⁺ ²F_{5/2} electronically excited state, where higher energy states of co-doped lanthanide ions in the UCNC are populated through a variety of energy transfer pathways and continued 976 nm illumination. An example of these transitions for the Yb-Er lanthanide pair is shown in **Figure 1** with a brief description. Since lanthanide series ions feature transition energies that derive from the extent of their individual *f*-block electronic occupancies, emissive bands in UCNCs can each be selectively tuned, amplified, or demodulated via dopant ion and concentration variation for optimal emissive characteristics. The resonant and non-resonant energy transfers between Yb³⁺ and the second residing lanthanide ion(s) are mediated by electron-phonon interactions within the crystalline matrix, where non-resonant energy differences are accounted for via the absorption or emission of phonons within the host crystal lattice. As such, the energy and intensity of emitted light depends

not only upon the nature and concentration of lanthanide ions, but also the composition of the host crystalline lattice, allowing for several parameters of variation for optimal emissive characteristics.

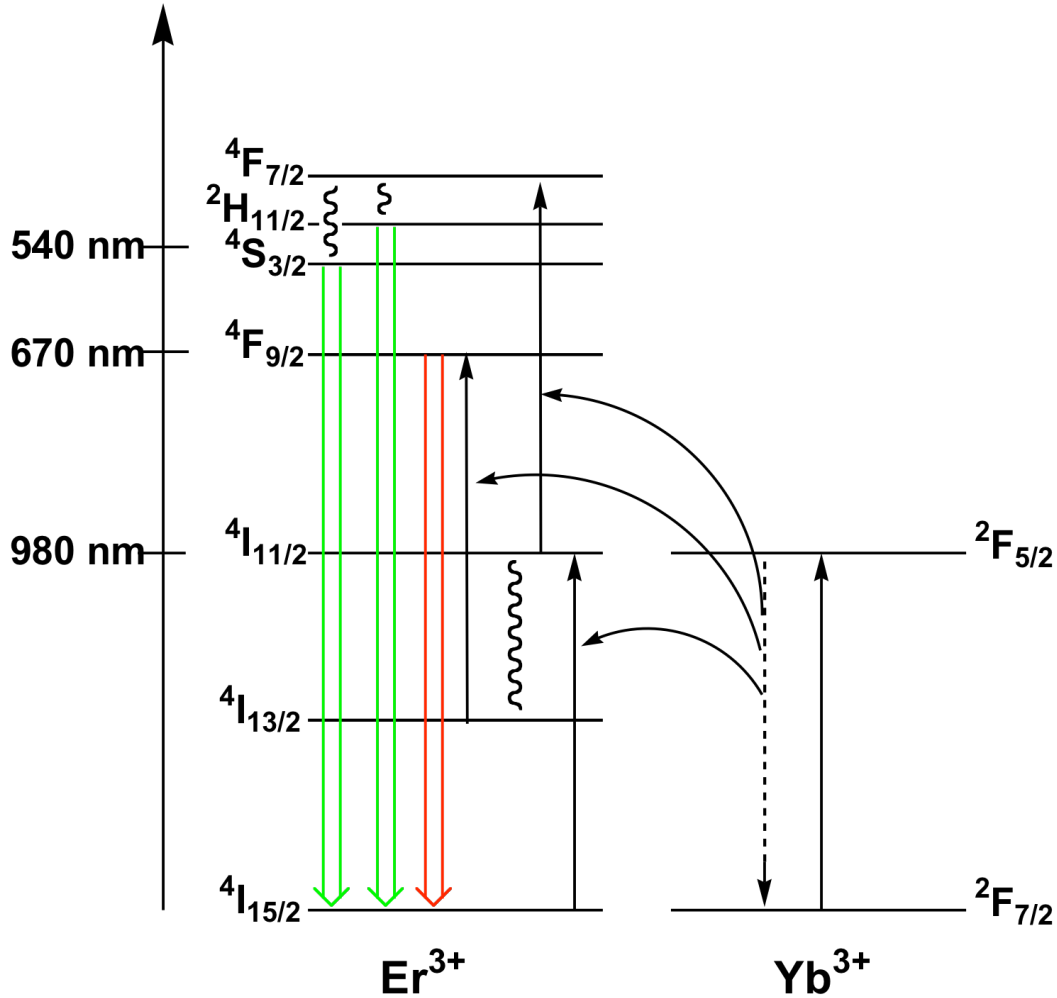


Figure 1: Notable upconversion mechanisms contributing to 540 nm centered $^2H_{11/2}/^4S_{3/2} \rightarrow ^4I_{15/2}$ and 670 nm centered $^4F_{9/2} \rightarrow ^4I_{15/2}$ radiative transitions in Er-Yb co-doped upconversion nanocrystals. 980 nm laser excitation populates the Yb^{3+} ion $^2F_{5/2}$ state, and the more weakly absorbing Er^{3+} $^4I_{11/2}$ state (solid vertical arrows); appropriately high laser fluences drive population of higher energy Er^{3+} excited states via processes that include Er^{3+} excited state absorption (ESA) (solid vertical arrows) and energy transfer upconversion (ETU) involving the electronically excited Yb^{3+} $^2F_{5/2}$ state (solid curved arrows) between energy-matched excited states of Er^{3+} and Yb^{3+} . Phonon relaxations (wavy lines) result in populations at intermediate ($^4I_{13/2}$) and emitting ($^2H_{11/2}/^4S_{3/2}$) Er^{3+} excited states. Subsequent radiative transitions within the Er^{3+} f -block states produce green [$^2H_{11/2} \rightarrow ^4I_{15/2}$; $^4S_{3/2} \rightarrow ^4I_{15/2}$; 515 – 570 nm] and red [$^4F_{9/2} \rightarrow ^4I_{15/2}$; 645 – 690 nm] emission lines.

Relatively few studies exist that have attempted to measure quantum yield values of bulk-upconversion phosphors, with only one known attempt made to quantify the absolute quantum yield of UCNCs in the solution phase.¹⁰ Furthermore, no studies performed to date have reported total radiant fluxes of such materials, even though the radiant flux is the true unit of merit when comparing materials' light-output for utility on an applications basis. Measurements of the absolute quantum yield values for bulk-phase upconverting phosphors were first performed by Auzel and Pecile, who employed an integrating sphere to compare quantum yield values of different lanthanide dopant concentrations in fluoride- and tungstate-based crystals.^{11,12} Another pioneering study by Page *et al.* examined power-dependent quantum yield values of multiple fluoride- and oxide-based bulk upconversion materials in the solid-state using a power meter and optical filters attached to an integrating sphere; these investigators, for example, reported a peak upconversion quantum yield for bulk [NaYF₄; Yb (18%), Er (2%)] at approximately 4% over a laser excitation power density range of 20 - 40 W/cm².¹³ More recently, Faulker *et al.* reported absolute quantum yield measurements of upconversion materials in the solid-state, ranging up to an approximate average of 13% quantum yield for the largest bulk samples.¹⁴ The only nanocrystalline study was performed by Boyer and van Veggel,¹⁰ who investigated the size-dependent upconversion absolute quantum yields of [NaYF₄; Yb (20%), Er (2%)] UCNCs in the solution phase, showing that the larger particles produce a higher quantum yield on a per mass basis. They showed that a 100 nm composition displayed a quantum yield of 0.30 ± 0.10 %, a 30 nm composition displayed a quantum yield of 0.10 ± 0.05 %, and a 10 nm composition displayed a quantum yield of 0.005 ± 0.005 %, all measured at 150 W/cm² when integrating the visible emission bands. However, all of these data have significant (30% - 100%) uncertainty values, most likely caused by UCNCs' poor

absorbance cross-section, making the quantum yield a difficult value to measure reliably.

1.1.2 Motivation

One of the principal applications of UCNCs is their use as luminescent imaging probes, revealing such advantages over organic-molecule and quantum dot imaging modalities as: (i) enhanced tissue penetration and minimized tissue scatter using NIR excitation relative to visible excitations, (ii) the disappearance of any biological autofluorescence by measuring the upconverted emissions, and (iii) improved stability against molecular photobleaching and blinking.^{3,15-18} Another benefit of UCNCs is the ability to functionalize their surfaces such that they afford greater than 90% cell viability at concentrations up to several hundred micrograms of UCNCs per milliliter, which has already been demonstrated with success for *in vitro* applications such as biological imaging,^{17,19-29} cellular tracking,^{16,30} and photodynamic therapy.³¹⁻³³ Even further, studies exploring the potential for *in vivo*^{16,19} and whole body^{17,20,24,25,34} UCNC-based imaging of small animals has been shown via CW excitation, giving significant biological imaging potential for this recently developed imaging modality.

While the previous examples of upconversion bulk and nanocrystal quantum yield measurements discussed above provide an approximate assessment on specific upconversion composition quantum yields under certain excitation conditions, the absence of direct radiant flux values, rigorously detailed bulk sample preparations for measurement as reference samples that can be reproduced in any laboratory, experiments that detail the excitation power dependences of the quantum yield and radiant flux for fs-pulsed and CW laser light sources, and post-synthetic characterization data, such as that provided by inductively coupled plasma atomic emission spectroscopy (ICP-AES), implores the need for innovative and thorough light-

measurement capabilities on highly characterized material compositions to better examine, design, and exploit UCNCs in applications. These facts motivated the design of a custom-engineered integrating sphere system to provide the first such study on highly characterized UCNCs that thoroughly establishes itself as the “standard of practice” for this field.

1.1.3 Summary and Goals

Chapter 2 presents the laser power-dependent total radiant flux and absolute quantum yield measurements of homogeneous, solution-phase [NaYF₄; Yb (15%), Er (2%)] upconversion nanocrystals, and further compares the quantitative total radiant flux and absolute quantum yield measurements under both 970 nm continuous-wave and 976 nm pulsed Ti-Sapphire laser excitation (140 fs pulse-width, 80 MHz). This study demonstrates that at comparable excitation densities under continuous-wave and fs-pulsed excitation from 42 - 284 W/cm², the absolute quantum yield is higher under fs-pulsed laser excitation, whereas the total radiant flux is higher under continuous-wave excitation, when spectra are integrated over the 500 - 700 nm wavelength regime. This study further establishes the radiant flux as the true unit of merit for quantifying emissive output intensity of upconverting nanocrystals for application purposes, especially given the high-uncertainty in solution phase upconversion nanocrystal quantum yield measurements due to their low absorption cross-section. Additionally, a commercially available bulk [NaYF₄; Yb (20%), Er (3%)] upconversion sample was measured in the solid-state to provide a total radiant flux and absolute quantum yield standard. The measurements were accomplished utilizing a custom-engineered, multi-detector integrating sphere measurement system that can measure spectral sample emission in Watts on a flux-calibrated (W/nm) CCD-spectrometer, enabling the direct

measurement of the total radiant flux without needing an absorbance or quantum yield value.

It is the goal of this work not just to highlight a custom engineered instrument, but to provide foundational measurements of homogeneous, solution-phase UCNCs, and to convey standard methods of practice for correct quantitative measurement and analysis of UCNC emission properties to be exploited in applications like biological imaging. The study meticulously details all sample preparations, measurement components, metrology, and compares and contrasts the different types of laser excitation. Further, it is the goal of this work to explain and establish the total radiant flux as the unit of merit when comparing different materials for light-based application utility.

1.2 Scintillating Nanocrystals and Their Integration Into Radiation Sensing Device Architectures

1.2.1 Scintillating Nanocrystals

Lanthanide-doped inorganic scintillators have long been exploited as radiation sensing materials due to their high stabilities and emission characteristics, and the fact that the emissive wavelengths of these materials are compatible with conventional photomultiplier tube detectors.³⁵⁻³⁷ However, factors such as crystal growth conditions and the need for cryogenic cooling, for example, have limited the extent to which many of these materials can be deployed. Modern photodetectors, such as those based on CCD cameras and Si-photodiodes, enable enhanced scintillation emission detection sensitivities, and open up new possibilities to exploit scintillators that are smaller, easier

to produce, and scintillate within the photodetector spectral regime that affords optimal quantum efficiency of the photovoltaic response (generally between 500-1000 nm).

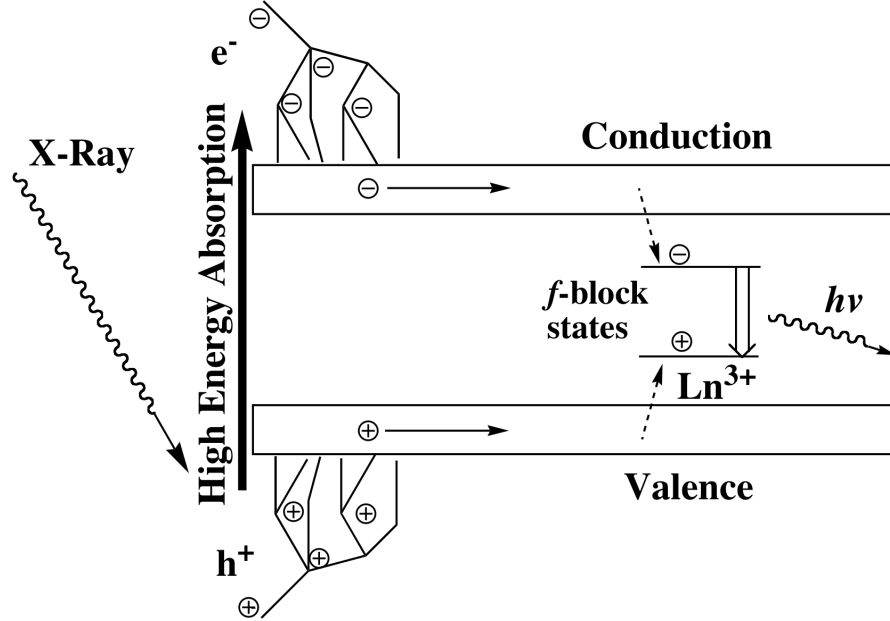


Figure 2: X-ray excited emission (scintillation) stems from initial x-ray absorption, electron-hole (e^-h^+) pair generation, subsequent valence and conduction band energy trapping and collection, and ensuing radiative emission from lanthanide f -block states lying within the valence and conduction band gap.

The basic mechanism of x-ray excited emission (scintillation) stems from initial x-ray absorption, electron-hole (e^-h^+) pair generation, subsequent valence and conduction band energy trapping and collection, and ensuing radiative emission from lanthanide f -block states lying within the valence and conduction band gap (**Figure 2**).^{35,36} Although this mechanism is well established for bulk-samples, these processes have rarely, if ever, been probed on the nanoscale; little is known, for example, regarding the x-ray absorptive cross-sections, scintillation efficiencies, energy dependence and saturation thresholds of such nanoscale materials.

Bulk-phase europium-doped yttrium oxide ($[Y_2O_3; Eu]$) is one such lanthanide-doped inorganic material that garnered acclaim for its use as the red-phosphor in early

cathode ray televisions³⁸ and as the scintillator material in a wide variety of x-ray computed tomography (CT) detectors by GE-Healthcare:³⁹ both of these applications exploit the material's peak emissions near 600 nm, radiation and environmental stability, and room-temperature usability. The ability to further synthesize $[\text{Y}_2\text{O}_3; \text{Eu}]$ constructs on the nanoscale has afforded new applications of its utility in white light emitting diodes⁴⁰ and *in vitro* imaging.⁴¹ However, despite the fact that GE has used this material in thousands of X-Ray CT instruments, and despite the fact that the per-mass scintillation yield of $[\text{Y}_2\text{O}_3; \text{Eu}]$ nanocrystals was shown to exceed that of their bulk counterparts under electron-beam excitation,⁴² nanoscale $[\text{Y}_2\text{O}_3; \text{Eu}]$ x-ray scintillation properties have yet to be fully interrogated and explored. While scintillating nanomaterials have been delineated and demonstrate considerable potential,⁴³⁻⁴⁷ relatively little work has capitalized upon such materials in device architectures pertinent to applications in radiation sensing and detection.

1.2.2 Medical Dosimetry

Accurate, cost effective, and real-time *in vivo* patient dosimetry during radiation therapy (RT), diagnostic, and interventional x-ray procedures provides an invaluable tool for monitoring organ doses, assessing patient safety, and improving clinical outcomes. Ideal clinical dosimeters should have the following properties by providing: (i) simplicity in operation, (ii) cost-effectiveness, (iii) real-time reading, (iv) negligible performance degradation in a normal hospital environment, and (v) minimum radiation damages during its lifetime. In addition, the detector may add additional values by providing: (i) negligible image artifacts, (ii) small size point dosimetry, and (iii) easy integration in clinical environments.

Current commercial detectors can provide several of the attributes listed above, but all fall short on at least one if not more of the aforementioned desired detector

specifications. MOSFETs are relatively small and durable dosimeters that provide an easy way to measure point doses near real-time.⁴⁸ However, there are several factors that would limit their use for *in vivo* therapy and diagnostic applications. One foremost limitation of MOSFETs is their finite lifetime of use due to radiation damage; MOSFETs record dose on a radiation-to-charge generated (mV) scale, with a total lifetime of about 16,000-20,000 mV (16-20 Gray; Gy, absorbed radiation by tissue (J/kg)).⁴⁹ Radiation aging of MOSFET detectors has been reported previously and the re-calibration of the detectors has been suggested for both diagnostic and therapy MOSFETs.^{50,51} In addition, MOSFETs have angular response dependencies due to the geometry of the sensitive detector area,⁵² which limits their use for rotational radiation fields such as axial and helical scans in CT. Another imperfection of MOSFETs is that they are *integrating detectors*, where subtracting the final voltage from the initial voltage reading of each individual experiment is used to determine the absorbed dose. Thus, MOSFETs cannot obtain dose-rate responses in *real-time*, nor can they measure dose fluctuations in real-time during the experiment integration, an attribute highly desired for pin-point *in vivo* dosimetry and radiation surveillance applications. Finally, MOSFETs and the required signal wires are not radio-opaque; they are comprised of high Z materials of metal-oxide sensors and copper wires, and thus they can obstruct underlying structures on radiographic images,⁵³ or scatter radiation from arriving to its target point.

Thermo-luminescent dosimeters (TLDs) have seen widespread use for dosimetry due to their accuracy and ease of re-use, but are often not chosen as the primary method of measurement due to several drawbacks. The first drawback is that TLDs require a time consuming annealing process prior to exposure (for a TLD-100, annealing takes at least 3 hours), and like MOSFETs, they are an integrating detector, not allowing for real-time dose rates. Another consequence of this integration happens during transportation

and storage, as TLDs must be shielded from UV and visible light to minimize false readings.⁵⁴ The recommended stabilization time of 24 hours post-irradiation prior to reading further limits their usefulness as a fast read-out detector, particularly considering the additional instrumentation needed to quantify the dose.⁵⁵ This point furthers the consideration of using TLD dosimetry versus other methods, as it can be very expensive and time consuming, especially when one considers the cost of the TLD reader, nitrogen gas system, TLD annealing equipment, and manpower. Lastly, TLDs are delicate and require careful handling with vacuum tweezers since dust, dirt, and scratches can introduce errors in the measured dose values.

The ion-chamber (IC) dosimeter performs near real-time and integrated dose measurements, can detect a broad spectrum of incident x-ray and gamma-ray energies, and offers superior durability, making it the gold-standard for dosimetry. Unfortunately, it is not feasible to use an IC for many of the *in vivo* applications in the clinic, nor for organ dose measurements in the phantom due to the relatively large size of ICs being a centimeter or greater in diameter.

Fiber-optic based radiation detectors have been of recent interest, with several design and fabrication routes to achieve ultra-small size, radiation and handling durability, as well as sensitivity. The most common of these is made by attaching a plastic scintillator at the end of an optical fiber,⁵⁶⁻⁵⁸ or by encasing a plastic scintillator with a non-scintillating cladding at the end of an optical fiber, some of which are commercialized by companies like Saint-Gobain (Paris, France) and Kuraray (Tokyo, Japan). A very detailed literature example with comparative results highlights how plastic fiber length, fiber diameter, and fiber scintillator type perform, with results showing that the plastic scintillator with a non-scintillating cladding produces more light than simply attaching a plastic scintillator at the end of the tip, both using a PMT

for the photodetector.⁵⁶ By using the latter plastic scintillator at the end of an optical fiber with a electron multiplying charge coupled device (EMCCD) camera, the same authors were able to accurately demonstrate dose measurements in an anthropomorphic prostate phantom in real-time,⁵⁷ which provides foundational capabilities for ultra-small radiation detectors. However, the use of EMCCD cameras in the field is impractical, due to their high cost, high noise with high gain acquisition, and additional size, power and mounting requirements, to name a few.

1.2.3 Motivation

The lack of foundational energy and flux dependent x-ray excited scintillation measurements on nanoscale scintillators that display advantageous physical and light-based properties, such as environmental and radiation stability, ease of synthesis, and emission wavelengths matching optimal Si-photodetector sensitivities, inspires such studies that take advantage these materials' properties for next-generation devices that are small, accurate, and less expensive than current dosimetry technologies. Further, despite the widespread clinical use of radiation-based methods for diagnosis and therapy, none of the aforementioned dosimeters (MOSFETs, TLDs, ICs) provide convenient, inexpensive, *real-time* devices capable of measuring or confirming the radiation dose delivered *in/ex vivo*. In order to ensure the safety of the patient, provide proper treatment to areas of malignancy in radiation therapy, and study radio-biological effects, it is essential to establish a more systematic description of the radiation dose delivered to and in tissue by developing novel device architectures.

1.2.4 Summary and Goals

Chapter 4 presents the development and characterization of Eu- and Li-doped yttrium oxide nanocrystals [$Y_{2-x}O_3$; Eu_x, Li_y], in which Eu and Li dopant ion concentrations were systematically varied in order to define the most emissive

compositions under specific x-ray excitation conditions. These optimized $[Y_{2-x}O_3; Eu_x, Li_y]$ compositions displayed scintillation responses that: (i) correlate linearly with incident radiation exposure at x-ray energies spanning from 40 - 220 kVp, and (ii) manifest no evidence of scintillation intensity saturation at the highest evaluated radiation exposures [up to 4 Roentgen per second]. For the most emissive nanoscale scintillator composition, $[Y_{1.9}O_3; Eu_{0.1}, Li_{0.16}]$, excitation energies of 40, 120, and 220 kVp were chosen to probe the dependence of the integrated emission intensity upon x-ray exposure-rate in energy regimes where either the photoelectric or the Compton effect governs the scintillation mechanism: these experiments demonstrate for nanoscale $[Y_{2-x}O_3; Eu_x]$, that for comparable radiation exposures, when scintillation is governed by the photoelectric effect (120 kVp excitation), greater integrated emission intensities are recorded relative to excitation energies where the Compton effect regulates scintillation (220 kVp excitation).

Nanoscale $[Y_{1.9}O_3; Eu_{0.1}, Li_{0.16}]$ (70 ± 20 nm) was further exploited as a detector material in a prototype fiber-optic radiation sensor. The scintillation intensity from the $[Y_{1.9}O_3; Eu_{0.1}, Li_{0.16}]$ -modified, 400 micron-sized optical fiber tip, recorded using a CCD-photodetector and integrated over the 605 - 617 nm wavelength domain, was correlated with radiation exposure using a Precision XRAD 225Cx small-animal image guided radiation therapy (IGRT) system. For both 80 and 225 kVp energies, this nearly radiotransparent device recorded scintillation intensities that tracked linearly with total radiation exposure, highlighting its capability to provide alternately accurate dosimetry measurements for both diagnostic imaging (80 kVp) and radiation therapy treatment (225 kVp).

Chapter 5 further explores the device development of Chapter 4 by utilizing a small, USB-powered Si-photodiode to record the scintillation of the nanoscale $[Y_{1.9}O_3;$

Eu_{0.1}, Li_{0.16}] fiber-optic sensor, which was able to record accurate dosimetry data in and on tissue phantoms under clinical x-ray CT energy and flux settings in strong accord to the gold-standard IC dosimeter. Chapter 5 proves that this nano-scintillator device is capable of producing enough light such that basic light-detection architecture afforded by Si-photodiodes can be readily utilized to provide a device capable of real-time, accurate dosimetry, with dimensions appropriate for *in vivo* use.

It is the goal of this work to systematically optimize nanoscale scintillators to be the most emissive through compositional variation, as well as study their scintillation properties as a function of x-ray energy and flux. Further, this work shows their direct utility in a device-based application that provides unique abilities to record radiation dosimetry with near pin-point accuracy in *real-time*. This research project has provided several opportunities for collaborative research across Radiology, Radiation Oncology, Medical Physics, and Physics departments at Duke University and University of North Carolina at Chapel Hill, with many ongoing experiments to test the device in a variety of radiation fields relevant to medical, nuclear, and outer-space settings and applications.

1.3. Additional Chapters

Chapter 3 presents an upconverting nanomaterial composition, [Y₂O₃; Yb (2%), Er (1%)], that converts both X-ray and high-fluence NIR irradiation to visible light. This composition is compared to a higher Yb³⁺ doped composition, [Y₂O₃; Yb (10%), Er (1%)], that displays diminished visible X-ray scintillation, but shows enhanced red wavelength centered upconversion emission. These nanocrystals were characterized by TEM, X-ray diffraction, power-dependent upconversion luminescence, and X-ray scintillation spectroscopy. It is further demonstrated that lithium ion doping of the [Y₂O₃; Yb (2%), Er (1%)] nanoscale composition leads to enhanced X-ray and NIR excited emission intensities through the production of nanoparticles that feature slightly enhanced sizes

and increased crystallinity. Given the aforementioned advantages utilizing upconversion nanocrystals as luminescent imaging probes (Section 1.1.2), functionalized rare-earth doped nanomaterials that display x-ray excited luminescence and upconversion luminescence should impact next-generation multi-modal imaging methods that combine information gleaned from long-wavelength upconversion optical imaging and high-resolution x-ray luminescence computed tomography.

Appendix A presents fluorescence analysis on the solvation environment of re-suspended poly[1,5-bis(3-propoxysulfonic acid sodium salt)-2,6-naphthylene]ethynylene (PNES) wrapped single-walled carbon nanotubes (SWNTs), and Raman spectroscopy of directly suspended PNES-SWNTs in multiple solvents, that was in part, used in a collaborative publication.⁵⁹ Two-dimensional excitation-emission maps were collected on PNES-SWNT samples that had been originally made in D₂O, dried, and re-suspended in D₂O, as well as in MeOH and DMSO via a phase transfer catalyst to understand the stability of the PNES-SWNT supramolecular compositions in comparison with the samples directly made in those solvents.⁵⁹ The excitation-emission results of directly suspended and re-suspended PNES-SWNTs were in qualitative accord with each other, showing that the solvent's polarity, as well as the solvent's electrophilicity, play important roles on the emission efficiencies of individualized SWNTs. Raman spectroscopic interrogation of the radial breathing modes of directly solvent-suspended PNES-SWNTs showed that there were no changes upon PNES wrapping versus SDS surfactant dispersion in D₂O, and that there were no further changes in the peak positions due to solvent. This Raman spectroscopic data confirms the previous AFM and TEM structural characterizations that the PNES-SWNT supramolecular structure remains constant in different solvent environments, and further does not affect the inherent vibrational structure of SWNTs.

Appendix B presents the absolute quantum yield determination of free base tetraphenylporphyrin (H₂TPP) in benzene under multiple excitation wavelengths using a commercially available integrating sphere system. The results show that the quantum yield values previously measured via the relative method overestimated the quantum yield values for H₂TPP by a factor of 1.6, with the absolute method determining the quantum yield to be 7.0% in aerated benzene at all excitation wavelengths from 405 - 588 nm and 8.7% in de-aerated benzene under 546 nm excitation, establishing H₂TPP as a broad band excitable quantum yield standard. Additionally, solutions of fluorescein, ruthenium tris(2,2'-bipyridyl)ruthenium(II) (Ru(bipy)₃²⁺), and rhodamine 101 were measured to verify that the methods used to measure H₂TPP produce consistent quantum yield results with recent absolute determinations from literature.^{60,61}

2. Power-Dependent Total Radiant Flux and Absolute Quantum Yield Measurements of Solution-Phase [NaYF₄; Yb, Er] Upconversion Nanocrystals Under Continuous and Femtosecond-Pulsed Laser Excitation

Elucidating structure-function relationships relevant to the photophysics of nanomaterials that upconvert high-power, near-infrared excitation to shorter wavelength NIR, visible, and UV emission requires extensive compositional characterization and rigorously measured light-based properties. Presented herein is the laser power-dependent total radiant flux and absolute quantum yield measurements of homogeneous, solution-phase [NaYF₄; Yb (15%), Er (2%)] upconversion nanocrystals, and further compares the quantitative total radiant flux and absolute quantum yield measurements under both 970 nm continuous-wave and 976 nm pulsed Ti-Sapphire laser excitation (140 fs pulse-width, 80 MHz). This study demonstrates that at comparable excitation densities under continuous-wave and fs-pulsed excitation from 42 - 284 W/cm², the absolute quantum yield is higher under fs-pulsed laser excitation, whereas the total radiant flux is higher under continuous-wave excitation, when spectra are integrated over the 500 - 700 nm wavelength regime. This study further establishes the radiant flux as the true unit of merit for quantifying emissive output intensity of upconverting nanocrystals for application purposes, especially given the high-uncertainty in solution phase upconversion nanocrystal quantum yield measurements due to their low absorption cross-section. Additionally, a commercially available bulk [NaYF₄; Yb (20%), Er (3%)] upconversion sample was measured in the solid-state to provide a total radiant flux and absolute quantum yield standard. The measurements were accomplished utilizing a custom-engineered, multi-detector integrating sphere

measurement system that can measure spectral sample emission in Watts on a flux-calibrated (W/nm) CCD-spectrometer, enabling the direct measurement of the total radiant flux without needing an absorbance or quantum yield value.

2.1 Introduction

Upconversion nanocrystals (UCNCs) represent a unique class of materials capable of absorbing multiple near-infrared (NIR) excitation photons to generate higher-energy photons spanning the UV, visible and higher-energy NIR. The upconverted emissions are achieved via multi-photon absorptions, which undergo subsequent quasi- and non-resonant energy transfers between long-lived excited states in rare-earth ions doped within a crystalline matrix,¹⁻⁹ and as such, the specific UCNC composition defines the energy and intensity of emitted light.

One of UCNCs' noteworthy uses is as luminescent imaging probes, providing several distinct advantages over typical organic and inorganic molecules, fluorescent proteins, and quantum dots excited by visible wavelengths: (i) the NIR excitation has enhanced tissue penetration and tissue scatter is minimized relative to visible excitations, (ii) the disappearance of any biological auto-fluorescence by measuring the upconverted emissions, and (iii) improved stability against molecular photobleaching and blinking.^{3,15-18} Another advantage is the ability to functionalize UCNC surfaces that afford greater than 90% cell viability at concentrations up to several hundred micrograms of UCNCs per milliliter, and has been demonstrated for *in vitro* applications such as biological imaging,^{17,19-29} cellular tracking,^{16,30} and photodynamic therapy³¹⁻³³ using CW excitation. However, very few examples have tried UCNC imaging utilizing fs-pulsed lasers,^{18,62} even as fs-pulsed lasers have shown remarkable imaging resolution and penetration depths when employed for organic-fluorophore-based two-photon imaging.^{63,64} One potential issue with *in-vitro* UCNC imaging is that fast scan speeds

result in blurred images due to the long lifetime emissions of UCNCs, but it was well demonstrated that using a confocal pinhole greatly reduced the out-of-focus upconversion imaging signals seen in either CW or fs-pulsed excitation,¹⁸ allowing the resolution to mirror that of their organic counterparts. Even further, studies exploring the potential for *in vivo*^{16,19} and whole body^{17,20,24,25,34} UCNC imaging of small animals has been shown via CW excitation, giving significant biological-use potential for this recently developed imaging modality. While the benefits noted above underscore the importance of upconversion nanocrystals for ultra-sensitive diagnosis and imaging applications, the development of next-generation UCNCs will require modulation of nanocrystal composition, size, and crystal phase, the nature and density of surface ligand substitution, and the type of excitation source and power-density able to be achieved: evaluation of structure-function relationships under different laser excitation conditions that inform critical design criteria beseech the need for rigorous, quantitative, and accurate photophysical characterization methods for these materials.

The most significant metric for quantifying a material's ability for applications when trying to generate the most luminescence possible is the radiant flux, defined as the amount of energy emitted per unit time per unit volume for a given stimulus. For laser-excited luminescence, the total radiant flux is a measure of the amount of incident laser excitation energy converted into luminescence energy for a specific sample preparation, and is a function of the incident laser power, material absorption, volume of material excited, and material quantum yield, with the quantum yield defined as the amount of light emitted versus the light absorbed. Although it is important to design and develop materials with exceptional quantum yields, it is the radiant flux comparison between materials and excitation conditions that will ultimately define the most emissive combination; for instance, even if a material has an exceptionally high quantum

yield, it may have a very low absorptive cross-section, thus generating significantly less light (total radiant flux) than a material with the same quantum yield and a higher absorptive cross-section. However, for UCNC development and optimization, quantum yield values shouldn't be ignored, as they can be used to gain insights into compositional and excitation characteristics that give more efficient light conversion, and subsequently more radiant flux, towards achieving next-generation UCNCs with augmented luminescence intensity.

Measurements of the absolute quantum yield values for bulk-phase upconverting phosphors were first performed by Auzel and Pecile, who employed an integrating sphere to compare quantum yield values of different lanthanide dopant concentrations in fluoride- and tungstate-based crystals.^{11,12} Another pioneering study by Page *et al.* examined power-dependent quantum yield values of multiple fluoride- and oxide-based bulk upconversion materials in the solid-state using a power meter and optical filters attached to an integrating sphere; these investigators, for example, reported a peak upconversion quantum yield for bulk [NaYF₄; Yb (18%), Er (2%)] at approximately 4% over a laser excitation power density range of 20 - 40 W / cm².¹³ More recently, Faulker *et al.* reported absolute quantum yield measurements of upconversion materials in the solid-state, ranging up to an approximate average of 13% quantum yield for the largest bulk samples.¹⁴ While these previous studies report quantum yield measurements for bulk upconverting materials, few attempts have been made to quantify the absolute quantum yield of UCNCs in the solution phase;¹⁰ furthermore, no studies performed to date have reported total radiant fluxes of such materials. Boyer and van Veggel investigated the size-dependent upconversion absolute quantum yields of [NaYF₄; Yb (20%), Er (2%)] upconversion nanocrystals in solution, with significant (30% - 100%) uncertainty values, showing that the larger particles produce a higher quantum

yield on a per mass basis, with a 100 nm composition displaying a quantum yield of $0.30 \pm 0.10 \%$, a 30 nm composition displaying a quantum yield of $0.10 \pm 0.05 \%$ at 150 W/cm^2 , and a 10 nm composition displaying a quantum yield of $0.005 \pm 0.005 \%$, at 150 W/cm^2 when integrating the visible emission bands.¹⁰ For comparison purposes, Boyer and van Veggel also synthesized and measured a bulk $[\text{NaYF}_4; \text{Yb} (20\%), \text{Er} (2\%)]$ material at $3.0 \pm 0.3\%$ quantum yield under 20 W/cm^2 excitation, which was similar to Page *et al.*'s 4% quantum yield measurement at this power density.¹³ While these examples of previous upconversion bulk and nanocrystal quantum yield measurements provide an approximate assessment on specific upconversion composition quantum yields under certain excitation conditions, the absence of direct radiant flux values, rigorously detailed bulk sample preparations for measurement as reference samples that can be reproduced in any laboratory, experiments that detail the excitation power dependences of the quantum yield and radiant flux for fs-pulsed and CW laser light sources, and post-synthetic characterization data, such as that provided by inductively coupled plasma atomic emission spectroscopy (ICP-AES), implores the need for innovative and thorough light-measurement capabilities on highly characterized material compositions to better examine, design, and exploit UCNCs for ultra-sensitive biological imaging, diagnosis, and treatment.

Presented herein is the power-dependent total radiant flux and absolute quantum yield measurements of a homogeneous, solution-phase upconversion nanocrystal composition, and directly compares these metrics under 970 nm CW and 976 nm fs-pulsed Ti-Sapphire laser excitation (140 fs pulse-width, 80 MHz). This study illustrates that at comparable excitation densities under continuous-wave and fs-pulsed excitation from $42 - 284 \text{ W/cm}^2$, the absolute quantum yield is higher under fs-pulsed laser excitation, whereas the total radiant flux is higher under continuous-wave

excitation, when spectra are integrated over the 500 - 700 nm wavelength regime. This study further establishes the radiant flux as the true unit of merit for quantifying emissive output intensity of upconverting nanocrystals for application purposes, especially given the high-uncertainty in solution phase upconversion nanocrystal quantum yield measurements due to their low absorption cross-section. These measurements were accomplished using a custom-engineered, multi-detector integrating sphere measurement system utilizing a three-position sample-measurement methodology described by de Mello, Whitmann, and Friend⁶⁵ to accurately account for direct and indirect absorption and emission within the sphere. Hexagonal-phase [NaYF₄; Yb (15%), Er (2%)] nanocrystals (diameter = 28 nm) dispersed in toluene at 1 mg/mL were utilized to make these foundational measurements, which were characterized by transmission electron microscopy (TEM), x-ray diffraction (XRD), and inductively coupled plasma atomic emission spectroscopy (ICP-AES). The Yb-Er ion pair provides two distinct emission bands centered at 540 and 660 nm, that respectively arise from the Er³⁺-based $^2H_{11/2}/^4S_{3/2} \rightarrow ^4I_{15/2}$ and $^4F_{9/2} \rightarrow ^4I_{15/2}$ transitions. Solid-state emission lifetime measurements conclusively showed that the $^2H_{11/2}$ (525 nm) and $^4S_{3/2}$ (545 nm) states display matching $62 \pm 2 \mu s$ rise and $302 \pm 3 \mu s$ decay single-exponential time constants, respectively, prompting their combination in the quantum yield and radiant flux calculations. The material synthesis, absolute measurements, complete description of the measurement methods and metrology is thoroughly established. Additionally, a commercially available upconversion material, [NaYF₄; Yb (20%), Er (3%)] was acquired and measured in the solid-state at 25 W/cm² to provide a quantitative standard for radiant flux and absolute quantum yield research in this field.

2.2 Experimental

Materials:

Synthesis of [NaYF₄; Yb (15%), Er (2%)] nanocrystals. The following method was adapted from a synthesis of hexagonal-phase (beta) NaYF₄: Yb, Er nanocrystals reported by Qian *et al.*² Salts (99.99%) were obtained from Sigma-Aldrich and liquids were obtained from Fisher Scientific; all were used without further purification. YCl₃ (0.78 mmol), YbCl₃ (0.20 mmol) and ErCl₃ (0.02 mmol) were dissolved in 2 mL water (HPLC grade) in a 100 mL round-bottomed flask. 6 mL oleic acid (NF/FCC) and 15 mL 1-octadecene (technical grade) were then added, and the solution was heated to 100 °C under vacuum for 10 min using a heating mantle connected to a digital temperature controller. The solution was then heated to 156 °C for 30 min to ensure removal of all water and solvation of the rare-earth salts as indicated by the yellow color of the resulting solution. After the solution was cooled to room temperature, NH₄F (4.0 mmol) and NaOH (2.5 mmol) were added in a methanol solution (10 mL). The solution was then heated to 80 °C for 30 min under positive argon flow and then switched to vacuum to ensure removal of all methanol. After returning the flask to positive argon flow, the solution was heated to 310 °C at a rate of 20 °C/min and held for 150 min before being cooled to room temperature. Particles were isolated via centrifugation and washed twice in 50:50 hexanes/ethanol before being dried by rotary evaporation. Particles were re-suspended in toluene (spectroscopic grade) using sonication at 1 mg/mL for all measurements.

Bulk [NaYF₄; Yb (20%), Er (3%)]. The bulk upconverting sample was purchased from Sigma-Aldrich and used as is (Batch number: MKBK3038). A certificate of analysis showed that inductively coupled plasma optical emission spectroscopy confirmed Na, F, F, Yb, and Er components, and further provided a trace metals analysis. The average size

(d50) was reported to be 1 micron. For sample measurement solid powder was placed between two pieces of glossy weigh-paper at a density of approximately 1 mg/mm, which was placed on a machine press (**Figure 3A**). The sample was then pressed at 1000 psi, and maintained at this pressure for 10 sec. The compressed solid-state piece was then cut into a 8 x 8 mm square wafer as best as possible without fracturing using a razor blade, and mounted vertically in a 1 cm cuvette using a 1 x 1 mm piece of double sided tape. The wafer was mounted at the center-point of where the laser beam passes through the cuvette (**Figure 3B**).

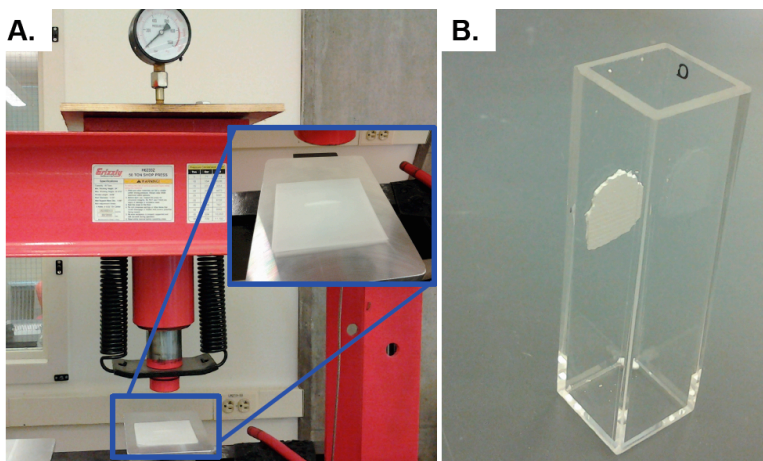


Figure 3: (A) A machine press with the [NaYF₄; Yb (20%), Er (3%)] bulk powder sample placed in-between two pieces of weigh-paper (inset), and (B) an approximate 8 x 8 mm wafer cut and mounted in a 1 cm cuvette for absolute quantum yield and radiant flux measurements of the pressed [NaYF₄; Yb (20%), Er (3%)] bulk sample.

Instrumentation:

X-ray Diffraction (XRD) and Transmission Electron Microscopy (TEM) were performed at the *Shared Materials Instrumentation Facility (SMiF)* at Duke University.

Transmission Electron Microscopy (TEM). TEM was performed using an FEI Tecnai G² Twin microscope operated at an accelerating voltage of 200kV and equipped with a TIA digital camera.

X-ray Diffraction (XRD). The as synthesized crystal structure was verified using a Panalytical X'Pert PRO MRD HR X-ray Diffraction System with a Cu Ka (1.5405 \AA) x-ray source.

Inductively Coupled Plasma Atomic Emission Spectroscopy (ICP-AES).

[NaYF₄: Yb (15%), Er (2%)] nanocrystals were digested in aqua-regia in the presence of boric acid and submitted to the Environmental and Agricultural Testing Service at North Carolina State University.

Upconversion Luminescence Lifetime Measurement System. The luminescence lifetime spectra were acquired utilizing an Edinburgh Instruments LP920 Laser Flash Photolysis Spectrometer and Edinburgh L900 Software. Excitation pulses were generated from a Q-switched Nd:YAG laser (Quantel, Brilliant) and a dual-crystal OPO (OPOTEK, Vibrant LDII) tuned to 976 nm operating at 1 Hz, a temporal pulse-width of 5 ns, and a pulse energy of 0.3 mJ, which was focused on a 5 mg pellet of [NaYF₄: Yb (15%), Er(2%)] nanocrystals using a 25 mm focal length convex lens. An Andor iStar ICCD recorded time-gated emission spectra from 250 - 800 nm over a time range from 1 - 2000 μs at 20 μs intervals, with a gate integration time of 5 μs and an ICCD camera gain setting of 150. Lifetimes were fitted using the Edinburgh L900 exponential tail-fitting package, with rise and decay times denoted by negative or positive coefficients, respectively.

Absolute Quantum Yield and Radiant Flux Measurement System.

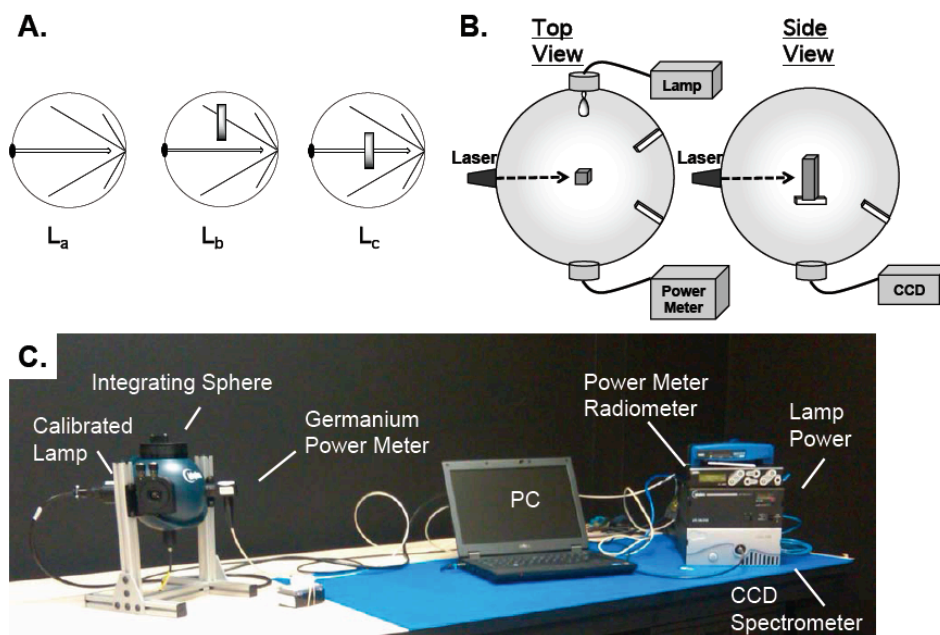


Figure 4: (A) Schematic representation of the three measurement methodology where purely the excitation laser (L_a), and the indirect (L_b) and direct (L_c) sample absorption and emission are measured, and (B) the sphere design viewing down from the top and to the side showing placement of the intensity calibrated lamp, power meter, CCD-spectrometer detector, and baffles to ensure photons bounce twice before being detected. (C) The absolute quantum yield and total radiant flux measurement system featuring an integrating sphere with a calibrated spectral flux lamp and a Germanium power meter, a fiber-coupled CCD spectrometer, and electronics necessary for the measurements (no lasers shown).

The custom engineered system shown in **Figure 4** was co-designed and engineered by Labsphere, Inc., for the solution phase 28 nm [NaYF₄: Yb (15%), Er (2%)] upconversion nanocrystal measurements, a 50 W Dilas 970 nm continuous-wave laser was injected into the sphere through an optical-fiber coupled to a fiber-collimator lens, producing a collimated 0.043 cm² beam inside the sphere for sample excitation, while a Coherent Chameleon pulsed-oscillator (80 MHz pulse-repetition, approximately 100 fs-pulse width), was tuned to 976 nm and directly injected the sphere with a 0.0018 cm² beam at the center of the cuvette. For the solid-state bulk sample measurements, the Dilas 970 nm continuous-wave laser used a collimated beam size of 0.036 cm² via an

optical-fiber coupler. All beam areas were measured by the razor-edge method at the 90/10 power diameter in 50 micron steps. The continuous-wave laser power was modulated by controlling the voltage over the diode, while a continuous OD filter wheel was used to control power from the femto-second pulsed laser before entering the sphere. A NIST-traceable, 50 lumen Labsphere SCL-050 standard lamp was mounted internally for spectral flux calibration of the CCD-spectrometer in Watts before the measurement of the sample was made. For the wavelength intensity response calibration, a 1 cm cuvette filled with non-lanthanide doped, 28 nm NaYF₄ nanocrystals suspended in toluene (1 mg/mL) was placed in the sphere to calibrate the spectral intensity response of the system; this is to account for any spectral and intensity throughput variations in the sphere caused by having a sample present. For organic molecules in solution, this step is usually just the solvent in a cuvette, as organics are typically measured at a very low OD to minimize any inner-sample concentration quenching of emission. An empty 1 cm cuvette in the sphere was used as the wavelength intensity response calibration for the solid-state sample. A significant change to the de Mello, Whitmann, and Friend method is to incorporate a laser power meter on the sphere to measure the integrated laser power fluencies and for the absorption value calculation. Since the absorption value is a unitless ratio of the excitation power in different sampling geometries, the power meter effectively measures the integrated difference of the excitation profile, in the same manner as de Mello, Whitmann, and Friend used for integrated spectral differences in the wavelength regime of the lamp excitation peak (L_x using their notation). From this, the absorption value, A , is calculated by subtracting the difference of the direct laser power (L_c) by the indirect laser power (L_b) from one (Eq. 1.);

$$A = 1 - (L_c / L_b) \quad \text{Eq. 1.}$$

However, since the upconversion nanocrystals have such a poor absorption cross-section, the measurement of the A-value is the biggest cause for error in the quantum yield measurements, as the values are so small that minor fluctuations induce significant changes to the quantum yield number. Accordingly, this fact gives the need for being able to accurately measure the total radiant flux via flux-corrected spectral measurements, where no absorption value is needed.

The final component to this system is a TE-cooled, back-thinned Labsphere CDS2100 CCD-array spectrometer running Labsphere LightMtrX software, with a usable wavelength range of 350 - 1100 nm. The integrated light in the sphere was collected on a cosine-corrected diffuser above an optical fiber to eliminate angle of incidence effects present with bare-fibers, which then transports the sampled light to the CCD-spectrometer. An 842 nm BrightLine short-pass filter (Semrock) was placed between the cosine-corrected surface and the fiber was to filter excitation laser light from entering the fiber. Since the CCD-spectrometer was wavelength corrected from the manufacturer, and was spectrally corrected for optical power (flux) using the NIST-traceable standard lamp directly mounted in the sphere as noted above, the spectral x-axis and y-axis have units of wavelength (nm) and flux (Watts per wavelength, W/nm), respectively. Because the spectrometer integration time required for spectral flux calibrations can differ from the integration time required for measurements, the spectral calibration scan is normalized by the integration time. When a measurement or calibration file was recorded in the sphere, the detector counts were divided by the integration time and then compared to the W/nm values from the standard lamp file to correct for different exposure times. This allows CCD integration times to be varied to achieve ideal pixel intensity for highest sensitivity while maintaining a linear light detection response, which was kept near 70% saturation. For example, under

continuous-wave excitation, a 10 sec integration time was used to record the lowest intensity emissions, which was shortened to 1 sec for the highest emission intensities. Complete, three-position measurements were collected three times each at all continuous-wave and pulsed laser densities over a wavelength range of 400 - 800 nm.

2.3 Results and Discussion

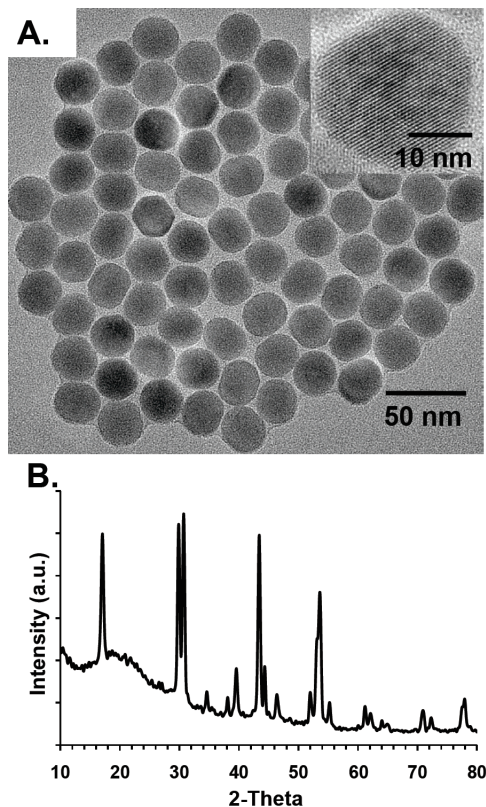


Figure 5: (A) TEM image of the [NaYF₄: Yb (15%), Er(2%)] nanocrystals, and the corresponding XRD trace confirming formation of the hexagonal phase.

Hexagonal-phase (*beta*) [NaYF₄: Yb (15%), Er (2%)] upconversion nanocrystals were synthesized using a method similar to that reported by Qian *et al.*² TEM imaging indicated that the nanocrystals were single crystals with a diameter of 28 ± 2 nm (**Figure 5A**), and XRD analysis confirmed the particles were synthesized in the hexagonal phase (**Figure 5B**). ICP-AES was used to provide as-synthesized compositional analysis showing a final composition of [NaYF₄: Yb (15%), Er (2%)] from pre-reaction

stoichiometry set to produce [NaYF₄; Yb (20%), Er (2%)], thus illustrating ICP-AES analysis is necessitated to accurately compare as-synthesized lanthanide dopant concentration-dependent photophysics in UCNCs.

A quantum yield and radiant flux measurement system, co-designed with Labsphere, Inc., was engineered to uphold the three-position quantum yield methodology developed by de Mello, Whitmann, and Friend to accurately account for direct absorption and emission and indirect re-absorption and re-emission within the sphere.⁶⁵ In brief, their absolute determination method makes use of three separate measurement positions in an integrating sphere, with the excitation and the emissive spectral response concurrently measured in the following order: (a) spectra with just the excitation source and no sample present, (b) spectra with the excitation source and sample present but not under direct excitation, and (c) spectra with the excitation source and sample present under direct excitation (**Figure 4**). The measurement of these quantities relied on integrating the excitation (absorption) and sample emission counts from a CCD-based spectrometer, where quantum yield values were produced by comparing the integrated emission to the integrated absorption from detector counts without the need to quantify photon input (excitation) or output (emission) flux in Watts. Given that they were measuring organic molecule quantum yields under Xenon lamp-based excitation, the CCD-based spectrometer was able to measure both the lamp excitation and emission spectral profiles over identical wavelength regions and under conditions whereby the excitation source did not saturate the CCD-detector prior to reliable quantification of the sample's emission. However, for the study presented herein, the high-fluence NIR excitation intensity needed to generate measureable upconversion emissions in UCNCs saturates a CCD-detector before any upconverted emission intensity can be detected, underscoring the need for a multi-detector based

absolute measurement system that can simultaneously measure sample emission and high-fluence excitation.

For the reason that the input laser power is significantly greater than the UCNC light output, the integrating sphere used herein incorporates a Germanium power meter to measure the incident excitation flux in Watts instead of integrating the excitation spectrally on the CCD-spectrometer. The incident excitation flux measured in the different sampling positions defines the corrected absorption value, A , a unitless value that compensates for directly excited absorption and indirectly excited absorption properties of the sample within the sphere (See 2.2 *Experimental* section for details). However, even with the added detection abilities granted by a the ultra-sensitive power meter, the absorption value causes the largest error in UCNC absolute quantum yield measurements, as UCNCs absorb so few photons relative to the high incident laser powers, that are near the same value of the inherent A -value measurement in regards to that stability of the laser and power meter. To this end, however, the system was engineered with an internally mounted NIST calibrated lamp in the sphere that spectrally standardizes the CCD-spectrometer from arbitrary intensity counts to Watts per wavelength (W/nm) over the entire wavelength regime. Since the CCD-spectrometer can measure spectral emission in Watts via the aforementioned flux calibration, the total radiant flux can be calculated straightforwardly from the integrated emission flux per unit volume of direct and indirect excitations with error only induced by sphere, laser and CCD-spectrometer uncertainties, which was calculated by BAM Federal Research Institute to be approximately 8% using similar system components as those used for organic quantum yields.⁶¹ Thus, the total radiant flux is expressed in Watts of light emitted per volume of sample with much higher certainty.

To first compare this custom-engineered quantum yield measurement system with prior bulk-measured samples,^{10,13,14} and to provide a benchmark measurement of a commercially available bulk-phase upconversion material, [NaYF₄; Yb (20%), Er (3%)] (Sigma Aldrich)] was utilized for solid-state quantum yield and total radiant flux measurements. To make the bulk standard sample, a machine-press was used to press the commercial [NaYF₄; Yb (20%), Er (3%)] powder at 1000 psi at a density of 1 mg/mm, where a square piece having dimensions of approximately 8 by 8 mm was cut using a razor blade and mounted on the inside of a 1 cm cuvette (**Figure 3**). A CW laser power of 25 W/cm² was utilized as the excitation source; this laser power density is readily attainable with most small diode lasers, and is comparable to the laser power laser densities utilized in previous experiments that reported quantum yields of bulk upconverting phosphores.^{10,13}

Table 1: Absolute quantum yield and total radiant flux measurements of the as prepared and CW excited commercially available [NaYF₄; Yb (20%), Er (3%)] upconversion phosphor at 25 W/cm². This radiant flux was not converted to a volume as it was measured in the solid-state.

Sample Mass	Trial	Laser Power (W/cm ²)	A	Total QY (500-700 nm)	Total Radiant Flux (W)
69mg (Day 1)	a1	25.2	0.12	6.7%	0.0073
	a2	25.2	0.11	6.7%	0.0070
	a3	25.2	0.11	6.9%	0.0070
	a4	25.2	0.11	7.3%	0.0075
	a5	25.2	0.11	6.9%	0.0071
	a6	25.1	0.11	7.3%	0.0076
55 mg	b1	25.1	0.11	7.5%	0.0072
	b2	25.1	0.11	6.9%	0.0066
	b3	25.2	0.10	6.9%	0.0064
66 mg	c1	25.2	0.13	6.4%	0.0074
	c2	25.3	0.13	6.5%	0.0075
	c3	25.4	0.13	6.6%	0.0076
Average				6.9%	0.0072
Uncertainty				0.5%	0.0005

Three separate samples were measured under these conditions, with the total integrated spectrum from 500 -700 nm giving a quantum-yield of $6.9 \pm 0.5\%$ (**Table 1**). The error is calculated based on the uncertainty of the absorption value, A, which is deduced from error of propagation analysis on the standard deviation of the A-value measurements. The quantum yield value measured herein is in a similar range as prior literature values that report approximate quantum yield values that range from ~3 - 13% for varying and unspecific sampling preparations of bulk [NaYF₄; Yb, Er] compositions.^{10,13,14} The total radiant flux was measured to be 0.0072 ± 0.0005 W of output from an excitation density of 25.2 W / cm²; no volume correction was made to this number due to the pressed disk being fractions of a millimeter thick.

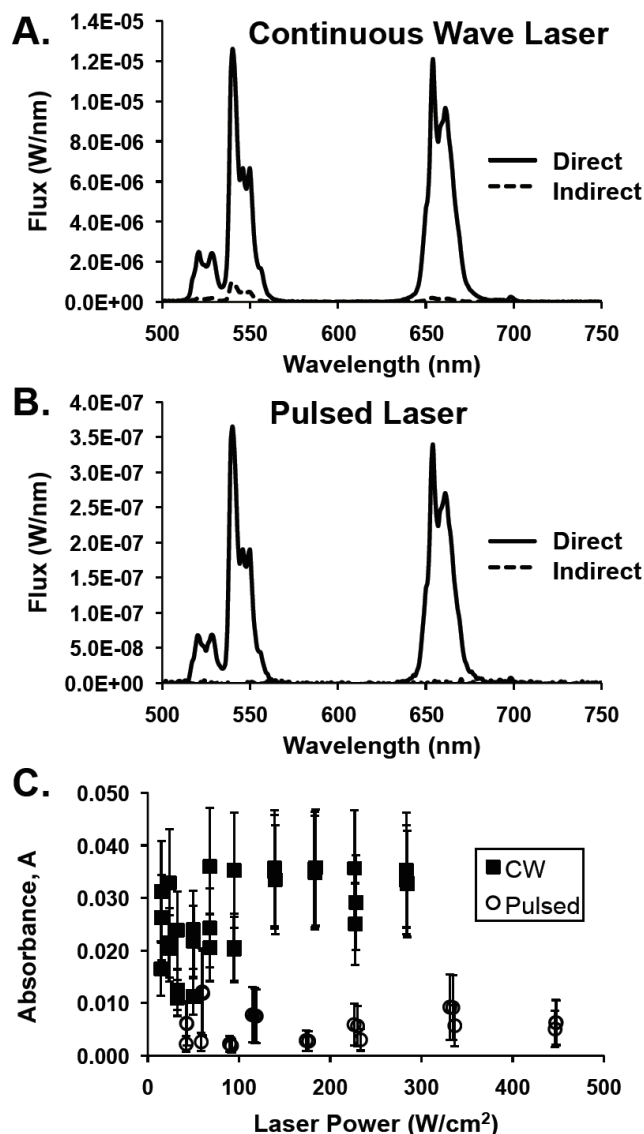


Figure 6: Upconversion spectra acquired for both direct (L_d) and indirect (L_b) laser excitation of 28 nm diameter $[\text{NaYF}_4; \text{Yb} (15\%), \text{Er} (2\%)]$ nanocrystals in toluene solution: (A) CW light source; (B) fs-pulsed light source (140 fs pulse-width, 80 MHz). Experimental conditions: laser power = 225 W/cm²; sample concentration = 1 mg/mL solution. (C) The absorbance value, A, plotted as a function of laser excitation type and power, with associated error bars.

Figure 6 displays the spectral response of a 1 mg/mL solution of $[\text{NaYF}_4; \text{Yb} (15\%), \text{Er} (2\%)]$ upconversion nanocrystals in toluene under 970 nm CW excitation (**Figure 6A**) and 976 nm fs-pulsed Ti-Sapphire excitation conditions (**Figure 6B**) at identical power densities (225 W/cm²); **Figure 6A-B** displays spectra acquired using

direct and indirect laser excitation. The 540 nm centered $^2H_{11/2}/^4S_{3/2} \rightarrow ^4I_{15/2}$ emissive band was integrated from 510 - 565 nm, and the 660 nm centered $^4F_{9/2} \rightarrow ^4I_{15/2}$ emissive band was integrated from 645 - 680 nm for all calculations. Under CW irradiation, re-emission was detected using indirect sample excitation at $3.6 \pm 1.4\%$ of the directly excited emission intensity, whereas the sample excited by the fs-pulsed laser shows virtually no detectable indirectly excited emission. The fact that no indirect emission was measured under fs-pulsed excitation however is not surprising given that the total power injected into the sphere is much less due to the fs-pulsed laser beam-diameter being significantly smaller (0.0018 cm^2) than that of the CW laser (0.043 cm^2). These data indicate that under CW excitation, the upconverted emission recorded in a direct excitation measurement features an emission contribution that derives from indirect excitation (reflected laser light that passed through the sample) within the sphere that should be accounted for in quantitative measurements. The absorbance value, A , is plotted in **Figure 6C** as a function of incident power. The UCNCs under CW excitation absorbed, on average, 2 times more photons than the same sample under fs-pulsed excitation conditions for equivalent laser densities recorded from over a range of 42 - 284 W/cm^2 , with the CW average A -value of 0.027 and the fs-pulsed absorbance average A -value of 0.005. However, inherent system absorption value measurement error is, on average, equal to an A -value of 0.017 with a standard deviation of 0.005 using undoped, 28 nm NaYF_4 nanocrystals. Therefore, using error of propagation analysis of the A -value measurement error, and the standard deviation of the doped 28 nm [NaYF_4 ; Yb (15%), Er (2%)] A -values, the reported absolute quantum yield error is 31% and 68% of the calculated value for CW and fs-pulsed excitation, respectively. While these uncertainties are high, they are on par with those measured previously for UCNCs,¹⁰ which suggests that quantum yield numbers should be used with caution when comparing UCNC

emission metrics. On the other hand, it's the ability to directly measure the total radiant flux via the flux corrected CCD-spectrometer that truly sets these measurements and system apart from previous studies, forgoing any reliability on the error prone UCNC quantum yield measurement, and having the ability to quantify the direct and indirect absorption and emission by the three-position absolute determination. In this case, where the A-value is very small (<0.1), the total radiant flux can be calculated simply by the directly-excited sample integrated emission flux minus the indirectly-excited integrated emission flux; this measurement methodology allows the ability to make quantitative measurements under more dilute conditions, such as 1 mg/mL presented herein, that will limit inner-sphere indirect absorption and emission properties, as well as concentration induced particle aggregation, for more accurate and precise quantitative determinations of particle light output.

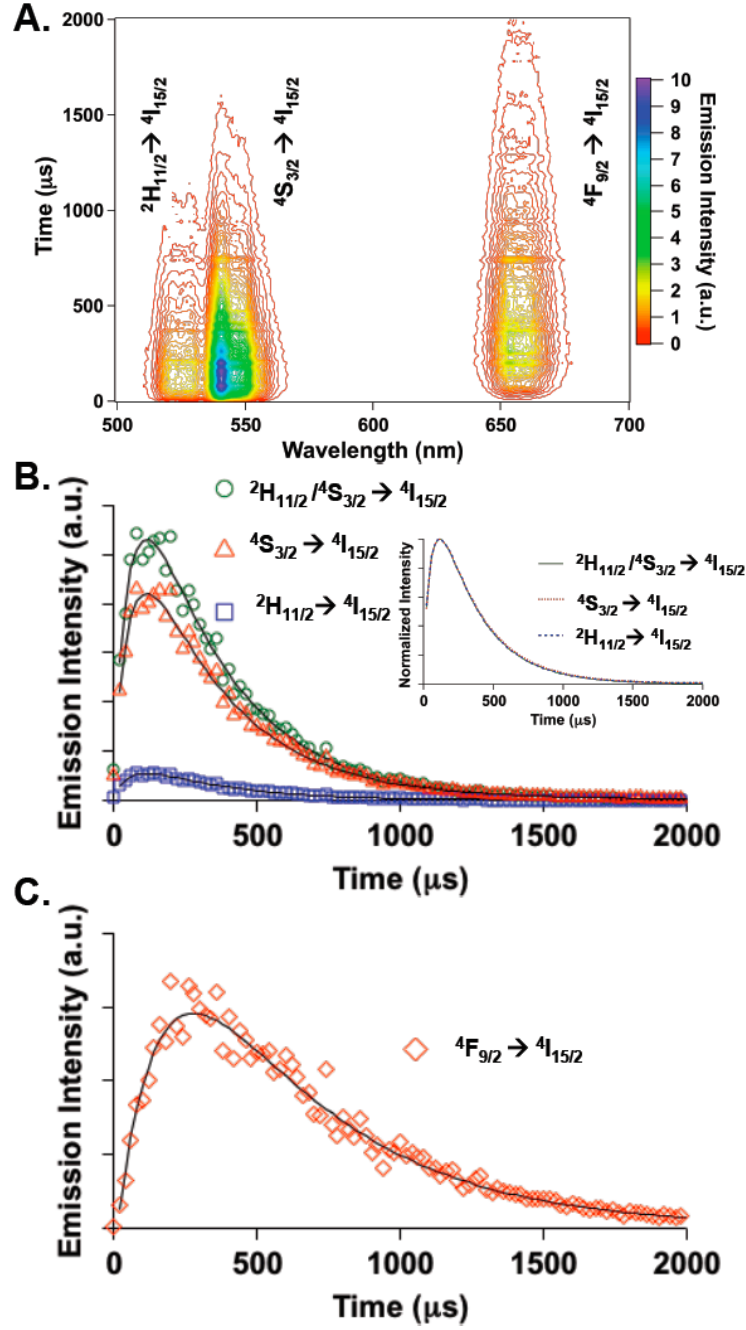


Figure 7: Contour plot of the emission intensity with respect to time and wavelength (A), lifetime fitting of the $2H_{11/2} \rightarrow 4I_{15/2}$ (510 - 525 nm), the $4S_{3/2} \rightarrow 4I_{15/2}$ (535 - 565 nm), and the fully integrated $2H_{11/2}/4S_{3/2} \rightarrow 4I_{15/2}$ (510 - 565 nm) transitions showing a rise-time of 62 μs and decay time of 302 μs (B) and the normalized overlap of the fitting traces (B, inset), and the lifetime fitting of the $4F_{9/2} \rightarrow 4I_{15/2}$ (645 - 680 nm) transition with a 161 μs rise and 488 μs decay lifetime. The raw data is presented by open shapes, with solid lines for the exponential fitting in B,C.

Solid-state luminescence lifetimes of the [NaYF₄; Yb (15%), Er (2%)] upconversion nanocrystals were measured from 976 nm nano-second pulsed excitation using time gating of an ICCD-camera equipped spectrometer such that the emissive bands could be spectrally separated for kinetic analysis in a time versus wavelength contour plot (**Figure 7**). As can be seen from the kinetic fitting and normalization of the 510 - 565 nm emission (**Figure 7B** and inset, raw data is presented by open shapes), the $^2\text{H}_{11/2} \rightarrow ^4\text{I}_{15/2}$ (510 - 525 nm), the $^4\text{S}_{3/2} \rightarrow ^4\text{I}_{15/2}$ (535 - 565 nm), and the fully integrated $^2\text{H}_{11/2}/^4\text{S}_{3/2} \rightarrow ^4\text{I}_{15/2}$ (510 - 565 nm) wavelength regions obey the same upconversion kinetics, with an identical fitting of a $62 \pm 2 \mu\text{s}$ rise-time and $302 \pm 3 \mu\text{s}$ decay-time. These data support the hypothesis that the upconversion pathways that populate and subsequently radiatively decay from the $^2\text{H}_{11/2}/^4\text{S}_{3/2}$ states of the Er³⁺ ion are nearly identical, allowing for their combined quantitative photophysical measurements to be examined. **Figure 7C** shows the kinetics for the $^4\text{F}_{9/2} \rightarrow ^4\text{I}_{15/2}$ (645 - 680 nm) transition, fit with a single rise component of 161 μs and a decay lifetime of 488 μs . Following the upconversion mechanisms that populate these emissive states, the $^2\text{H}_{11/2}/^4\text{S}_{3/2} \rightarrow ^4\text{I}_{15/2}$ states are populated by a quasi-resonant two photon process from 976 nm excitation, as shown by the radiant flux data in **Figure 8** with a power dependent slope of 1.7. On the other hand, the $^4\text{F}_{9/2} \rightarrow ^4\text{I}_{15/2}$ population is a result of non-radiative energy transfers through multiple phonon-coupled events, either from the earlier populated $^2\text{H}_{11/2}/^4\text{S}_{3/2}$ states or from other, lower lying Er³⁺ states, such as the $^4\text{I}_{13/2}$, which are populated after phonon relaxation from the initially excited Yb³⁺ $^2\text{F}_{5/2}$ state resonant with the excitation laser at 976 nm. These population mechanisms explain the much faster rise and decay components of the $^2\text{H}_{11/2}/^4\text{S}_{3/2}$ states relative to the $^4\text{F}_{9/2}$ state in f-block manifold of the Er³⁺ in these nanocrystals.

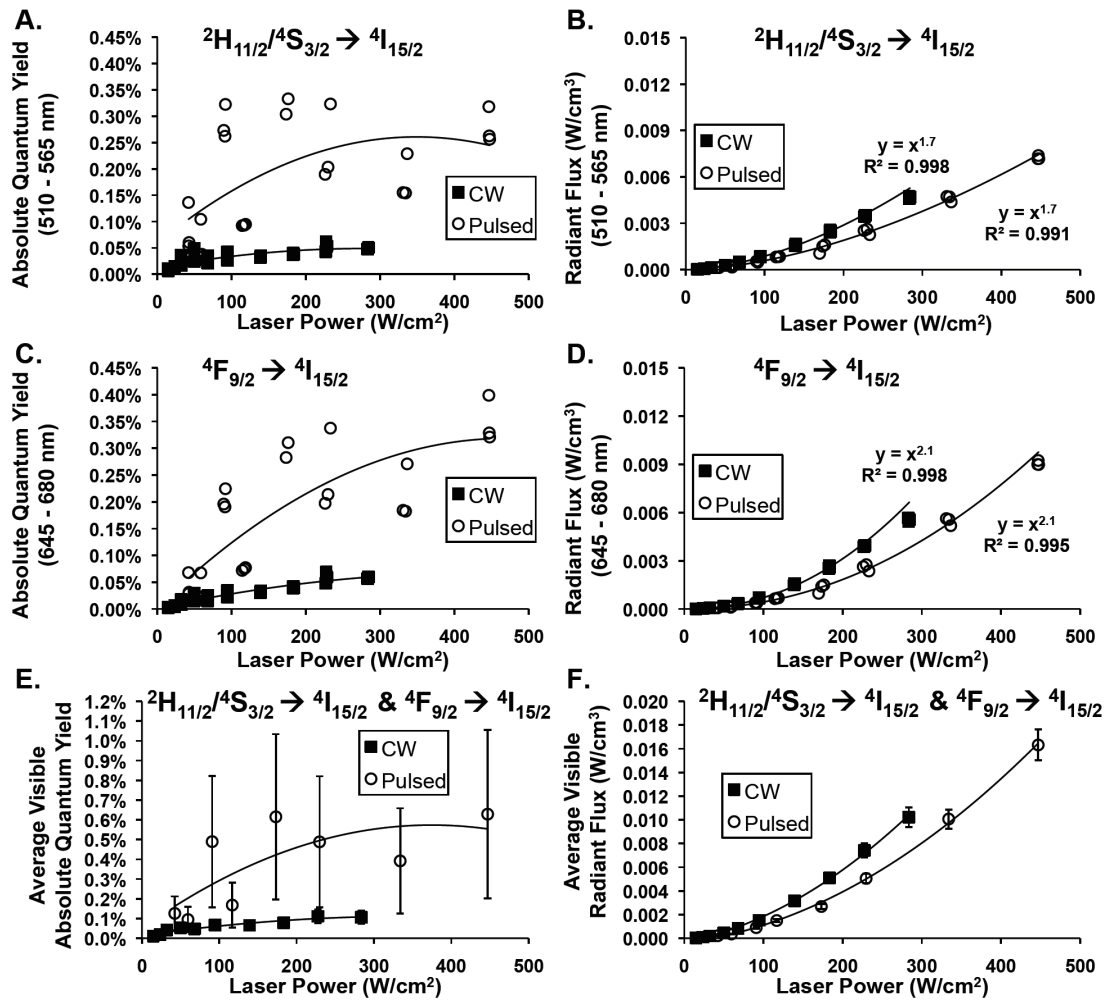


Figure 8: The absolute quantum yield and sample volume corrected total radiant flux under 970 nm CW and 976 nm fs-pulsed laser (140 fs pulse-width, 80 MHz) excitation of: (A, B) the $2H_{11/2}/4S_{3/2} \rightarrow 4I_{15/2}$ luminescence integrated from 510 - 565 nm, (C, D) the $4F_{9/2} \rightarrow 4I_{15/2}$ luminescence integrated from 645 - 680 nm, and (E, F) the averaged quantum yield and total radiant flux results of the entire visible spectrum by addition of both the $2H_{11/2}/4S_{3/2} \rightarrow 4I_{15/2}$ and $4F_{9/2} \rightarrow 4I_{15/2}$ transitions. Figures B,D have been fit with power law functions to highlight the number of photons responsible for each transition, while Figures A,C,E,F have added trend-lines to guide the eye. Figures E,F have error bars respective of the measurements' uncertainty.

The total radiant flux and absolute quantum yield measurements for the power-dependent CW and fs-pulsed excitation experiments for 1 mg/mL solutions of 28 nm [NaYF₄; Yb (15%), Er (2%)] upconversion nanocrystals are presented in Figure 8 in relation to the incident power density; the $2H_{11/2}/4S_{3/2} \rightarrow 4I_{15/2}$ emissive band (510 - 565

nm) measurements are shown in **Figure 8A-B**, the ${}^4F_{9/2} \rightarrow {}^4I_{15/2}$ emissive band (645 - 680 nm) measurements are shown in **Figure 8C-D**, and the sum of both the ${}^2H_{11/2}/{}^4S_{3/2} \rightarrow {}^4I_{15/2}$ and ${}^4F_{9/2} \rightarrow {}^4I_{15/2}$ emissions are shown in **Figure 8E-F**. **Figure 8A,C,E,F** display trend-lines added as visual guides, while the radiant flux data in **Figure 8B,D** have been fit with a power law to estimate the number of photons required for each emissive state to be populated. The total radiant flux values have been normalized to an excitation volume of 1 cm^3 based on the collimated laser excitation beam-diameter forming a cylinder through a $1 \text{ cm} \times 1 \text{ cm}$ cuvette. However, since the quantum yield is a unitless ratio of purely absorbed versus emitted photons, sampling volume has no effect on the outcome of this value, as it cancels out of the quantum yield equation.

Under CW excitation, a peak emission quantum yield for the combination of both the ${}^2H_{11/2}/{}^4S_{3/2} \rightarrow {}^4I_{15/2}$ and ${}^4F_{9/2} \rightarrow {}^4I_{15/2}$ transitions was measured to be $0.11 \pm 0.03 \%$ at the highest power density of 283 W/cm^2 , while under the fs-pulsed laser excitation, the highest quantum yield was $0.63 \pm 0.43 \%$ at 447 W/cm^2 (**Figure 8E-F**). **Figure 8A,C** show that as incident laser power increases, the ${}^2H_{11/2}/{}^4S_{3/2} \rightarrow {}^4I_{15/2}$ emission begins to reach quantum yield saturation as shown by decreasing slope of the respective trend-lines. However, the ${}^4F_{9/2} \rightarrow {}^4I_{15/2}$ quantum yield continues to increase almost linearly until the highest powers tested herein, with only a slight decrease in the trend-line slope. This fact is congruent with the radiant flux measurements under comparable laser densities, where the ${}^4F_{9/2} \rightarrow {}^4I_{15/2}$ radiant flux surpasses that for the ${}^2H_{11/2}/{}^4S_{3/2} \rightarrow {}^4I_{15/2}$ transitions as laser power increased over 250 W/cm^2 (**Figure 8B,D**). The peak total radiant flux of the combined ${}^2H_{11/2}/{}^4S_{3/2} \rightarrow {}^4I_{15/2}$ and ${}^4F_{9/2} \rightarrow {}^4I_{15/2}$ transitions was measured to be $0.010 \pm 0.001 \text{ W/cm}^3$ under CW excitation at 283 W/cm^2 , and $0.016 \pm 0.001 \text{ W/cm}^3$ under fs-pulsed oscillator excitation at 447 W/cm^2 (**Figure 8E-F**). Of note, the quantum yield under fs-pulsed excitation is greater than CW excitation, but the total radiant flux is

higher under CW excitation. However, since the quantum yields are nearly within error of each other due to the uncertainty in the as measured A-value, the quantum yield values under CW and fs-pulsed excitation can be treated as nearly indistinguishable. On the other hand, the higher radiant flux values measured under CW excitation over the comparable power density ranges interrogated is statically higher than those by the fs-pulsed excitation, although by only within a factor of two.

The quantitative photophysical data in **Figure 8** depict several characteristics of the power and pulse dependent photophysics associated with this nanocrystalline upconversion material. The most obvious feature is that the total radiant flux of this UCNC composition is nearly identical per unit volume excited by the CW and fs-pulsed laser excitation conditions used herein, with the CW excitation being only slightly greater than the fs-pulsed excitation. Thus, this data suggest that for this UCNC composition, that it is the average power, not peak (pulse) power, that dictates the emission. This can be related to the pulse-repetition-rate of a 80 MHz laser, where fs-pulses arrives every 12 ns, being only a very small fraction of microsecond rise and decay times displayed by these UCNCs. **Figure 8B,D** shows that radiant flux saturation starts to occur for CW and fs-pulsed excitation, as shown by the deviation of data points from the power function fitting at greater than 200 W/cm² for CW and greater than 400 W/cm² for fs-pulsed excitations. The nearly identical power-law fitting values for the power-dependence of the transitions under both CW and fs-pulsed excitation, 1.7 for the $^2\text{H}_{11/2}/^4\text{S}_{3/2} \rightarrow ^4\text{I}_{15/2}$ transition and 2.1 for the $^4\text{F}_{9/2} \rightarrow ^4\text{I}_{15/2}$ transition shown in **Figure 8B,D**, suggests that there is no significant alteration in the upconversion mechanisms that give rise to the population of the $^2\text{H}_{11/2}/^4\text{S}_{3/2}$ and $^4\text{F}_{9/2}$ states that is laser type-dependent, signifying the fs-pulsed laser isn't inducing additional linear or non-linear effects from high-peak power excitation at the Yb³⁺ $^2\text{F}_{5/2}$ 976 nm resonant excited state. To note,

however, it that during fs-pulsed *in vitro* biological imaging, it is possible that a 80 MHz fs-pulsed source, focused down by an objective to a spot size on the order of a few microns, could cause augmented radiant flux due to the probability of resonantly enhanced instantaneous two-photon absorption via the $\text{Yb}^{3+} {}^2\text{F}_{5/2}$.⁶⁶ However, the CW excitation data shown herein that displays more radiant flux per comparable excitation density than the fs-pulsed excitation, as well as the work already performed using CW excitation for *in vitro* biological imaging,^{17,19-29} cellular tracking,^{16,30} and photodynamic therapy,³¹⁻³³ even *in vivo*^{16,19} and whole body^{17,20,24,25,34} imaging, underscores the potential utility of the much lower costing CW sources compared to their fs-pulsed counterparts for ultra-sensitive, straightforward UCNC-based imaging applications. It is further worthwhile to note that for whole body imaging, incident laser power densities must be greatly reduced when compared to the potential 100 W/cm²-plus densities used in microscope-based imaging due to the highly focused excitation objectives, with a conservative threshold for human skin exposure being 726 mW/cm² of CW 980 nm.⁶⁷ Nevertheless, several reports have already shown superb whole-body small animal imaging at powers ranging from 2.6 - 250 mW/cm² using CW sources,^{20,24,34} exemplifying again the possibilities for UCNC biological imaging from inexpensive CW diode laser sources.

2.4 Conclusions

In conclusion, the power-dependent total radiant flux and absolute quantum yield measurements of a homogeneous, solution-phase upconversion nanocrystal composition were recorded, which directly compared these metrics under 970 nm CW and 976 nm fs-pulsed Ti-Sapphire laser excitation (140 fs pulse-width, 80 MHz). This study illustrates that at comparable excitation densities under continuous-wave and fs-pulsed excitation from 42 - 284 W/cm², the absolute quantum yield is higher under fs-

pulsed laser excitation, whereas the total radiant flux is higher under continuous-wave excitation, when spectra are integrated over the 500 - 700 nm wavelength regime. This study further establishes the radiant flux as the true unit of merit for quantifying emissive output intensity of upconverting nanocrystals for application purposes, especially given the high uncertainty in solution phase upconversion nanocrystal quantum yield measurements due to their low absorption cross-section. These measurements were accomplished using a custom-engineered, multi-detector integrating sphere measurement system utilizing a three-position sample-measurement methodology described by de Mello, Whitmann, and Friend,⁶⁵ that can directly measure the total radiant flux via a spectral-flux calibrated CCD-spectrometer. The hexagonal-phase [NaYF₄; Yb (15%), Er (2%)] nanocrystals were characterized by transmission electron microscopy (TEM), x-ray diffraction (XRD), and inductively coupled plasma atomic emission spectroscopy (ICP-AES). Solid-state emission lifetime measurements conclusively showed that the ²H_{11/2} (525 nm) and ⁴S_{3/2} (545 nm) states display identical rise and decay single-exponential time constants, prompting their combination in the quantum yield and radiant flux calculations. Further, a commercially available upconversion material, [NaYF₄; Yb (20%), Er (3%)] was acquired and measured in the solid-state at 25 W/cm² to provide a quantitative standard for radiant flux and absolute quantum yield research in this field. Given that the radiant flux is the figure of merit for determining how emissive a sample will be based on its composition, volume, and excitation conditions, as well as upconversion nanocrystals in solution displaying quantum yields with large uncertainties, this study proves that utilization of new techniques and superior light metrology will dictate the applicability of next-generation UCNCs for light-based applications such as biological imaging.

Acknowledgement. I would like to thank Jennifer A. Ayres, Joshua T. Stecher, Dan Scharpf, Jonathan D. Scheuch, and Michael J. Therien for their contributions to this work.

3. Dual energy converting nano-phosphors: upconversion luminescence and X-ray excited scintillation from a single composition of lanthanide-doped yttrium oxide

An upconverting nanomaterial composition, [Y₂O₃; Yb (2%), Er (1%)], that converts both X-ray and high-fluence NIR irradiation to visible light, is presented. This composition is compared to a higher Yb³⁺-doped composition, [Y₂O₃; Yb (10%), Er (1%)], that displays diminished visible X-ray scintillation, but shows enhanced red wavelength centered upconversion emission. These nanocrystals have been characterized by TEM, X-ray diffraction, power-dependent upconversion luminescence, and X-ray scintillation spectroscopy. It is further demonstrated that lithium ion doping of the [Y₂O₃; Yb (2%), Er (1%)] nanoscale composition leads to enhanced X-ray and NIR excited emission intensities through the production of nanoparticles that feature slightly enhanced sizes and increased crystallinity.

3.1 Introduction

Photonic applications of lanthanide-based nanoscale materials are widespread, and range from medical imaging^{15,19} to radiation detection.⁴³ Yttrium oxide (Y₂O₃) and its lanthanide-doped ([Y₂O₃; Ln]) analogues manifest extreme thermal stability, are robust under wide-ranging environmental conditions, and can be readily synthesized on the nanometer scale.⁶⁸⁻⁷³ Under appropriate excitation conditions, [Y₂O₃; Ln] compositions can emit light at specific wavelengths over ultraviolet (UV) through near-infrared (NIR) spectral regimes. High energy excitation sources (x-ray,⁷⁴ electron beam,^{38,75-77} and UV^{73,78}) give rise to downconversion emission at wavelengths longer than the excitation source, while high-fluence NIR laser excitation at 980 nm drives upconversion emission at higher energy NIR, visible, and UV wavelengths.^{72,78-82} Upconversion emission is enabled through multi-photon absorption processes that take advantage of long-lived

lanthanide ion electronically excited states and non-resonant phonon-coupled energy-transfer processes.^{1,83,84} Energy conversion involving Y₂O₃-based nanoscale materials have focused typically on processes that give rise to either downconversion or upconversion luminescence; few studies have examined compositions that support energy conversion of both high and low energy excitation.^{78,85} To date, no nanoscale compositions have been identified that manifest both x-ray-excited scintillation (XES) and upconversion luminescence (UCL) driven by 980 nm irradiation.

This chapter presents a lanthanide-based upconverting nanocrystalline composition, [Y₂O₃; Yb (2%), Er (1%)] (**Yb2Er1**), that displays both upconverted visible wavelength luminescence generated via 980 nm laser excitation, and XES (excitation power: 130 kVp at 5 mA). While eleven rare-earth ions have been shown to emit via absorption of ionizing radiation when doped into yttria,⁷⁷ **Yb2Er1** is the first such nanocrystalline composition to demonstrate Er³⁺-derived XES in a Yb³⁺-containing matrix. **Yb2Er1** is thus unusual in that Er³⁺-derived XES is maintained at a Yb³⁺ concentration sufficient to support upconversion luminescence via 980 nm excitation. Note in this regard that Yb³⁺ ions typically function as a low energy electron and energy trap, suppressing co-dopant scintillation; this is confirmed by comparing **Yb2Er1** scintillation and upconversion properties to a higher Yb³⁺-doped composition, [Y₂O₃; Yb (10%), Er (1%)] (**Yb10Er1**). It is further demonstrated that lithium ion doping of **Yb2Er1**, [Y₂O₃; Yb (2%), Er (1%), Li (15%)] (**Yb2Er1Li5**), enhances both up- and downconversion emission intensity, and correlate the emissive enhancements to increases in material size and crystallinity.

3.2 Experimental

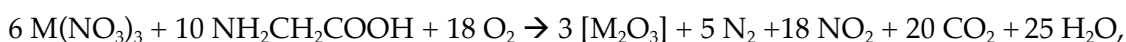
Materials:

$\text{Y}(\text{NO}_3)_3 \cdot 6\text{H}_2\text{O}$ (99.8%), $\text{Yb}(\text{NO}_3)_3 \cdot 5\text{H}_2\text{O}$ (99.9%), $\text{Er}(\text{NO}_3)_3 \cdot 5\text{H}_2\text{O}$ (99.9%), $\text{Li}(\text{NO}_3)$ (99.99%), and glycine ($\geq 99\%$) were purchased from Sigma-Aldrich and used without further purification. HPLC-grade H_2O was also used (Fisher Chemicals).

Synthesis of $[\text{Y}_2\text{O}_3; \text{Ln}]$:

$[\text{Y}_2\text{O}_3; \text{Yb} (2\%), \text{Er} (1\%)]$, $[\text{Y}_2\text{O}_3; \text{Yb} (10\%), \text{Er} (1\%)]$ and $[\text{Y}_2\text{O}_3; \text{Yb} (2\%), \text{Er} (1\%), \text{Li} (5\%)]$ were synthesized by a solution combustion synthesis involving glycine as the fuel.

The reaction is as follows:



where $\text{M} = \text{Y}, \text{Yb}, \text{Er}, \text{or Li}$. The glycine-to-metal nitrate molar ratio was kept at 1.5:1 to ensure consistency of the samples. In a typical synthesis, 25 mL of HPLC grade H_2O was used to dissolve a total 0.2 mol/L of metal-nitrates and 0.3 mol/L of glycine in a 100 mL beaker. **Table 2** shows the amounts based on this method for $[\text{Y}_2\text{O}_3; \text{Yb} (2\%), \text{Er} (1\%)]$.

Table 2: Theoretical amounts of precursors for $[\text{Y}_2\text{O}_3; \text{Yb} (2\%), \text{Er} (1\%)]$ based on a 25 mL solution.

	$\text{Y}(\text{NO}_3)_3 \cdot 6\text{H}_2\text{O}$	$\text{Yb}(\text{NO}_3)_3 \cdot 5\text{H}_2\text{O}$	$\text{Er}(\text{NO}_3)_3 \cdot 5\text{H}_2\text{O}$	glycine
mol / L (25 mL H_2O)	0.194	0.004	0.002	0.3
Mass (g)	1.858	0.045	0.022	0.563

After stirring until completely dissolved, the stir bar was removed and the reaction was placed on a hot plate set to maximum heat until combustion occurred, which took approximately 15 minutes. For safety purposes, the beaker and hot plate were enclosed by $\frac{1}{2}$ inch plexi-glass box during the reaction. Once the reaction occurred, the beaker was immediately removed from the hot plate and allowed to cool to room temperature. While most of the nanoparticle product remained in the beaker, a small amount of the white powder was also dispersed within the plexi-glass enclosure. All

powders were then collected in an aluminum oxide crucible and placed in a furnace at 500 °C for 1 hour under normal atmospheric conditions to burn off any residual nitrates. The powders were then experimentally tested as is.

Instrumentation:

X-ray Diffraction (XRD), Scanning Electron Microscopy (SEM), and Transmission Electron Microscopy (TEM) were performed at the *Shared Materials Instrumentation Facility* (SMiF) at Duke University.

X-ray Diffraction. Powder XRD was measured on a Philips X'Pert PRO MRD HR X-Ray Diffraction System from 25° - 75° (2 θ) under Cu K-Alpha (1.542 Å) irradiation at 45 keV and 40 mA.

Scanning Electron Microscopy. SEM was performed on a FEI XL30 SEM-FEG with a field emission source operating at 30 keV.

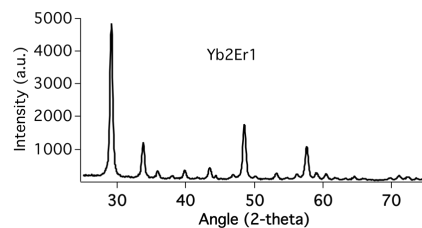
Transmission Electron Microscopy. TEM images were acquired on a FEI Tecnai G² Twin microscope operated at an accelerating voltage of 200 keV and equipped with a TIA digital camera. Sample preparation consisted of making a 1 mg/mL solution of bare nanocrystals in ethanol, sonicating the solution for 1 minute in a bath sonicator, and then placing several drops of this solution on a carbon-formvar 400 mesh copper grid (EMS).

Upconversion Luminescence (UCL). UCL spectra were measured on an Edinburgh FLSP920 equipped with a Hamamatsu R2658 PMT. Solid samples (5 mg) were mounted in the spectrometer using a 100 micron Starna Cell powder sample holder and excited using an OEM Laser Systems 980 nm laser diode with tunable power. The emissions from the powder were passed through a Schott KG-5 filter to minimize scatter noise from high excitation densities and spectra were collected from 350-680 nm. All spectra were corrected for spectral throughput and detector sensitivity based on calibrations from a NIST calibrated light source provided by Edinburgh Instruments.

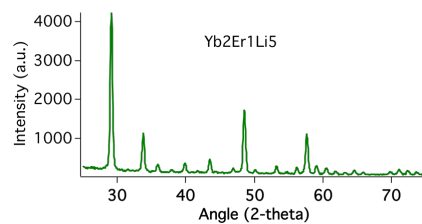
X-ray Excited Scintillation (XES). XES spectra were measured on an Edinburgh FLSP920 equipped with a Hamamatsu R2658 PMT over the range from 350 – 680 nm. A Faxitron RX-650 X-Ray Cabinet fiber coupled (Ocean Optics 400 μm) to the Edinburgh FLSP920 detection system allows for XES measurements with excitation powers ranging from 30 - 130 keV at a constant current of 5 mA. For measurements, 5 mg of powder were pressed into a 7 mm diameter pellet using a Pike Technologies' hand press and placed on a piece of Teflon in the x-ray cabinet. The sample was aligned with the mounted fiber for maximum light collection; optimum alignment was verified by maximizing the emission intensity for each sample.

3.3 Results and Discussion

A.



B.



C.

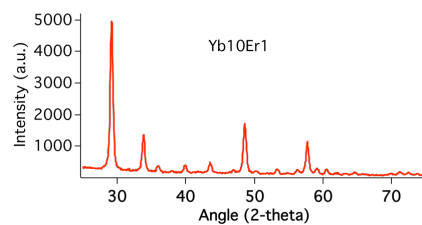
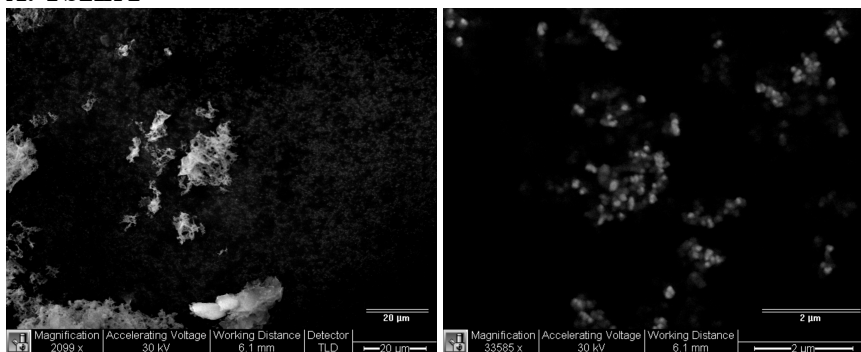
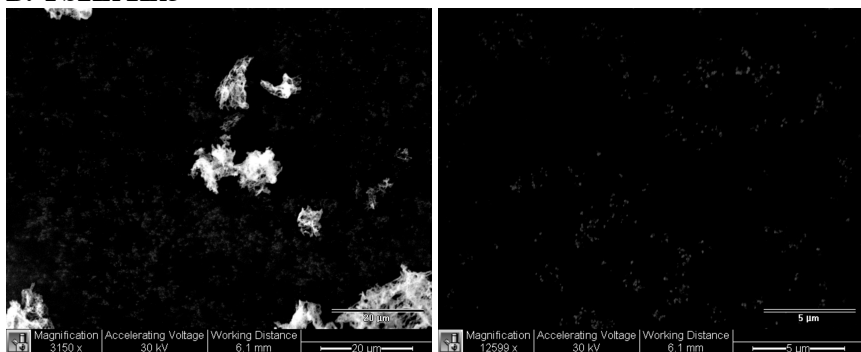


Figure 9: X-ray diffraction patterns of Yb₂Er₁ (A), Yb₂Er₁Li₅ (B) and Yb₁₀Er₁ (C). These spectra match the JCPDS-88-1040 Index for cubic yttrium oxide demonstrating all compositions are crystalline and cubic.

A. Yb₂Er₁



B. Yb₂Er₁Li₅



C. Yb₁₀Er₁

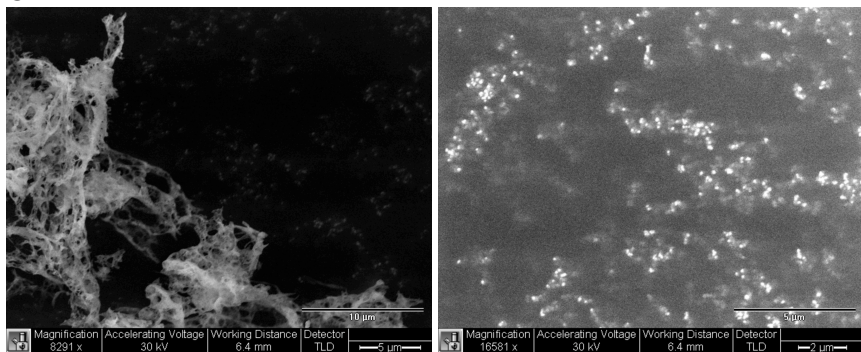
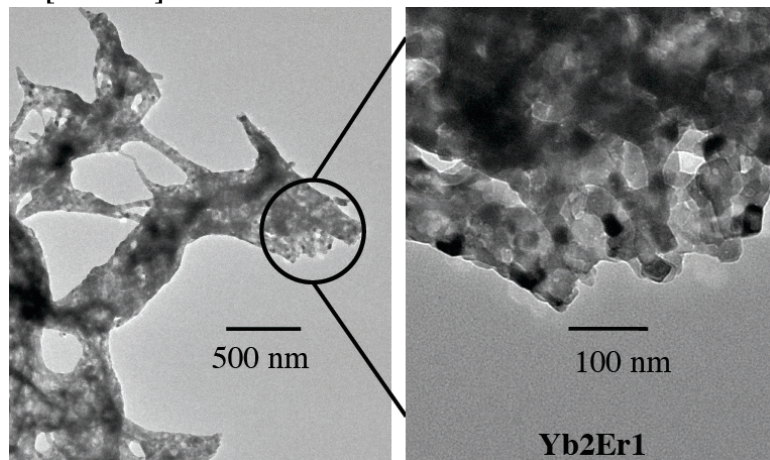


Figure 10: Exemplar SEM images of Yb₂Er₁ (A), Yb₂Er₁Li₅ (B), and Yb₁₀Er₁ (C), highlighting the small, individualized nanocrystals as well as the micron sized “coral-like” structures present in all samples with and without lithium.

The combustion synthetic approach^{68,80} was utilized to produce [Y₂O₃; Yb, Er, +/- Li] nanocrystals, **Yb2Er1**, **Yb10Er1**, and **Yb2Er1Li5**. Incorporation of lithium ions into the [Y₂O₃] matrix has been shown to enhance extrinsic, dopant-centered emissions under ionizing and electron beam radiation conditions (*e.g.*, the Y₂O₃; Eu red phosphor),^{71,75} and in specific Yb³⁺-, Er³⁺-, Tm³⁺-, and Ho³⁺-doped compositions that generate upconversion luminescence under 980 nm excitation.^{81,86,87} X-ray diffraction data (XRD; **Figure 9**) confirmed formation of the cubic phase (space group Ia3, JCPDS-88-1040) for all compositions. Scanning electron microscopy (SEM) data indicate porous, fractal-like Y₂O₃ structures for dispersed **Yb2Er1**, **Yb10Er1**, and **Yb2Er1Li5** nanocrystals (**Figure 10**), congruent with that reported previously for other lanthanide-based nanostructures fabricated via this method.⁷⁰ Transmission electron microscopy (TEM) of **Yb2Er1** and **Yb2Er1Li5** confirmed that the observed micron-sized features derive from fused nanoparticle units arranged in coral-like structures (**Figure 11**). Analysis of these TEM images reveals diameters of ~20 – 25 nm and ~40 – 70 nm, for the respective **Yb2Er1** and **Yb2Er1Li5** nanoparticles. Further comparison of **Yb2Er1** and **Yb2Er1Li5** TEM images in **Figure 11** evinces that addition of lithium ions affects crystalline properties beyond size; the lithium ion-doped nanocrystals exhibit reduced amorphous structure and better-defined individual nanocrystalline boundaries.

A. [Yb₂Er₁]



B. [Yb₂Er₁Li₅]

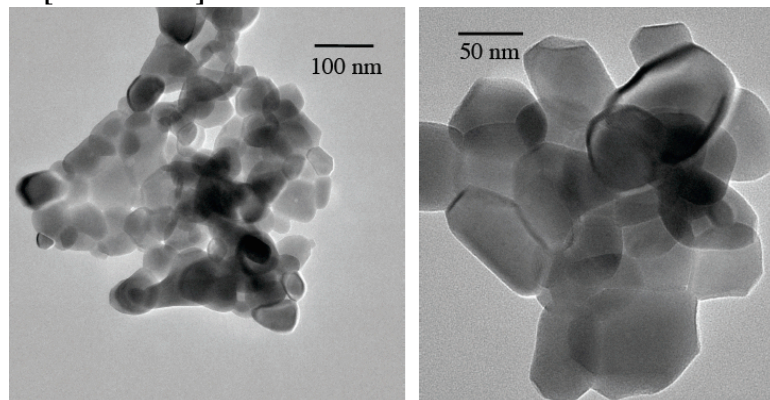


Figure 11: TEM images of Yb₂Er₁ (A) and Yb₂Er₁Li₅ (B), showing how the micron-sized structures are actually composed of nanocrystallites. This further shows the effects of Li-doping, as the Yb₂Er₁Li₅ nanocrystals feature larger size and better particle crystallinity than their Yb₂Er₁ parent structures.

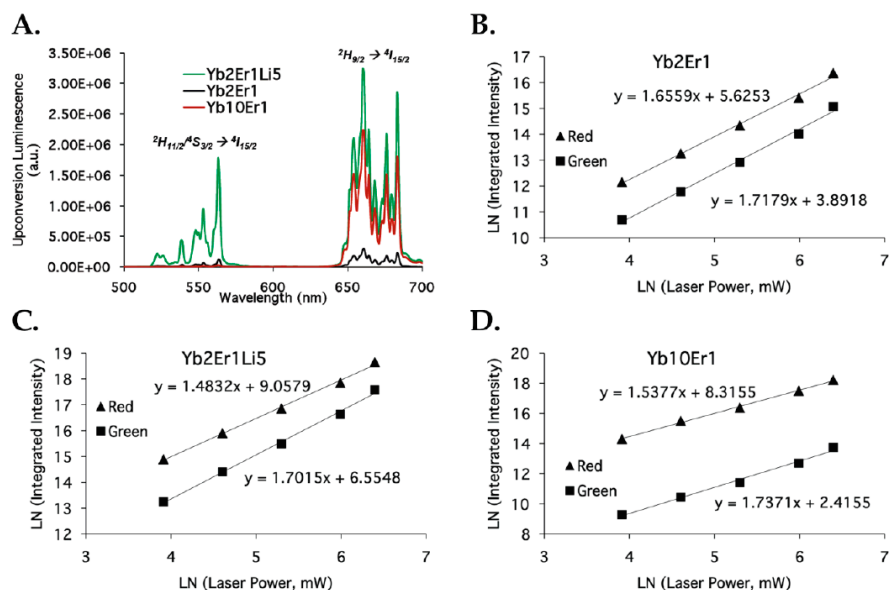


Figure 12: (A) Solid-state UCL spectra of Yb2ErLi5, Yb2Er1, and Yb10Er1 nanocrystals excited at 980 nm (laser power = 400 W/cm²), and the power-dependent integrated upconversion luminescence intensity of (B) Yb2Er1, (C) Yb2Er1Li5, and (D) Yb10Er1 over the green [$^2H_{11/2}/^4S_{3/2} \rightarrow ^4I_{15/2}$; 515 – 570 nm] and red [$^4F_{9/2} \rightarrow ^4I_{15/2}$; 645 – 690 nm] centered emission lines. Yb2Er1 and Yb2Er1Li5 both display green (565 nm) and red (670 nm) centered emissions, with the lithium-doped composition nearly an order of magnitude more emissive. Yb10Er1 displays red (670 nm) centered emission near intensity of Yb2Er1Li5, but displays almost no green (565 nm) emission.

Power-dependent, 980 nm-excited UCL spectra of the as synthesized nanocrystals display emission lines that span the visible through the NIR (**Figure 12**). 980 nm laser excitation populates the Yb³⁺ ion $^2F_{5/2}$ state, and the more weakly absorbing Er³⁺ $^4I_{11/2}$ state.⁸⁰ Appropriately high laser fluences drive population of higher energy Er³⁺ excited states via processes that include Er³⁺ $^4I_{11/2}$ excited state absorption (ESA) and energy transfer upconversion (ETU) involving the electronically excited Yb³⁺ $^2F_{5/2}$ state, and cross-relaxation between energy-matched excited states of Er³⁺ and Yb³⁺. Radiative transitions within the Er³⁺ *f*-block states produce green [$^2H_{11/2} \rightarrow ^4I_{15/2}$; $^4S_{3/2} \rightarrow ^4I_{15/2}$; 515 – 570 nm] and red [$^4F_{9/2} \rightarrow ^4I_{15/2}$; 645 – 690 nm] emission lines (**Figure 12A**). Analysis of the power-dependent upconversion luminescence intensity measured in all three

samples over the green [$^2H_{11/2} \rightarrow ^4I_{15/2}; ^4S_{3/2} \rightarrow ^4I_{15/2}$; 515 – 575 nm] and red [$^4F_{9/2} \rightarrow ^4I_{15/2}$; 645 – 690 nm] wavelengths indicates that these emission manifolds arise from two-photon processes (**Figure 12B-D**), concurrent with previous literature.⁸⁰ Comparison of **Yb2Er1** and **Yb2Er1Li5** power-dependent upconversion luminescence demonstrates that the lithium ion-doped nanocrystals display emission intensities that are nearly one order of magnitude larger than the **Yb2Er1** benchmark at all interrogated laser powers (**Figure 12B,C**). Note as well that the ratio of the [$^2H_{11/2}/^4S_{3/2} \rightarrow ^4I_{15/2}$]:[$^4F_{9/2} \rightarrow ^4I_{15/2}$] emissive transition intensities has increased in the lithium-doped sample,⁸¹ suggesting at least partial suppression of non-radiative processes involving relaxation from the Er^{3+} [$^2H_{11/2}/^4S_{3/2} \rightarrow ^4I_{15/2}$] manifold to the Er^{3+} [$^4F_{9/2} \rightarrow ^4I_{15/2}$] manifold. **Yb10Er1** displays red-centered [$^4F_{9/2} \rightarrow ^4I_{15/2}$] (670 nm) emission that approaches intensities similar to that of the **Yb2Er1Li5** sample. However, nearly all of the green-centered Er^{3+} [$^2H_{11/2}/^4S_{3/2} \rightarrow ^4I_{15/2}$] emission lines are suppressed in **Yb10Er2** through cross-relaxation processes involving appropriate states of close lying Er^{3+} and Yb^{3+} dopant ions.

XES stems from initial x-ray absorption, electron-hole (e^-h^+) pair generation, subsequent valence and conduction band energy trapping and collection, and ensuing radiative emission from lanthanide f -block states lying within the valence and conduction band gap.^{35,36} While XES in lanthanide (Ln^{3+})-doped inorganic crystals have been known for decades, these processes have rarely, if ever, been probed on the nanoscale; little is known, for example, regarding the x-ray absorptive cross-sections, scintillation efficiencies, and saturation thresholds of such materials. Data do suggest, however, that highly crystalline nanoparticles can in fact outperform their bulk counterparts on a per mass basis under low energy electron excitation conditions.⁴²

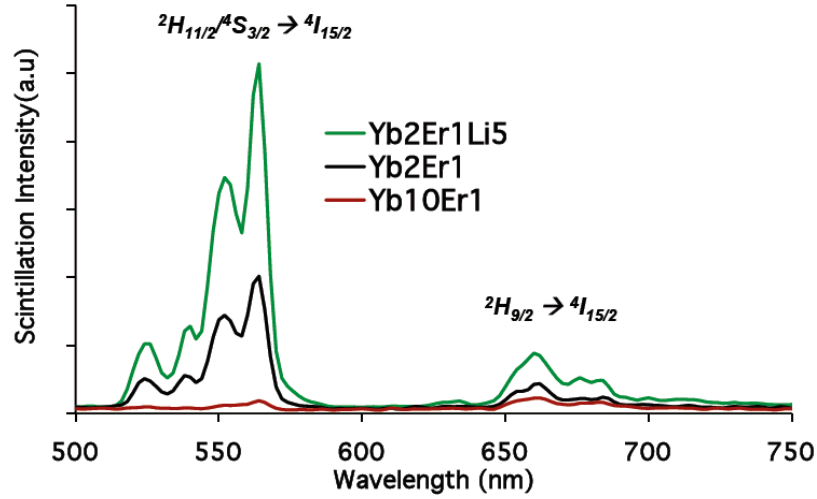


Figure 13: Solid-state x-ray excited scintillation (XES) spectra recorded for Yb2Er1Li5, Yb2Er1, and Yb10Er1 nanocrystals. Experimental conditions: x-ray source, 130 kVp (5 mA); T = 20 °C.

Figure 13 displays the XES spectral signatures of **Yb2ErLi5**, **Yb2Er1**, and **Yb10Er1** nanocrystals observed under 130 kVp (5 mA) x-ray excitation. Both **Yb2ErLi5** and **Yb2Er1** nanocrystalline compositions feature dominant emission manifolds centered near 565 nm (Er^{3+} : $^2\text{H}_{11/2}/^4\text{S}_{3/2} \rightarrow ^4\text{I}_{15/2}$). These emissive signatures closely resemble those previously observed for bulk-phase $[\text{Y}_2\text{O}_3; \text{Er}]$ samples subject to electron-beam excitation,⁷⁷ signifying that this Yb^{3+} dopant level does not give rise to complete scintillation quenching. Conversely, XES quenching is very apparent in the **Yb10Er1** composition, where nearly all scintillation is suppressed. Like the UCL data, the **Figure 13** spectra evince that the scintillation intensity manifested by nanocrystalline **Yb2Er1Li5** samples exceeds that of the parent **Yb2Er1** composition. Given Yb^{3+} 's role as a sensitizer in upconverting nanocrystals, it is clear that key design trade-offs are necessary for dual UCL and XES nanocrystals; optimizing 980 nm Yb^{3+} absorption for upconversion, while minimizing cross-ion quenching of states that give rise to scintillation suppression, thus

define key design challenges for elaboration of other nanomaterials that display dual up- and downconversion emission. High-resolution TEM images (**Figure 11**) qualitatively rationalize the origin of lithium ion doping emission intensity enhancements to UCL and XES. Lithium ion doping: (i) slightly increases nanocrystal size and thereby decreases the surface-to-volume ratio relative to the corresponding undoped composition, thus diminishing the proportion of surface defect sites and the extent of non-radiative relaxation involving surface OH vibrational modes, and (ii) gives rise to an apparent increase in crystallinity, correlating to more efficient electron-phonon coupling, stronger mixing of charge-transfer states, and reduced internal reflections within lanthanide-oxide nanoparticles.^{73,75,88-90}

3.4 Conclusion

In conclusion, it was demonstrated that a nanocrystalline material, **Yb2Er1**, can function as a dual energy converting phosphor under both x-ray and NIR laser irradiation conditions. Lithium ion doping of **Yb2Er1** enhances XES and UCL intensity; a larger nanocrystalline diameter and a visually apparent increase of composition crystallinity likely provide the genesis for this effect. Further, it was shown that increasing the Yb³⁺ concentration in these nanocrystalline compositions gives rise to dominant red upconversion emission, and suppresses scintillation through both cross relaxation and charge trapping processes. Given the utility for upconversion multi-modal imaging in medicine,⁹¹⁻⁹³ functionalized rare-earth doped nanomaterials that display XES and UCL should impact next-generation imaging methods that combine information gleaned from long-wavelength upconversion optical imaging and high-resolution x-ray luminescence computed tomography (XLCT).^{94,95}

Acknowledgement. I would like to thank Jennifer A. Ayres and Michael J. Therien for their contributions to this work, and Immunolight, LLC, and the National Science Foundation (NSEC DMR-0425780) for financial support.

4. A Fiber-Optic Radiation Detector Based on Europium-Doped Yttrium Oxide Nanocrystals that Provides a Linear Emissive Response to X-ray Radiation Exposure

Eu- and Li-doped yttrium oxide nanocrystals [$Y_{2-x}O_3; Eu_x, Li_y$], in which Eu and Li dopant ion concentrations were systematically varied, were developed and characterized (TEM, XRD, Raman spectroscopic, and ICP-AES data) in order to define the most emissive compositions under specific x-ray excitation conditions. These optimized [$Y_{2-x}O_3; Eu_x, Li_y$] compositions display scintillation responses that: (i) correlate linearly with incident radiation exposure at x-ray energies spanning from 40 - 220 kVp, and (ii) manifest no evidence of scintillation intensity saturation at the highest evaluated radiation exposures [up to 4 Roentgen per second]. For the most emissive nanoscale scintillator composition, [$Y_{1.9}O_3; Eu_{0.1}, Li_{0.16}$], excitation energies of 40, 120, and 220 kVp were chosen to probe the dependence of the integrated emission intensity upon x-ray exposure-rate in energy regimes where either the photoelectric or the Compton effect governs the scintillation mechanism: these experiments demonstrate for the first time for nanoscale [$Y_{2-x}O_3; Eu_x$], that for comparable radiation exposures, when scintillation is governed by the photoelectric effect (120 kVp excitation), greater integrated emission intensities are recorded relative to excitation energies where the Compton effect regulates scintillation (220 kVp excitation). Nanoscale [$Y_{1.9}O_3; Eu_{0.1}, Li_{0.16}$] (70 ± 20 nm) was further exploited as a detector material in a prototype fiber-optic radiation sensor. The scintillation intensity from the [$Y_{1.9}O_3; Eu_{0.1}, Li_{0.16}$]-modified, 400 μ m-sized optical fiber tip, recorded using a CCD-photodetector and integrated over the 605 - 617 nm wavelength domain, was correlated with radiation exposure using a Precision XRAD 225Cx small-animal image guided radiation therapy (IGRT) system. For both 80 and 225 kVp energies, this radiotransparent device recorded scintillation intensities that tracked linearly with total radiation exposure, highlighting its capability to provide alternately

accurate dosimetry measurements for both diagnostic imaging (80 kVp) and radiation therapy treatment (225 kVp).

4.1 Introduction

Inorganic scintillators have long been exploited as radiation sensing materials due to their high stabilities and emission characteristics, and the fact that the emissive wavelengths of these species are compatible with conventional photomultiplier tubes.³⁵⁻³⁷ Factors such as crystal growth conditions and the need for cryogenic cooling, for example, have limited the extent to which many of these materials can be deployed. Modern photodetectors, such as those based on CCD cameras and Si-photodiodes, enable enhanced scintillation emission detection sensitivities, and open up new possibilities to exploit scintillators that are smaller, easier to produce, and scintillate within the photodetector spectral regime that affords optimal quantum efficiency of the photovoltaic response (generally between 500-1000 nm).

Bulk yttrium oxide activated with europium ions, $[\text{Y}_2\text{O}_3; \text{Eu}]$, has been utilized as the red-phosphor in early cathode ray televisions³⁸ and as the scintillator material in a wide variety of x-ray computed tomography (CT) detectors.³⁹ Both of these applications exploit the material's peak emissions near 600 nm. While nanoscale $[\text{Y}_2\text{O}_3; \text{Eu}]$ has found utility in white light emitting diodes⁴⁰ and *in vitro* imaging,⁴¹ its x-ray scintillation properties have yet to be fully interrogated, despite the fact that the per-mass scintillation yield of $[\text{Y}_2\text{O}_3; \text{Eu}]$ nanocrystals exceeds that of their bulk counterparts under electron-beam excitation.⁴² Further, while scintillating nanomaterials have been delineated and demonstrate considerable potential,⁴³⁻⁴⁷ relatively little work has capitalized upon such materials in device architectures.

In this chapter, Eu- and Li-doped yttrium oxide nanocrystals $[\text{Y}_{2-x}\text{O}_3; \text{Eu}_x, \text{Li}_y]$ in which dopant ion concentrations have been systematically varied in order to define the

most emissive compositions under specific sets of x-ray excitation conditions. It is shown that these optimized $[Y_{2-x}O_3; Eu_x, Li_y]$ compositions display scintillation responses that: (i) correlate linearly with incident radiation exposure at x-ray energies spanning from 40 - 220 kVp, and (ii) manifest no evidence of scintillation intensity saturation at the highest evaluated radiation exposures [up to 4 Roentgen per second (R/s; 1 R = 2.58×10^{-4} Coulombs of charge produced by x- or γ -rays per kilogram of air)]. The most emissive of these nanoscale scintillator compositions is further exploited as a detector material in a prototype fiber-optic radiation sensor, and demonstrate its ability to provide a linear emission response as a function of radiation exposure for 80 and 225 kVp x-ray energies in a micro-CT dual imaging and high precision cone-beam therapy instrument utilized for small-animal image guided radiation therapy (IGRT).

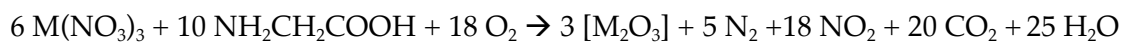
4.2 Experimental

Materials:

$Y(NO_3)_3 \cdot 6H_2O$ (99.99%), $Eu(NO_3)_3 \cdot 5H_2O$ (99.9%), $Li(NO_3)$ (99.99%), and glycine ($\geq 99\%$) were purchased from Sigma-Aldrich and used without further purification. HPLC-grade H_2O was also used (Fisher Chemicals).

Synthesis of $[Y_2O_3; Ln]$:

$[Y_2O_3; Eu_x]$, $[Y_2O_3; Eu_{0.1}, Li_y]$, and $[Y_2O_3; Li_y]$ compositions were synthesized by a solution combustion reaction involving glycine as the fuel. The reaction is as follows, where $M = Y, Eu, \text{ or } Li$;



The glycine-to-metal nitrate molar ratio was kept at 1.5:1 to ensure consistency of the samples. In a typical synthesis, 25 mL of HPLC grade H_2O was used to dissolve a total 0.2 mol/L of metal-nitrates and 0.3 mol/L of glycine in a 100 mL beaker. After stirring until dissolved fully, the stir-bar was removed and the reaction was placed on a

hot plate set to maximum heat until combustion occurred. The hot plate and reaction beaker were enclosed in a plexi-glass box in a hood to limit airborne materials when combustion occurs. After the reaction, the beaker was immediately removed and allowed to cool to room temperature. Powders in the beaker and the enclosure were collected in an aluminum oxide crucible and placed in a furnace at 500 °C for 1 hour to burn off any residual nitrates. The powders were then experimentally tested as is.

Instrumentation:

X-ray Diffraction (XRD) and Transmission Electron Microscopy (TEM) were performed at the Shared Materials Instrumentation Facility (SMiF) at Duke University. Inductively Coupled Plasma Atomic Emission Spectroscopy (ICP-AES) was performed by Kim Hutchison at NC State University.

X-ray Diffraction. Powder XRD was measured on a Philips X'Pert PRO MRD HR X-Ray Diffraction System from 5° - 75° (2 θ) under Cu K-Alpha (1.542 Å) irradiation at 45 keV and 40 mA.

Transmission Electron Microscopy. TEM was imaged on a FEI Tecnai G² Twin at a 200 keV accelerating voltage. Sample preparation consisted of making a 1 mg/mL solution of bare nanocrystals in ethanol, sonicating the solution for 1 minute in a bath sonicator, and then placing several drops of this solution on a carbon-formvar 400 mesh copper grid (EMS).

Raman Spectroscopy. The custom built Raman system utilized a PI Acton SP2360i 300 mm spectrograph outfitted with a PI Acton PIXIS 400 BR CCD detector. A Lasos 20 mW 633 nm He-Ne was utilized for sample excitation and its power density was controlled at 16 mW via a linear neutral density filter wheel. A Semrock RazorEdge Dichroic beam splitter and a Semrock Razor Edge long-pass laser blocking optics were

employed to direct the excitation light to the sample and filter the laser's Rayleigh scatter from the Raman signal in the collection path to the detector.

Solid-state X-ray Excited Scintillation (XES). XES spectra were measured on an Edinburgh Instruments FLSP920 equipped with a Hamamatsu R2658 PMT over a 500 – 700 nm wavelength range. A Faxitron RX-650 X-Ray Cabinet fiber coupled (Ocean Optics 400 μm) to the Edinburgh Instruments detection system allows for XES measurements with 130 kVp excitation power 130 kVp at a constant 5 mA. A X-Rad 320 X-Ray Cabinet fiber coupled (Ocean Optics 400 μm) to a Labsphere CDS2100 Spectrometer provided XES measurements at 40, 120, and 220 kVp (variable mA) over the range of 400 - 800 nm. For all measurements, 5 mg of $[\text{Y}_{2-x}\text{O}_3; \text{Eu}_x, \text{Li}_y]$ nanocrystals were pressed into a 7 mm diameter pellet using a Pike Technologies' hand press, placed on a Teflon mount in the x-ray cabinet, and the fiber was mounted right next to the pellet for light collection. Emission intensity was maximized by fiber placement before the acquisition occurred for each powder sample in the same geometry.

Fiber-Optic Device XES Response. The fiber-optic device was made by pressing 1 mg of the $[\text{Y}_{1.9}\text{O}_3; \text{Eu}_{0.1}, \text{Li}_{0.16}]$ material was into a 7 mm flat disk using the Pike Technologies' hand press to create a glass-like wafer. This wafer was then fractured into little pieces, where roughly a 400 μm diameter piece of this wafer was optically-glued (Norland 81) to one end of a 400 μm (inner diameter) unjacketed optical fiber (Ocean Optics). Once the glue was UV-cured, the nanocrystal-based wafer was cracked to cover just the 400 μm optical fiber entrance without any overhang. The other end of the fiber was connected to a Princeton Instruments SP2360i 300 mm spectrograph with a Princeton Instruments Pixis 400BR CCD camera. Light collection was made from 585 - 645 nm on a high groove-density grating, where only the dominant 611 nm peak was integrated from 605 - 617 nm.

Inductively Coupled Plasma Atomic Emission Spectroscopy (ICP-AES). ICP-AES measurements were made on a Perkin Elmer 2000 DV for Y, Eu, and Li ions in the as-synthesized samples. The data were compiled to compare the as-synthesized material to that anticipated based on reaction stoichiometry.

4.3 Results and Discussion

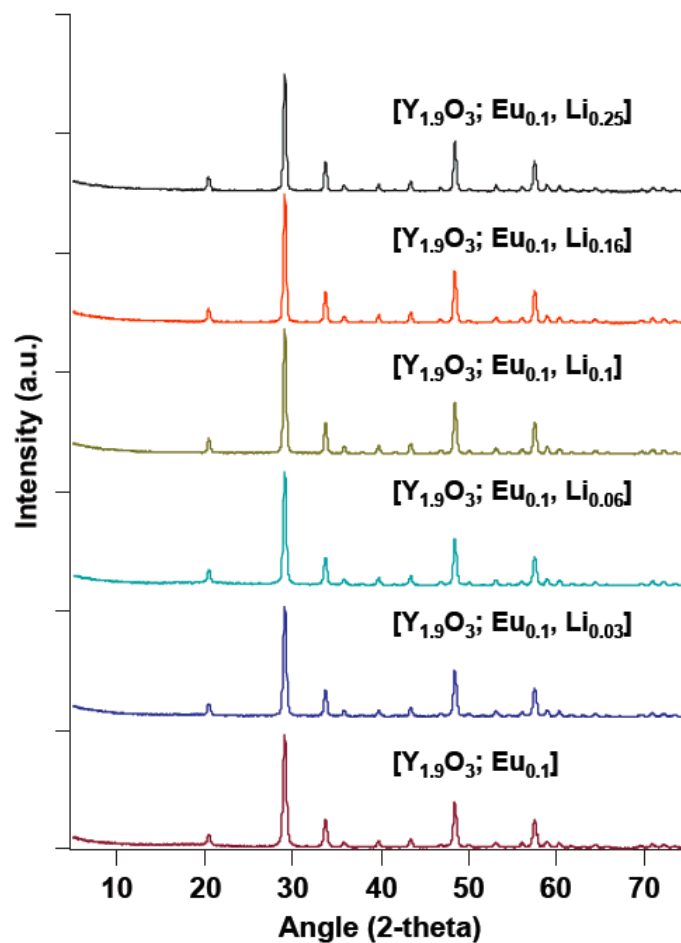


Figure 14: X-ray diffraction (XRD) spectra of the $[Y_{1.9}O_3; Eu_{0.1}, Li_y]$ compositions. All material compositions display the cubic phase, space group Ia3, JCPDS-88-1040.

Table 3: ICS-AES compositional analysis of the $[\text{Y}_2\text{O}_3; \text{Eu}_x]$, $[\text{Y}_2\text{O}_3; \text{Eu}_{0.1}, \text{Li}_y]$, and $[\text{Y}_2\text{O}_3; \text{Li}_y]$ samples, comparing the pre-combustion starting material predicted composition (theoretical) to the as-synthesized nanocrystal composition (actual). These data show that Eu ions are easily incorporated into the lattice with the anticipated stoichiometry; Li ion concentrations in the pre-combustion solution, however, exceed that found for the as-synthesized nanocrystals.

Theoretical	Actual
$[\text{Y}_2\text{O}_3]$	$[\text{Y}_2\text{O}_3]$
$[\text{Y}_{1.98}\text{O}_3; \text{Eu}_{0.02}]$	$[\text{Y}_{1.98}\text{O}_3; \text{Eu}_{0.02}]$
$[\text{Y}_{1.96}\text{O}_3; \text{Eu}_{0.04}]$	$[\text{Y}_{1.96}\text{O}_3; \text{Eu}_{0.04}]$
$[\text{Y}_{1.90}\text{O}_3; \text{Eu}_{0.1}]$	$[\text{Y}_{1.90}\text{O}_3; \text{Eu}_{0.1}]$
$[\text{Y}_{1.8}\text{O}_3; \text{Eu}_{0.2}]$	$[\text{Y}_{1.8}\text{O}_3; \text{Eu}_{0.2}]$
$[\text{Y}_{1.7}\text{O}_3; \text{Eu}_{0.3}]$	$[\text{Y}_{1.68}\text{O}_3; \text{Eu}_{0.32}]$
$[\text{Y}_{1.9}\text{O}_3; \text{Eu}_{0.1}]$	$[\text{Y}_{1.9}\text{O}_3; \text{Eu}_{0.1}]$
$[\text{Y}_{1.9}\text{O}_3; \text{Eu}_{0.1}, \text{Li}_{0.04}]$	$[\text{Y}_{1.9}\text{O}_3; \text{Eu}_{0.1}, \text{Li}_{0.03}]$
$[\text{Y}_{1.9}\text{O}_3; \text{Eu}_{0.1}, \text{Li}_{0.1}]$	$[\text{Y}_{1.9}\text{O}_3; \text{Eu}_{0.1}, \text{Li}_{0.06}]$
$[\text{Y}_{1.9}\text{O}_3; \text{Eu}_{0.1}, \text{Li}_{0.2}]$	$[\text{Y}_{1.9}\text{O}_3; \text{Eu}_{0.1}, \text{Li}_{0.1}]$
$[\text{Y}_{1.9}\text{O}_3; \text{Eu}_{0.1}, \text{Li}_{0.3}]$	$[\text{Y}_{1.9}\text{O}_3; \text{Eu}_{0.1}, \text{Li}_{0.16}]$
$[\text{Y}_{1.9}\text{O}_3; \text{Eu}_{0.1}, \text{Li}_{0.4}]$	$[\text{Y}_{1.9}\text{O}_3; \text{Eu}_{0.1}, \text{Li}_{0.25}]$
$[\text{Y}_2\text{O}_3; \text{Li}_{0.04}]$	$[\text{Y}_2\text{O}_3; \text{Li}_{0.03}]$
$[\text{Y}_2\text{O}_3; \text{Li}_{0.3}]$	$[\text{Y}_2\text{O}_3; \text{Li}_{0.18}]$

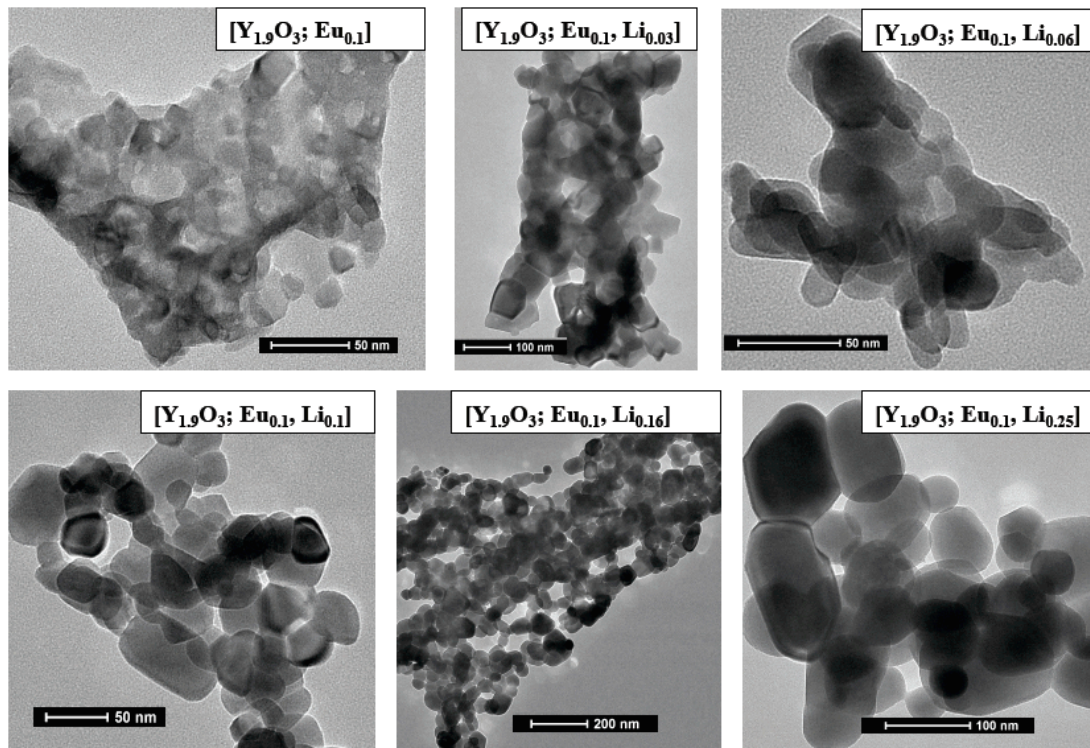


Figure 15: TEM images of $[\text{Y}_{1.9}\text{O}_3; \text{Eu}_{0.1}, \text{Li}_y]$ nanocrystals with increasing lithium-doping content. The amorphous content gradually disappears as Li ion concentration is increased; with these increasing Li^+ concentrations, isolated nanoparticles feature larger diameters as well as more well-defined crystalline boundaries.

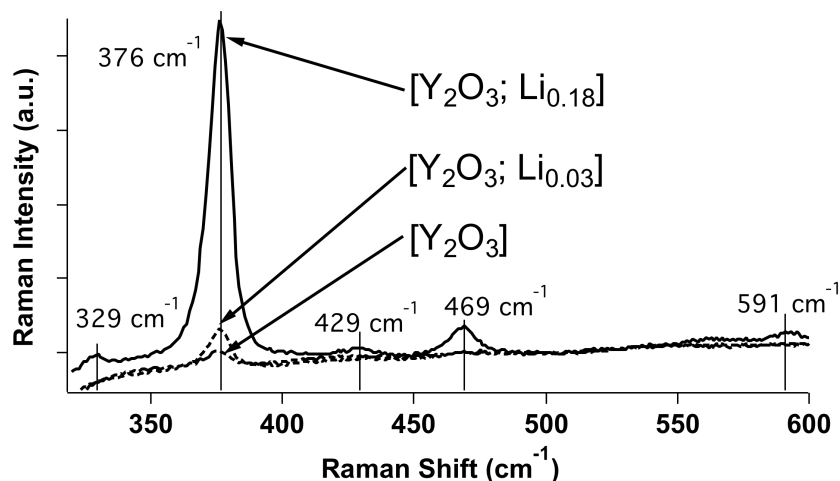


Figure 16: Raman spectra of $[Y_2O_3; Li_y]$ compositions acquired at a 632 nm irradiation wavelength. The increases in size and crystallinity observed in the TEM images as a function of increased Li concentration correlate with an observed increase in the Raman scattering intensity measured at 376 cm^{-1} .

The flame-combustion technique, utilizing glycine and metal nitrate salts at a fixed ratio, was employed to systematically synthesize nanocrystal compositions.^{68,96} X-ray diffraction (XRD) spectra confirmed that all compositions displayed a cubic structure, and inductively coupled plasma atomic emission spectroscopy (ICP-AES) provided $[Y_{2-x}O_3; Eu_x, Li_y]$ compositional analysis (**Figure 14; Table 3**, respectively). **Figure 15** displays representative TEM images for the $[Y_{1.9}O_3; Eu_{0.1}, Li_y]$ compositional series ($y = 0$ to 0.25), that reveal that as Li doping is increased from $y = 0$ to $y = 0.25$, crystalline size increases from $\sim 20 - 40\text{ nm}$ to $\sim 50 - 90\text{ nm}$, and crystalline boundaries become better defined. Increased nanocrystal sizes and the corresponding reduction of amorphous content are evident in TEM images and the Raman spectra of these samples; note that as the Li ion doping concentration increases, the Raman scattering intensity of the dominant optical phonon of cubic- Y_2O_3 at 376 cm^{-1} increases (**Figure 16**), congruent with data acquired for corresponding heterogeneous bulk-phase samples.⁹⁷ While increased levels of Li ion doping of bulk phase $[Y_2O_3; Eu]$ compositions have been demonstrated to track qualitatively with augmented cathodoluminescence intensity,^{75,76}

the experimental data presented herein highlight that the increased nanoscale size and crystallinity of the Y_2O_3 host lattice that occurs with Li^+ doping also results in an increased scintillation intensity of the nanocrystalline $[\text{Y}_{2-x}\text{O}_3; \text{Eu}_x, \text{Li}_y]$ compositions (*vide infra*).

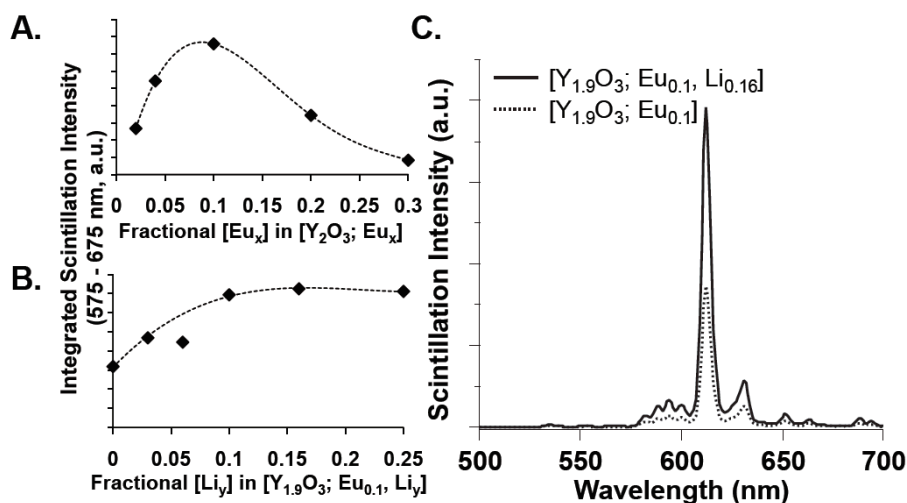


Figure 17: Integrated, solid-state x-ray emission spectral intensities determined over a 575 - 675 nm range for: (A) $[\text{Y}_2\text{O}_3; \text{Eu}_x]$ and (B) $[\text{Y}_{1.9}\text{O}_3; \text{Eu}_{0.1}, \text{Li}_y]$ compositions (note: trend lines added for visualization purposes). (C) The x-ray emission spectra of the most emissive Eu and Eu/Li co-doped samples, recorded for 130 kVp (5 mA) x-ray excitation.

To obtain $[\text{Y}_{2-x}\text{O}_3; \text{Eu}_x, \text{Li}_y]$ compositions that display enhanced emission, Eu concentrations were initially varied over a $[\text{Y}_{1.98}\text{O}_3; \text{Eu}_{0.02}]$ to $[\text{Y}_{1.69}\text{O}_3; \text{Eu}_{0.31}]$ compositional range, and interrogated via solid-state x-ray emission spectroscopy (XES) using a 130 kVp (5 mA) x-ray cabinet-confined irradiation source. In these studies, 5 mg of $[\text{Y}_{2-x}\text{O}_3; \text{Eu}_x]$ nanocrystals were pressed into a 7 mm diameter disk and placed on a Teflon mount; an optical fiber was utilized to collect scintillated emission, which was quantitated using an Edinburgh FLS920 spectrometer. These studies demonstrated that the $[\text{Y}_{1.9}\text{O}_3; \text{Eu}_{0.1}]$ composition was the most emissive member of this compositional

series; **Figure 17A** displays the x-ray emission intensities determined over a 575 - 675 nm range for these nanoscale $[\text{Y}_2\text{O}_3; \text{Eu}_x]$ compositions. Note that this experimental trend in x-ray emission intensity determined as a function of Eu ion concentration depicts characteristic activator ion emission behavior in yttrium oxide host crystals,^{38,77,98,99} *i.e.*, an optimal concentration of emitting ions exists, beyond which cross-ion quenching drives reductions of emission intensity.

Holding the optimized Eu activator ion concentration of $[\text{Y}_{1.9}\text{O}_3; \text{Eu}_{0.1}]$ constant, progressively increasing Li ion concentrations were incorporated into combustion reactions used to synthesize the $[\text{Y}_{1.9}\text{O}_3; \text{Eu}_{0.1}, \text{Li}_y]$ compositions; ICS-AES was used to determine the ion doping levels of the isolated nanocrystalline products (**Table 3**).

Figure 17B shows the integrated solid-state x-ray emission intensities determined over a 575 - 675 nm range for $[\text{Y}_{1.9}\text{O}_3; \text{Eu}_{0.1}, \text{Li}_y]$ ($y = 0$ to 0.25) compositions recorded for 130 kVp (5 mA) x-ray excitation. These XES data show that $[\text{Y}_{1.9}\text{O}_3; \text{Eu}_{0.1}, \text{Li}_{0.16}]$ is the most emissive of the $[\text{Y}_{1.9}\text{O}_3; \text{Eu}_{0.1}, \text{Li}_y]$ compositions under these conditions, displaying more than twice the emission intensity of the parent $[\text{Y}_{1.9}\text{O}_3; \text{Eu}_{0.1}]$ nanocrystalline material (**Figure 17C**).

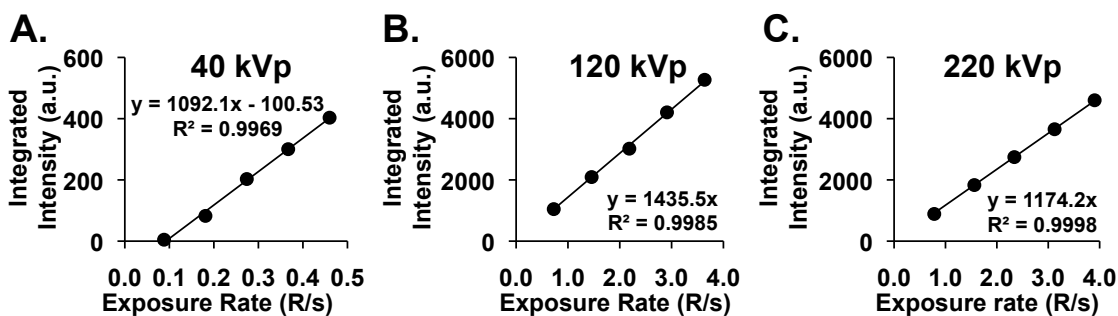


Figure 18: Integrated solid-state x-ray emission spectral intensity recorded over the 500 - 700 nm range as a function of radiation exposure (R/s) for: (A) 40, (B) 120, and (C) 220 kVp excitation.

Energy and flux dependent x-ray emission spectroscopic measurements of the most emissive nanoscale composition, $[Y_{1.9}O_3; Eu_{0.1}, Li_{0.16}]$, were determined for solid-state samples at 40, 120, and 220 kVp excitation through modulation of the x-ray tube current (mA). For a given x-ray tube voltage, the tube current was adjusted in 2-5 mA steps to provide a range of x-ray exposure rates (R/s). **Figure 18A-C** shows the linear response of the integrated emission intensity over the 500 - 700 nm emission range recorded for 40, 120, and 220 kVp x-ray excitation energies, respectively. For 120 and 220 kVp excitation, integrated scintillation intensities were recorded over identical exposure-rate ranges (0.6 - 4.0 R/s) in order to assess the energy dependence of the scintillation intensity. Note that the dependences of scintillation intensity upon radiation dose differ slightly at these two excitation energies (**Figure 18B-C**), as the slope determined at 120 kVp surpasses that at 220 kVp by a factor of 1.2. As both of these x-ray excitation energies exceed that of the yttrium k-edge (17 keV), this effect is congruent with the facts that (i) yttrium-oxide displays a higher mass-attenuation coefficient (ionizing radiation absorption) at 120 kVp than 220 kVp,¹⁰⁰ and (ii) the scintillation mechanism is dominated by the photoelectric effect at 120 kVp, and the Compton effect at 220 kVp, for yttrium's Z-number of 39.¹⁰¹ These data further underscore that the scintillation quantum yield for the nanoscale $[Y_{1.9}O_3; Eu_{0.1}, Li_{0.16}]$ composition for photoelectric energy region absorption exceeds that for Compton energy region absorption, for comparable high-energy photon exposures and this nanocrystalline lattice.

The spectroscopically demonstrated linear response of scintillation intensity with x-ray energy and flux for these nanocrystals, across broad, medically relevant energy and exposure ranges (**Figure 18**), can be exploited in device applications. As such, a prototype device for measuring radiation exposure (dosimetry), based on these nanomaterials, was developed. $[Y_{1.9}O_3; Eu_{0.1}, Li_{0.16}]$ nanocrystals (1 mg) were pressed into

a 7 mm flat disk; a fractured piece of ~400 μm diameter (~3.3 μg) was employed as the device detection element, and optically-glued to one end of a 400 μm (inner diameter) optical fiber. The other end of the fiber was connected to a high-sensitivity, high-spectral resolution CCD-spectrometer (**Figure 19A**). The integration times of the CCD-camera were varied from 0.5 to 20 seconds at 80 and 225 kVp x-ray energies to record the total radiation exposure up to 6.4 Roentgen at 80 kVp and 117.8 Roentgen at 225 kVp. The scintillation intensity from the $[\text{Y}_{1.9}\text{O}_3; \text{Eu}_{0.1}, \text{Li}_{0.16}]$ -modified optical fiber tip, integrated over the 605 - 617 nm wavelength domain (note that this integration range is limited by the CCD-spectrometer spectral window), was correlated with radiation exposure using a Precision XRAD 225Cx small-animal image guided radiation therapy (IGRT) system, in order to highlight the relevance of this prototype device to *in vivo* radiation dosimetry. The Precision XRAD 225Cx instrument employs low dose x-ray computed tomography (CT) to image a specific organ or tissue area of interest, prior to delivery of therapeutic x-ray doses via an x-ray pencil-beam that targets millimeter-sized areas of malignant tissue at high precision, thus minimizing healthy tissue damage.¹⁰²

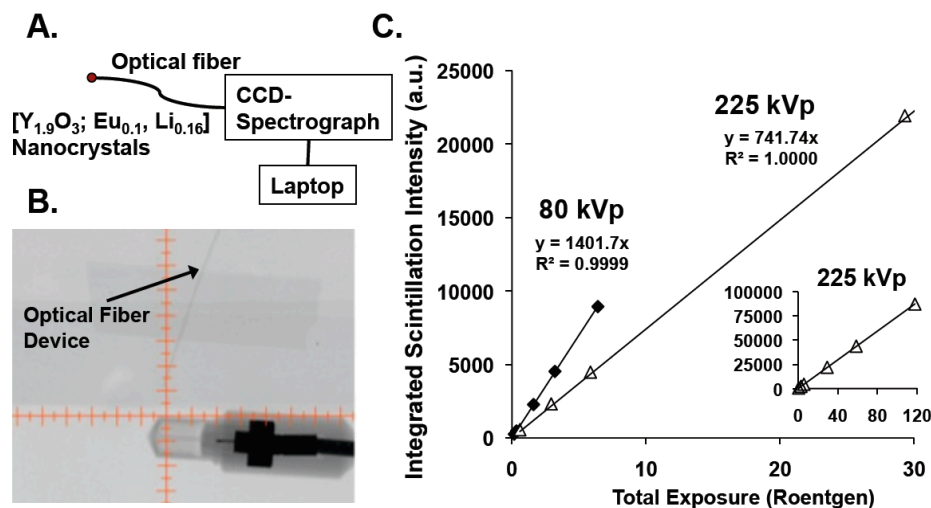


Figure 19: (A) A schematic of the sub-mm-sized optical fiber prototype dosimeter based on nanoscale $[Y_{1.9}O_3; Eu_{0.1}, Li_{0.16}]$. (B) An x-ray CT image acquired at 40 kVp, showing the optical fiber device adjacent to an ion-chamber radiation detector. (C) The linear scintillation intensity recorded by the device integrated over 605 - 617 nm that measures the total dose deposited at 80 kVp (imaging) and 225 kVp (therapy) energies. The CT image was acquired in a Precision XRAD 225Cx small-animal image guided radiation therapy (IGRT) system; the scintillation data were recorded using IGRT 80 and 225 kVp excitation. Note that all data points were measured in triplicate, and the standard deviation for a given data point was $< 0.9\%$. The inset of (C) shows that the device scintillation response tracks linearly with exposure to the highest levels tested (117.8 Roentgen at 225 kVp).

Figure 19B shows a x-ray image taken at 40 kVp of the fiber-optic device next to a standard ion-chamber radiation detector used to calibrate the radiation exposure on the Precision XRAD 225Cx image guided radiation therapy (IGRT) system. Note that the copper wires present in the ion-chamber show dark contrast, highlighting that the sensor portion of the prototype detector based on nanoscale $[Y_{1.9}O_3; Eu_{0.1}, Li_{0.16}]$ is effectively radiotransparent during diagnostic imaging, due to the low-density, low Z-number, and small size of the fiber-optic. This radio transparency of the fiber-optic device underscores its *in vivo* utility with the IGRT system as it alternately provides accurate dosimetry measurements for both diagnostic imaging and radiation therapy

treatment, while precluding the possibility for significant imaging artifacts that accompany the use of ion chamber- or MOSFET-based dosimeters.

Figure 19C displays a plot of integrated scintillation intensity (605 - 617 nm) versus total radiation exposure at both 80 kVp (diagnostic imaging) and 225 kVp (therapy) energies. As noted earlier for data that compared emission intensity for 120 and 220 kVp excitations at equivalent exposures (**Figure 18B-C**), 80 kVp incident x-rays produce more light than 225 kVp x-rays over identical 0 - 6 Roentgen exposure ranges. Critical to the envisioned applications for this device, note that the scintillation response tracks linearly with exposure (at least to 117.8 Roentgen at 225 kVp). Moreover, since the entire scintillation spectrum, not just a single scintillation wavelength, expresses a linear response with respect to radiation exposure (**Figure 18A-C**), simple device architectures that exploit Si-photodiodes can be fabricated: as Si-photodiodes manifest maximal sensitivity over the emission range of nanoscale $[\text{Y}_{1.9}\text{O}_3; \text{Eu}_{0.1}, \text{Li}_{0.16}]$, the timing speeds, sizes, and low power-consumption of these devices, coupled with the detection element's linear dependence of scintillation intensity with radiation dose, demonstrates the opportunity for next-generation radiation exposure measuring devices for *in/ex vivo* applications that are ultra-small, inexpensive, and accurate. Note that such devices that exploit rare-earth doped inorganic nanocrystals will compliment pioneering optical fiber dosimeters that are based on plastic scintillating materials,¹⁰³⁻¹⁰⁵ while providing superior environmental and radiation stability, new scintillation energy ranges, and the opportunity for significantly red-shifted luminescence.

4.4 Conclusion

In summary, Eu- and Li-doped yttrium oxide nanocrystals $[\text{Y}_{2-x}\text{O}_3; \text{Eu}_x, \text{Li}_y]$ in which Eu and Li dopant ion concentrations were systematically varied, were developed and characterized (TEM, XRD, Raman spectroscopic, and ICP-AES data) in order to

define the most emissive compositions under specific x-ray excitation conditions. These optimized $[Y_{2-x}O_3; Eu_x, Li_y]$ compositions display scintillation responses that: (i) correlate linearly with incident radiation exposure at x-ray energies spanning from 40 - 220 kVp, and (ii) manifest no evidence of scintillation intensity saturation at the highest evaluated radiation exposures [up to 4 Roentgen per second]. For the most emissive nanoscale scintillator composition, $[Y_{1.9}O_3; Eu_{0.1}, Li_{0.16}]$, excitation energies of 40, 120, and 220 kVp were chosen to probe the dependence of the integrated emission intensity upon x-ray exposure-rate in energy regimes where either the photoelectric or the Compton effect governs the scintillation mechanism; these experiments demonstrate for nanoscale $[Y_{2-x}O_3; Eu_x]$, that for comparable radiation exposures, when scintillation is governed by the photoelectric effect (120 kVp excitation), greater integrated emission intensities are recorded relative to excitation energies where the Compton effect regulates scintillation (220 kVp excitation). Nanoscale $[Y_{1.9}O_3; Eu_{0.1}, Li_{0.16}]$ (70 ± 20 nm) was further exploited as a detector material in a prototype fiber-optic radiation sensor. The scintillation intensity from a $[Y_{1.9}O_3; Eu_{0.1}, Li_{0.16}]$ -modified, 400 μ m-sized optical fiber tip, recorded using a CCD-photodetector and integrated over the 605 - 617 nm wavelength domain, was correlated with radiation exposure using a Precision XRAD 225Cx small-animal image guided radiation therapy (IGRT) system. For both 80 and 225 kVp energies, this radiotransparent device recorded scintillation intensities that tracked linearly with total radiation exposure, highlighting its capability to provide alternately accurate dosimetry measurements for both diagnostic imaging (80 kVp) and radiation therapy treatment (225 kVp). Because Si-based CCD and photodiode detectors manifest maximal sensitivities over the emission range of nanoscale $[Y_{1.9}O_3; Eu_{0.1}, Li_{0.16}]$, the timing speeds, sizes, and low power-consumption of these devices, coupled with the detection element's linear dependence of scintillation intensity with radiation dose, demonstrates

the opportunity for next-generation radiation exposure measuring devices for *in/ex vivo* applications that are ultra-small, inexpensive, and accurate.

Acknowledgement. I would like to thank Matthew D. Belley, Giao Nguyen, Anna Rodrigues, Yifan Li, David G. Kirsch, Terry T. Yoshizumi, and Michael J. Therien for their contributions to this work, as well as financial support in part by grants from the Department of Homeland Security, Domestic Nuclear Detection Office - Academic Research Initiative (NSF-ECCS-11-40037), the National Aeronautics and Space Administration (NNX11AC60G), the U.S. NRC Health Physics Fellowship (NRC-HQ-12-G-38-0022), and the National Institute of Allergy and Infectious Diseases (5U19AI067798).

5. Characterization of a Nano-Scintillator Terminated Fiber-Optic Dosimeter for *in vivo* Diagnostic and Radiation Therapy Dosimetry

Accurate, cost effective, and real-time *in vivo* patient dosimetry during radiation therapy (RT), diagnostic, and interventional x-ray procedures provides an invaluable tool for monitoring organ doses, assessing patient safety, and improving clinical outcomes. Ideal clinical dosimeters should have the following properties by providing: (i) simplicity in operation, (ii) cost-effectiveness, (iii) real-time reading, (iv) negligible performance degradation in normal hospital environment, and (v) minimum radiation damages during its lifetime. In addition, the detector may add additional values by providing: (i) negligible image artifact, (ii) small size point dosimetry, and (iii) easy integration in clinical environment. Herein, a nano-scintillator terminated fiber-optic based dosimeter (NS-FOD) is proposed to be a viable candidate to meet all of the aforementioned properties, and is shown to provide accurate dosimetry in tissue phantoms under clinical x-ray CT energies. In addition, it may offer a superior choice when compared to existing detectors such as metal oxide semiconductor field effect transistors (MOSFETs), thermoluminescent dosimeters (TLDs), and ion-chambers (ICs) for broad use in instrument characterization, validation, and calibration, as well as for patient radiation dose monitoring, given its size, durability, cost, and most importantly, accuracy and reproducibility.

5.1 Introduction

While some current commercial dosimetry detectors, specifically the gold-standard ion chamber (IC), can provide attributes such as simplicity in operation and radiation longevity, all commercial dosimeters currently fall short on sizes appropriate for *in vivo* monitoring, simplicity of use and handling in clinical settings, cost-effectiveness that would allow them to be broadly employed, and most importantly the ability to measure dosimetry in real-time. This is especially imperative given that accurate, cost effective, and real-time *in vivo* patient dosimetry during radiation therapy (RT), diagnostic, and interventional x-ray procedures can provide an invaluable tool for monitoring organ doses, assessing patient safety, and improving clinical outcomes.

MOSFETs are relatively small and durable dosimeters that provide an easy way to measure point doses near real-time.⁴⁸ However, there are several factors that would limit their use for *in vivo* therapy and diagnostic applications. One foremost limitation of MOSFETs is their finite lifetime of use due to radiation damage; MOSFETs record dose on a radiation-to-charge generated (mV) scale, with a total lifetime of about 16,000-20,000 mV (16-20 Gy).⁴⁹ Radiation aging of MOSFET detectors has been reported previously and the re-calibration of the detectors has been suggested for both diagnostic and therapy MOSFETs.^{50,51} In addition, MOSFETs have angular response dependencies due to the geometry of the sensitive detector area,⁵² which limits their use for rotational radiation fields such as axial and helical scans in CT. Another imperfection of MOSFETs is that they are *integrating detectors*, where subtracting the final voltage from the initial voltage reading of each individual experiment is used to determine the absorbed dose. Thus, MOSFETs cannot obtain dose-rate responses in *real-time*, nor can they measure dose fluctuations in real-time during the experiment integration, an attribute highly desired for pin-point *in vivo* dosimetry and radiation surveillance

applications. Finally, MOSFETs and the required signal wires are not radio-opaque; they are comprised of high Z materials of metal-oxide sensors and copper wires, and thus they can obstruct underlying structures on radiographic images,⁵³ or scatter radiation from arriving to its target point.

TLDs have seen widespread use for dosimetry due to their accuracy and ease of re-use, but are often not chosen as the primary method of measurement due to several drawbacks. The first of which, is that TLDs require a time consuming annealing process prior to exposure (for a TLD-100, annealing takes at least 3 hours), and like MOSFETs, they are an integrating detector, not allowing for real-time dose rates. Another consequence of this integration happens during transportation and storage, as TLDs must be shielded from UV and visible light to minimize false readings.⁵⁴ The recommended stabilization time of 24 hours post-irradiation prior to reading further limits their usefulness as a fast read-out detector, particularly considering the additional instrumentation needed to quantify the dose.⁵⁵ This point furthers the consideration of using TLD dosimetry versus other methods, as it can be very expensive and time consuming, especially when one considers the cost of the TLD reader, nitrogen gas system, TLD annealing equipment, and manpower. Lastly, TLDs are delicate and require careful handling with vacuum tweezers since dust, dirt, and scratches can introduce errors in the measured dose values.

When compared to MOSFETs and TLDs, the nano-scintillator terminated fiber-optic based dosimeter (NS-FOD) is superior due to the following: the NS-FOD can be fabricated sub-millimeter in size with lengths on the order of meters (MOSFET lead wire is less than 40 cm in length), the NS-FOD has displayed no radiation damage to date, has no fabrication limited angular dependent response, displays very little if any contrast during imaging due to the low Z fiber, only requires a single calibration at each energy

range to be used, has no special handling requirements, and it is able to provide real-time dose-rate measurements. Additionally, at over an order of magnitude less costly than a complete MOSFET reader system and detectors or TLD detectors and associated hardware, the NS-FOD device could revolutionize the ultra-small, portable, and reliable dose measurement market.

The IC performs near real-time (0.2 - 0.5 Hz) and integrated dose measurements, can detect a broad spectrum of incident x-ray and gamma-ray energies, and offers superior durability, making it the gold-standard for dosimetry. Unfortunately, it is not feasible to use an IC for many of the *in vivo* applications in the clinic, nor for organ dose measurements in the phantom due to the relatively large size of ICs being a centimeter or greater in diameter. In contrast, the NS-FOD is better suited for *in vivo* applications, due especially to its small size and relatively low Z value of the optical fiber that leads to virtually no contrast during x-ray imaging, and no radiation scattering during radiation therapy.

Fiber-optic based radiation detectors have been of recent interest, with several design and fabrication routes to achieve ultra-small size, radiation and handling durability, as well as sensitivity. The most common of these is made by attaching a plastic scintillator at the end of an optical fiber,⁵⁶⁻⁵⁸ or by encasing a plastic scintillator with a non-scintillating cladding at the end of an optical fiber, some of which are commercialized by companies like Saint-Gobain (Paris, France) and Kuraray (Tokyo, Japan). A very detailed literature example with comparative results highlights how plastic fiber length, fiber diameter, and fiber scintillator type perform, with results showing that the plastic scintillator with a non-scintillating cladding produces more light than simply attaching a plastic scintillator at the end of the tip, both using a PMT for the photodetector.⁵⁶ By using the latter plastic scintillator at the end of an optical fiber

with a electron multiplying charge coupled device (EMCCD) camera, the same authors were able to accurately demonstrate dose measurements in an anthropomorphic prostate phantom in real-time,⁵⁷ which provides foundational capabilities for ultra-small radiation detectors. However, the use of EMCCD cameras in the field is impractical, due to their incredibly high cost, high noise with high gain acquisition, and additional size, power and mounting requirements, to name a few. In comparison, the Si-photodiode light meter used in the NS-FOD device data presented herein is roughly 400 times less expensive than an EMCCD, is not much bigger than a common smart-phone, and runs off USB power. Furthermore, the use of inorganic materials provides much longer radiation stability and ease of fabrication and handling, and since such a small quantity is directly mounted to the tip of the fiber with an estimated 50 micron thickness, no extra cladding is needed to direct light into the fiber. Another recent literature example utilizes CsI nanocrystals imbedded into a porous optical fiber, which is then connected to a conventional optical fiber using a quartz capillary, whose signal is read by a PMT photodetector.¹⁰⁶ While this approach and material might be advantageous for photon-counting applications, its use for medically relevant dosimetry again lacks portability, is costly, and requires additional time for fabrication relative to the NS-FOD device presented herein. Moreover, the environmental stability of CsI renders the material and device fabrication to be handled with much more care.

Presented herein is the demonstration of a dosimetry device utilizing nano-scintillator inorganic crystals as the sensor, a sub-millimeter fiber-optic signal transfer wire, and a USB powered Si-photodiode light power meter to record accurate dose measurements in and on tissue phantoms in direct comparison to ICs in strong accord.

5.2 Experimental

Fabrication of the nano-scintillator terminated fiber-optic dosimeter:

A previously optimized nano-scintillator composition, cubic-[Y_{1.9}O₃; Eu_{0.1}, Li_{0.16}] (Chapter 4), was utilized as the radiation sensing material. The fiber-optic device was made by pressing 1 mg of the [Y_{1.9}O₃; Eu_{0.1}, Li_{0.16}] material was into a 7 mm flat disk using the Pike Technologies' hand press to create a glass-like wafer. This wafer was then fractured into little pieces, where roughly a 600 µm diameter piece of this wafer was optically-glued (Norland 81) to one end of a 600 µm (inner diameter) unjacketed optical fiber (Ocean Optics). Once the glue was UV-cured, the nanocrystal-based wafer was cracked to cover just the 600 µm optical fiber entrance without any overhang. The other end is used to couple to a calibrated photodiode meter with a SMA-905 connector. The calibrated Si-photodiode light meter (Thor Labs, SM150C and PM100USB) is USB powered from a laptop to ensure portability. For the Xrad320 measurements, the sensor was set to record light power by averaging 250 points per 0.1 seconds at a wavelength calibration of 611 nm. For the GE-VCT measurements, the sensor was set to record light power by averaging 150 data point per 0.05 seconds at a calibration wavelength of 611 nm, as dose delivery times were much shorter during the CT trials. Each of the two systems used a different nano-scintillator terminated fiber, but used the same photodiode sensor.

Data Analysis Program:

The raw data files as acquired from the Thor Labs light meter were processed using in-house software that was developed using Python Software Foundation. The raw data was processed by automatically detecting the peak values corresponding to the light output (in Watts) of the sensor during irradiation and integrating the signal during

the exposure (to obtain Joules). The raw data was then used to calculate the background and noise. This noise was then subtracted from the integrated signal data to obtain the net signal due to radiation and thus negate the effects of dark noise on the Si-photodiode.

Tissue Equivalent Phantoms:

Three phantoms were used in this study to determine the detector response in tissue-equivalent materials. These were (a) a custom tissue equivalent slab of dimension 150 mm x 150 mm x 25 mm, (b) an ATOM anthropomorphic breast phantom, and (c) an ATOM adult male anthropomorphic phantom, all manufactured by CIRS (Norfolk, VA). In phantom (a), two through holes were drilled in the block to allow for side-by-side placement, one for the MOSFET and NS-FOD, and the other for the ion-chamber, both of which were located approximately in the center of the block and at the same depth. For phantom (b), the breast size was 300 cc and had 5mm diameter holes for side-by-side insertion of the MOSFET and NS-FOD, and was comprised of a material that simulated 50% glandular and 50% adipose tissue (BR50/50). For phantom (c), the NS-FOD and the ion-chamber were placed on the sternum of the whole body phantom, parallel and perpendicular to the patient bed, perpendicular to the x-ray tube axis for comparison.

Comparison Dosimeters:

The MOSFETs and mobile MOSFET Dose Verification System (TN-RD-70-W) used in this study were manufactured by Best Medical Canada (Ottawa, Ontario). A set of 5 MOSFETs (TN-502RD) were calibrated against the IC free in air. The average calibration factor from 3 individual exposures of ~5.3R was used. The MOSFET with the lowest uncertainty reading was used as the sole detector for the breast phantom dose. A

0.18cc IC (model 10X6-0.18, Radcal, Monrovia, CA) and a monitor (model 9015, Radcal, Monrovia, CA) were used for the MOSFET calibration. A detailed description of a MOSFET calibration method can be found elsewhere.^{48,107} The IC was calibrated at the AAPM accredited calibration laboratory (University of Wisconsin).

Small Animal Orthovoltage Irradiator and MDCT Scanner:

The Xrad-320 x-ray irradiator (Precision X-ray, North Branford, CT) with a model F4 filter (0.1mm Cu and 2.5mm Al, Precision X-ray) was used to calibrate MOSFET detectors. The filter F4 provided the equivalent beam quality (~7.51 mm Al HVL) to the GE-VCT scanners at 120 kVp. A General Electric MDCT scanner was used for the adult male anthropomorphic phantom data (model Lightspeed VCT, GE Healthcare, Milwaukee, WI).

Nano-scintillator Terminated Fiber-Optic Dosimeter (NS-FOD) Calibration:

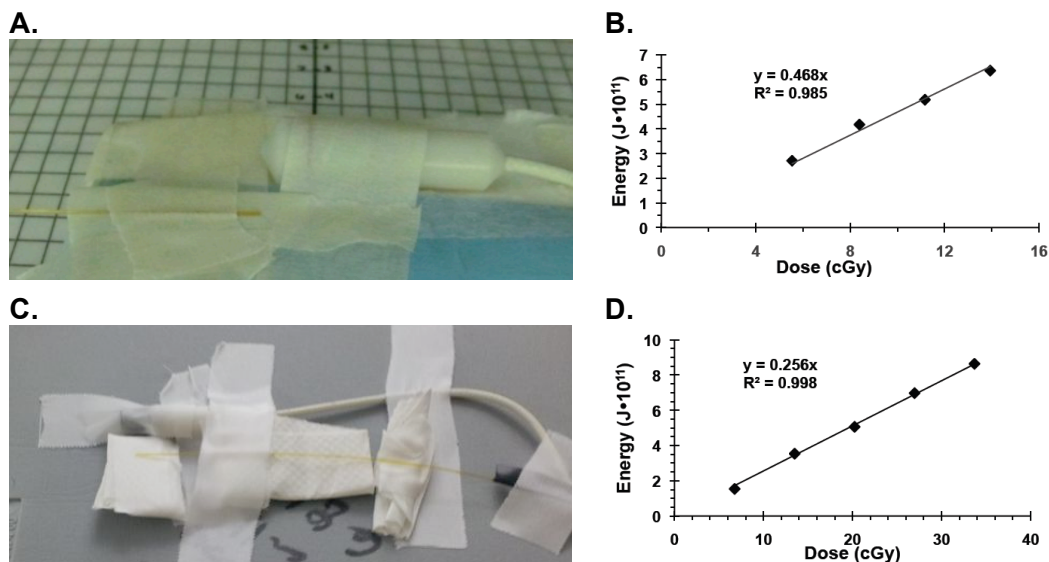


Figure 20: (A) A picture of the NS-FOD in front of the ion-chamber and (B) the calibration curve during Xrad320 calibration, and (C) a picture of the NS-FOD next to the ion-chamber and (D) the calibration curve during GE-VCT calibration. Both calibrations display a high level of linearity over the broad dose range that each x-ray machine is capable of producing.

A calibration curve was obtained by plotting the NS-FOD light response versus IC measured dose to tissue as measured free-in air prior to tissue phantom studies. During this measurement, the IC and the NS-FOD dosimeters were placed approximately 1 cm apart under the x-ray beams on a piece of Styrofoam, with the fiber tip being placed directly in the center of the much larger ion-chamber. For the Xrad320 measurements, the ion-chamber was set to record dose rate once the beam stabilized, as the beam could be operated at much longer time scales (16.4 sec) for the NS-FOD calibration. For the GE-VCT experiment, the ion-chamber was set to record total dose for the NS-FOD calibration due to the much shorter calibration and measurement times of 3 sec and 1 sec, respectively, and x-ray tube rise and fall times. This difference in calibration methods further proves that the NS-FOD can be calibrated using either

process to achieve a standardization curve for subsequent dose measurements, providing real-time and integrated dose measurements from the same data set. **Figure 20A,C** show a picture of the NS-FOD and ion-chamber positioning during calibration in the Xrad-320 and GE-VCT, respectively. **Figure 20B,D** display the acquired linear calibration curves and its slope for subsequent light-to-dose conversions in the Xrad-320 and GE-VCT, respectively, of the two nano-scintillator terminated fibers used. The difference in their slope is reflective of the variation in fabrication, as quantities of material and fiber length were different for each case. The R-squared values of both device calibrations, 0.985 for the Xrad-320 and 0.998 for the GE-VCT, reflect a near perfect linearity, establishing the ability for this device to function across a broad range of incident dose rates at this highly used medically relevant x-ray voltage. It is worthwhile to note that device calibration is dependent on fiber-size, fiber-length and the amount and type of material used, while it is also dependent on the energy range of the incident radiation. However, once a single NS-FOD cable is calibrated at desired energy ranges, the curve parameters can be used for any sensitive power meter that is calibrated for light response.

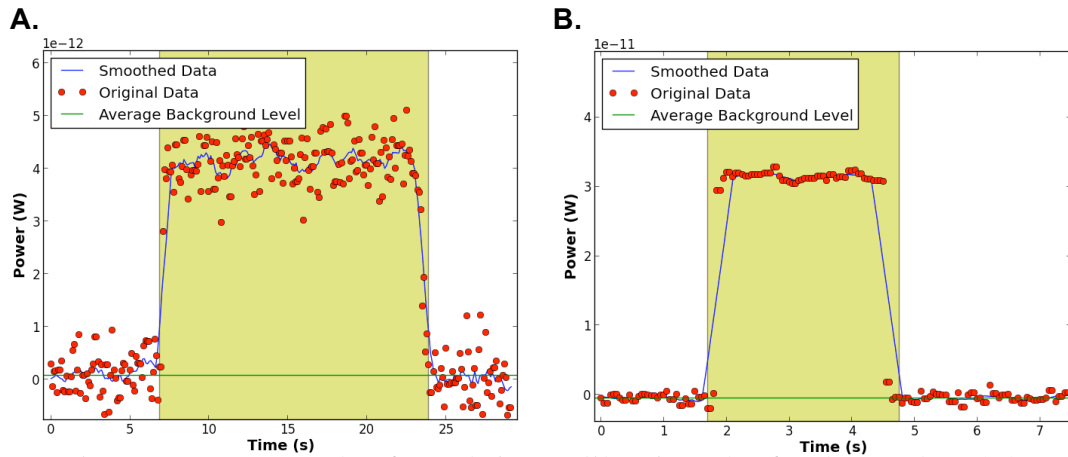


Figure 21: An example of a real-time calibration plot for the Xrad320 (A) and GE-VCT (B), from which a linear slope of the intensities can be correlated to a dose.

Figure 21A shows a real-time acquired calibration trial in light power (Watts) for a dose rate of 0.85 cGy/s on the Xrad320, while **Figure 21B** shows a calibration trial for the GE-VCT with a total dose delivered of 33.7 cGy, both values as recorded by an ion-chamber for the calibration. Comparing these two specific examples, the original data counts clearly show GE-VCT delivered a much higher dose rate, exhibited by the near order of magnitude increase in scintillation power and increased signal-to-noise ratio. Once the plots of calibration are made (**Figure 20B,D**), the y-axis can be directly converted to dose for real-time dose-rate monitoring.

5.3 Results

Measurement comparison of the NS-FOD, MOSFET, and IC in a tissue block in the orthovoltage x-ray machine

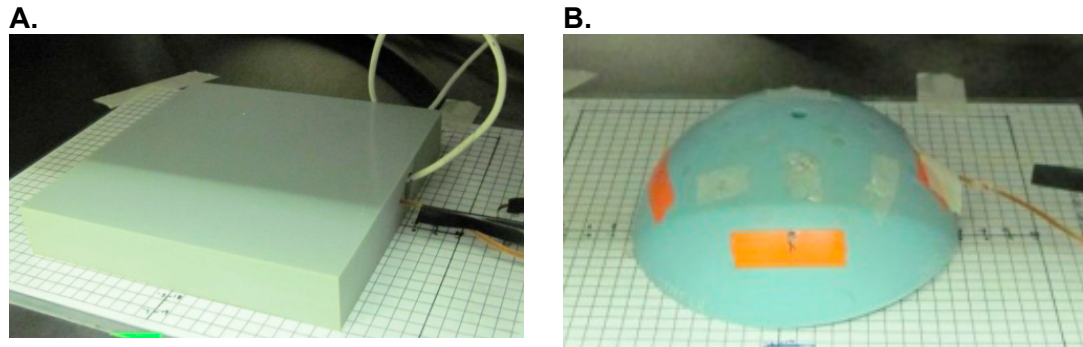


Figure 22: The 150 mm x 150 mm x 25 mm tissue equivalent block with the ion-chamber, MOSFET, and NS-FOD inserted at the same relative depth, and (B) the 300 cc breast phantom with the MOSFET and NS-FOD inserted at the same location.

Table 4: Dose measurements and statistics from the tissue equivalent block phantom.

Trial	Dose (cGy)		
	Ion-Chamber	NS-FOD	MOSFET
1	9.87	10.26	11.54
2	9.88	10.40	10.84
3	9.88	9.24	10.73
4	9.9	9.87	10.94
Mean	9.88	9.94	11.01
RSD*	0.1%	5.2%	3.3%
<i>% Difference to Ion-Chamber</i>		0.6%	11.4%
<i>T-TEST to Ion-Chamber</i>		0.84	0.01
*Relative Standard Deviation			

A 150 mm x 150 mm x 25 mm tissue equivalent block was used to evaluate all three dosimetry devices simultaneously, in the geometry described above (**Figure 22A**). Four measurements were made at 120 kVp and 15 mA for 18 seconds, with an ion-chamber average reported dose of 9.88 cGy. **Table 4** shows the individual measurement comparisons between the IC, NS-FOD, and MOSFET devices in the tissue block, along

with their relative differences to the IC, and a calculated two-tailed t-test to determine if the mean values were statistically different from one another. For the two-tailed t-test, a null hypothesis was that there was no difference in the mean with a p-value of 0.025, designating a 95% confidence interval for higher or lower mean deviations. Therefore, if the value from the t-test was above 0.025, the null hypothesis could not be rejected and that the mean values were statistically equivalent with 95% confidence. The relative standard deviation (RSD) of each device was further calculated, a statistical measure of the precision for a set of measurements. From these results, the NS-FOD measures with high accuracy relative to the ion-chamber, having less than 1% difference in mean value, and a t-test value of 0.84, correlating that the distribution of the two sets of measurements between the ion-chamber and NS-FOD are statistically equal. The NS-FOD displayed a higher RSD value of 5.2% compared to the ion-chamber's precise 0.1% value, but is on the same order as the commercially available MOSFET technology at 3.3%, giving reason to average multiple readings from these smaller detectors. However, in the comparison of the MOSFET to the ion-chamber, the average difference was 11.4%, with a t-test value below 0.025. Therefore the null hypothesis was rejected, indicating that there was a statistical difference in the mean of the gold standard ion-chamber measurement and the MOSFET measurement within 95% confidence. In this study, the NS-FOD provides the clear choice in very small detector size for mock *in vivo* dosimetry.

Measurement comparison of the NS-FOD and MOSFET in a 300 cc breast tissue equivalent phantom in the orthovoltage x-ray machine

Table 5: Dose measurements and statistics from the tissue equivalent breast phantom.

Table 2. Dose measurements and statistics from the tissue equivalent breast phantom.		
	<u>Dose (cGy)</u>	
Trial	NS-FOD	MOSFET
1	11.34	9.97
2	12.18	11.75
3	12.18	9.8
4	12.49	10.43
Mean	12.05	10.49
RSD*	4.10%	8.40%
	<i>% Difference to NS-FOD</i>	13.00%
	<i>T-TEST to Ion-Chamber</i>	0.029
*Relative Standard Deviation		

The 300 cc breast tissue equivalent phantom was utilized to provide further comparison of the NS-FOD to a MOSFET detector for a more realistic tissue geometry in the Xrad320. The NS-FOD and MOSFET were inserted into a small cavity on the side of the phantom (**Figure 22B**); no hole on this particular phantom was large enough for the ion-chamber, nor would it be easy to replicate the exact geometry of another adjacent hole analogous to the block tissue study. **Table 5** displays the data and statistics for the dose values recorded, where in this case, the MOSFET was directly compared to the NS-FOD. A 13.0% dose difference between the two detectors was measured, with the NS-FOD besting the MOSFET precision by a factor of two regarding the RSD value, at 4.1% and 8.4%, respectively. Although the t-test value was low with a value of 0.029 between the two detectors, it was still above the 0.025 p-value set for these experiemnts, indicating that these data sets were statistically similar with 95% confidence. It is also worthwhile to note that in the breast phantom, the MOSFET measured lower than the

NS-FOD, where in the tissue block, the MOSFEST measured higher. This is likely due to the accuracy and precision variability combination of the MOSFEST and NS-FOD during the course of these measurements. However, it should be noted that the NS-FOD was able to accurately reproduce the gold-standard ion-chamber values during the head-to-head comparison in the tissue block phantom, as well as the GE-VCT data (see below).

Measurement comparison of the NS-FOD and IC on a body phantom in the GE-VCT

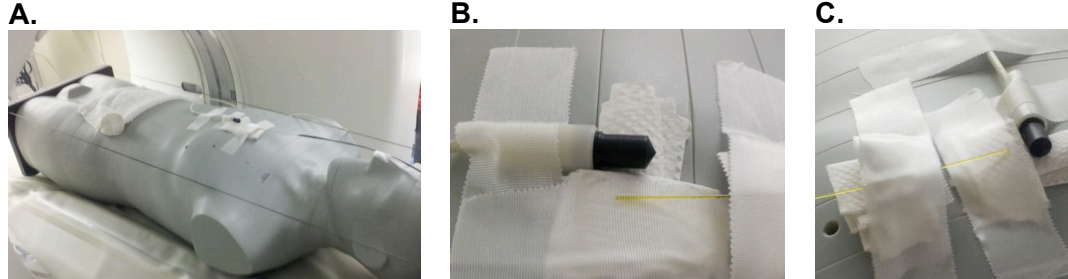


Figure 23: (A) The ATOM adult male anthropomorphic phantom placed on the GE-VCT bed, and close-up images of the parallel (B) and perpendicular (C) placements of the NS-FOD, holding constant the ion-chamber parallel to the bed.

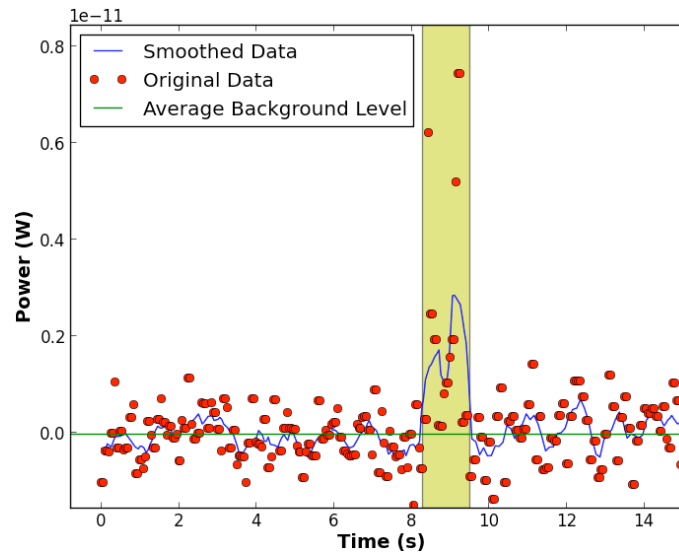


Figure 24: Real-time data acquisition during with the NS-FOD placed parallel to the ion-chamber on the body phantom, comparing scintillation power (W) to time (s). The timing resolution of the NS-FOD enables dose monitoring as the x-ray tube circles the body multiple times, evinced by the two sharp peaks in the original data plot highlighted in the yellow region.

Table 6: Dose measurements and statistics from the tissue equivalent body phantom in a clinical GE-VCT.

Trial	Parallel Dose (cGy)		Perpendicular Dose (cGy)	
	Ion-Chamber	NS-FOD	Ion-Chamber	NS-FOD
1	0.93	1.29	0.95	0.84
2	0.97	0.94	0.94	1.02
3	1.00	0.89	0.93	1.27
4	0.97	0.80	0.93	1.06
5	1.00	0.97	0.95	1.04
Mean	0.97	0.98	0.94	1.04
RSD*	2.8%	19.1%	0.7%	14.7%
<i>% Difference to Ion-Chamber</i>		0.5%	/	11.2%
<i>T-TEST to Ion-Chamber</i>		0.96	/	0.20

*Relative Standard Deviation

To ensure this device functions under more realistic diagnostic applications, a whole body phantom was utilized in a clinical GE-VCT scanner to record point dose on the body surface during a pulmonary embolism diagnostic imaging protocol. The fiber was calibrated free in-air (on a piece of foam) next to the ion-chamber (**Figure 23C**), which was then placed on the sternum of the body in the same “parallel” orientation, with the beam rotating about the central axis (**Figure 23A,B**). An additional set of measurements placed the NS-FOD “perpendicular” to the ion-chamber, to observe if there are any limitations of the NS-FOD with respect to the nano-scintillator tip and beam orientation (**Figure 23C**). **Table 6** shows the acquired point dose data from the sternum of the body phantom, where five measurements were made in each orientation (parallel / perpendicular), and compared to the IC placed in the same position. Once again, these data suggest that the NS-FOD is very accurate with respect to the ion-chamber when aligned in parallel, with less than a 1% difference in measurement and a t-test value of 0.96. Even when aligned perpendicularly, the NS-FOD provided a measurement error of 11.2%, and passed the t-test with a value of 0.20. However, the relative standard deviation was noticeably higher in these experiments; this was likely

caused by the very short time scale of 1-second that the x-ray beam was on, and differences in the tube location during irradiation due to rotation. Using a faster signal rate will easily overcome this in future NS-FOD devices when high-speed is needed.

Figure 24 shows real-time data recorded for parallel trial-3; the original data shows two peaks, with a very sharp valley; this is the real-time dose at the pin-point position from the x-ray tube as the detector is eclipsed by the body phantom tissue. This real-time dose monitoring and total dose measurement combination from the NS-FOD is extraordinary for such a small device, especially with such high accuracy compared the ICs.

5.4 Discussion

In the above results, the NS-FOD has demonstrated the ability to measure radiation dosimetry against the industry standard ion-chamber with sub cGy recording accuracy. These data also suggest that the NS-FOD measures more accurately than the commercially available MOSFET devices relative to the ion-chamber, and provides long-term durability in an even smaller size. The only results that limit this detector currently arise from the parallel versus perpendicular orientation NS-FOD results on the anthropomorphic phantom in the GE-VCT instrument. The data demonstrate however that in moving beam situations, that the incident angle to the detector should remain in the front hemisphere to minimize attenuation artifacts, in this case, as the CT tube rotated 180-degrees behind the nano-scintillator tip. Most instances of radiation imaging and treatment should not pose any concern for this subtle measurement condition, but these capabilities need to be understood to limit false data acquisition.

The nano-scintillator material used displays linearity over broad dose ranges; this material was chosen based on photophysical characterizations that demonstrate this linear response over much further dose and incident energy ranges as shown in Chapter 4. Not only was this material chosen for its linear response, however, but it also displays

an emissive wavelength centered at 611 nm, within the optimum efficiency wavelength range for a small, portable, low-power, and sensitive Si-photodiode that was able to be utilized in this study; simply the combination of highly emissive materials matched to detector efficiency provides the best recipe for a highly sensitive device architecture. An estimated 10 micro-grams or less of nano-scintillator material was used to construct each of the nano-scintillator terminated fibers used in this study, aptly demonstrating the ability of this material to generate light intense enough to be able to have simple photo-sensors be able to read the signal.

It is also worthwhile to note that, to date, these two NS-FOD constructs fabricated herein, plus other prototype detectors using this material, have yet to show any energy or power dependent radiation aging effects, ranging from low flux, low kVp x-ray, to high flux, high energy 662 keV gamma-ray sources. Future experimental plans are being designed to fully test the longevity of a single calibration under different energy regimes and particle types for this purpose. Since the fiber is calibrated for each energy range and radiation particle type, background noise and radiation inherent effects are non-existent to the sensor and or fiber. For instance, Cerenkov radiation has been reported under high-energy x-ray and electron beams, causing distortions of light signal from the fiber,^{108,109} and forcing subsequent corrections to be made in order to accurately present reliable dose measurements.¹¹⁰ In the study presented herein, the NS-FOD was tested at x-ray voltages far-less than the threshold needed to generate the Cerenkov effect, nor did it operate in counting (pulse-height) mode. Furthermore, Cerenkov radiation isn't expected to have any affect on the NS-FOD even at higher x-ray, electron and gamma-ray energies, due to the aforementioned NS-FOD calibration steps, that incorporate any Cerenkov radiation probability at a given energy and radiation particle type.

5.5 Conclusion

In conclusion, a device was presented, the nano-scintillator terminated fiber-optic dosimeter (NS-FOD), that is sub-millimeter in size, responds over broad, medically relevant dose ranges under 120 kVp x-rays, records dosimetry data in real-time, does not show any contrast during diagnostic imaging, is portable and USB powered, and presents long term radiation measuring stability. Not only does the NS-FOD dosimeter directly fit into existing applications for x-ray beam characterization and tissue phantom dose response research, but this platform allows for *in vivo* dosimetry measurements during clinical diagnostic imaging and radiation therapy treatments, with high measurement accuracy proven as measured against the industry standard ion-chamber. The fiber can easily be fit through the smallest of catheters or hypodermic needles to be placed almost anywhere *in vivo*, or, the fiber can be coated with a bio-friendly polymer that can be sterilized and re-used, limiting hospital and patient expenses. Additionally, given the ultra-small size of this device, point dose measurements in distinct areas of interest, from bone marrow to heart chambers, can be realized for the first time with sub cGy accuracy, providing invaluable data to clinicians in limiting radiation exposure and disease onset. The accuracy, durability and stability could further lend this device architecture to field use for general radiation monitoring and national security applications.

Acknowledgement. I would like to thank Matthew D. Belley, Giao Nguyen, Terry T. Yoshizumi, and Michael J. Therien for their contributions to this work. This work was supported, in part, by the Paul M. Gross and Kathleen Zielek Fellowships, the National Institute of Allergy and Infectious Diseases Grant (No. U19 A1067798), and the U.S. NRC Health Physics Fellowship Grant (No. NRC-HQ-12-G-38-0022). I would also like to thank Caroline Lowery, B.S.R.T. (R)(CT) for providing expertise and efforts to acquire CT data in the clinic.

Appendix A. Fluorescence and Raman Spectroscopy of Single-Walled Carbon Nanotubes Helically Wrapped by Ionic, Semiconducting Polymers In Different Dielectric and Electrophilic Environments

A.1 Introduction

Single-walled carbon nanotubes (SWNTs) possess photophysical, electrical and mechanical properties that can be exploited in photovoltaics,¹¹¹⁻¹¹⁴ sensors,¹¹⁵⁻¹¹⁸ and storage media,¹¹⁹ to name a few. These pseudo one-dimensional structures are composed of a single layer of carbon atoms, when can be illustrated as a rolled up sheet of graphene with varying diameters based on their chiral index, (n,m), that defines individual SWNT structural and electronic properties.

The SWNT electronic band-gaps, denoted by electronic transitions E_{ij} , are manifested optically throughout the entire UV-NIR and short-IR wavelength spectrum as measured by absorption spectroscopy, with the lowest energy E_{11} optical transition responsible for the NIR-IR wavelength emissions. Pioneering work of surfactant suspended individualized SWNT emission provided benchmark photophysical data of the individual chiral indices and tube diameters on the E_{11} transition energies,¹²⁰ facilitating the advancement of spectroscopic studies on surfactant¹²¹⁻¹²⁷ and polymer^{113,126,128-133} based dispersions, as well as environmental-dependence^{127,134-137} of SWNT absorption and emission properties. Furthermore, highly developed purification techniques via density gradient centrifugation^{119,138-143} and column chromatography,^{119,143} have made possible the study of individual SWNT electronic and photophysical properties, as well as provide purer materials for future device integration.

When coupled with emission spectroscopy, Resonant Raman spectroscopy provides additional characterization to the individualization and identification of the SWNTs present in the solution sample, as each diameter has a distinctive radial breathing mode (RBM) vibrational-phonon in addition to the classic graphene longitudinal G-band vibrational-phonon.^{133,140,141,144-152} Since the SWNT absorption peak positions shift as a function of their individualization, chiral index and diameter,^{140,145,147,149,152} as well as their E₁₁ emissions having a stoke's shift of only a few nanometers,^{120,153} careful selection of laser lines that overlap with individualized SWNTs in the E₂₂ absorption region allows for the RBM spectra to be measured in the Raman shift region of 100 - 400 cm⁻¹. In addition, since the phonons in SWNTs are, in part, responsible for non-radiative relaxation from E₂₂ excitation to E₁₁ emission,¹⁵⁴ the ability to provide solubilization techniques that don't alter the electronic or vibrational SWNT structure are exceedingly important to investigating and understanding the basic photophysics of these unique materials.

Several methods have been developed to individualize SWNTs for solution phase spectroscopic measurements, each with their own notable advantages and disadvantageous. Noncovalent, aqueous surfactant¹²¹⁻¹²⁷ dispersion is most widely utilized and studied, as its straightforward preparation through commercially available surfactants, sonication of SWNTs in a surfactant solution, and subsequent centrifugation provides well-dispersed SWNTs without altering the intrinsic SWNT electronic properties. There are multiple aqueous and organic based surfactants, with sodium dodecyl sulfate (SDS) and sodium cholate (SC) in aqueous solution being most typical due to their ease of preparation and SWNT dispersion, but unfortunately, surfactant dispersion has shown limited solvent choices based on the surfactant solubility, restricting photophysical studies on SWNT solvent-dependency. Covalent

functionalization of molecules to SWNT surfaces has also been explored,¹⁵⁵⁻¹⁵⁸ but has a shortcoming of breaking the electronic structure of SWNTs by creating defect sites on the SWNT surface. Individual dispersion of SWNTs by polymers has also been studied,^{113,126,128-133} but succumbs to similar limitations on solvents as the surfactant-based solvation routes based on the choice of the polymer. However, the polymer dispersion of individual SWNTs proves that such supramolecular structures can be readily formed, and provides a foundation for designing new supramolecular assemblies that readily enable multi-solvent dispersions without altering inherent SWNT electronic properties.

To this end, the Therien group developed an ionic polymer, poly[p-(2,5-bis(3-propoxysulfonic acid sodium salt))phenylene]ethynylene (PPES),¹⁵⁹ which efficiently dispersed SWNTs in aqueous solution. Atomic force microscopy (AFM) and transmission electron microscopy (TEM) characterization showed that the PPES polymer helically wrapped the SWNTs with a constant pitch length, that was also predicted by molecular dynamic (MD) simulations on the supramolecular structure. The polymer-wrapped SWNTs were approximately 80% individualized at a concentration over a magnitude more than the benchmark SDS-SWNT surfactant suspension. The next generation polymer synthesized, poly[1,5-bis(3-propoxysulfonic acid sodium salt)-2,6-naphthylene]ethynylene (PNES), was also shown to helically wrap individual SWNTs (PNES-SWNT),¹⁶⁰ but more importantly, these PNES-SWNTs were dispersed in both aqueous and organic solvents by use of a phase transfer catalyst, 18-crown-6 ether. PNES-SWNTs were efficiently dispersed in dimethyl sulfoxide (DMSO), dimethylformamide (DMF), and methanol (MeOH) with constant morphology in the various solvent conditions as examined by AFM and TEM, as well as constant excited state lifetimes probed by transient absorption. These solvent-independent lifetimes also matched the benchmark SDS-SWNT values previously recorded, confirming that the

PNES wrapping does not have any electronic distortion effects on the SWNT. By enabling organic dispersion via the PNES polymer and phase transfer catalysts, further solvent-dependent studies on SWNT photophysics were able to be designed, measured, and quantified.⁵⁹

Presented herein is fluorescence spectroscopic analysis on the solvation environment of re-suspended PNES-SWNTs, and Raman spectroscopy of directly suspended PNES-SWNTs in multiple solvents, and was, in part, used in a collaborative publication.⁵⁹ Two-dimensional excitation-emission maps were collected on PNES-SWNT samples that had been originally made in D₂O, dried, and re-suspended in D₂O, as well as in MeOH and DMSO via a phase transfer catalyst similar to the initial PNES-SWNT study, 15-crown-5 ether, to understand the stability of the PNES-SWNT supramolecular compositions in comparison with the samples directly made in those solvents as they were in the publication.⁵⁹ The excitation-emission results of directly suspended and re-suspended PNES-SWNTs were in qualitative accord with each other, showing that the solvent's polarity, as well as the solvent's electrophilicity, play important roles on the emission efficiencies of individualized SWNTs. Raman spectroscopic interrogation of the radial breathing modes of directly suspended PNES-SWNTs showed that there were no changes upon PNES wrapping versus SDS surfactant dispersion in D₂O, and that there were no further changes in the peak positions due to solvent. This Raman spectroscopic data confirms the previous AFM and TEM structural characterizations that the PNES-SWNT supramolecular structure remains constant in different solvent environments, and further does not affect the inherent vibrational structure of SWNTs.

A.2 Experimental

Materials:

Poly[1,5-bis(3-propoxysulfonicacidsodium salt)-2,6-naphthylene]ethynylene (PNES) was synthesized via previous methods.¹⁶⁰ HiPCO SWNTs (Rice Purified, PO342), D₂O (Aldrich, 99.9%), DMF (Acros, extra dry with sieves), methanol (Sigma, Spectroscopic Grade), DMSO (Sigma, 99.9% HPLC grade), and 15-crown-5 ether (Aldrich, 98%) were used as received without further purification.

Solvent Dependent Fluorescence Samples; Re-suspended from D₂O:DMF 9:1.

An initial sample was prepared by adding 7.9 mg of HiPCO SWNTs to 0.5 mL DMF. A solution containing 7.9 mg of PNES in 4.5 mL D₂O was then added to the SWNT and DMF slurry. The combined solution of PNES and SWNTs in D₂O:DMF was tip-sonicated at 5 W for 3 h and then centrifuged at 70,000 g for 3 h, with the top 70% of supernatant collected, leaving behind unsolubilized and bundled SWNTs, amorphous carbon materials, and catalysts (**origD₂O**). Three 1 mL aliquots were separated into vials, dried via rotovap and vacuum, and finally stored in a desiccator for 3 days. Each vial was then capped with a septum. To one vial, 3 mL of D₂O was added (**resD₂O**); to another vial, 3 mL of methanol and 100 μ L of 15-crown-5 ether (Aldrich, 98%) were added (**resMeOH**); to the last vial, 3 mL of DMSO and 100 μ L of 15-crown-5 ether were added (**resDMSO**). Each vial was then bath sonicated for 1 h to re-disperse the PNES-SWNTs. For fluorescence measurements, the solutions were transferred to and from septa-capped cuvettes via syringes to limit any moisture getting into the samples.

Solvent Dependent PNES-SWNT and SDS-SWNT Raman Samples. Three PNES-SWNT samples were produced, one each in D₂O:DMF (made as above), methanol, and DMSO. Approximately 8.3 mg of PNES was dissolved in each solvent, with 100 μ L of 15-crown-5 ether added to the methanol and DMSO samples. Approximately 4.0 mg

of HiPCO SWNTs were then added to each PNES-solvent mixture, tip-sonicated at 5 W for 3 h, and then centrifuged at 70,000 g for 3 h, with the top 70% of supernatant collected. The samples, **PNES-D₂O:DMF**, **PNES-MeOH**, and **PNES-DMSO** were used as prepared. **SDS-D₂O** was prepared by adding 4 mg of HiPCO SWNTs to 5 mL of a 2% w/v SDS solution in D₂O, tip-sonicated at 6.6 W for 1 h, and centrifuged at 70,000 g for 3 h. Post centrifugation, the top 70% of the supernatant was collected and used as prepared.

Instrumentation:

Absorption Spectroscopy. Absorption spectra were recorded on a Shimadzu UV-1700 from 300 - 1100 nm prior to and after fluorescence mapping to ensure no sample degradation occurred.

Excitation-Emission Fluorescence Mapping. 2-dimensional excitation-emission mapping was performed on an Edinburgh Instruments FLSP920 equipped with a 450 W Xe excitation lamp and a Hamamatsu H10330A-75 PMT-module detector. Excitation was measured in 5 nm steps from 540 - 810 nm with a 495 long-pass filter to limit any 2nd-order UV excitation reaching the sample, and emission was recorded in 2 nm steps from 940 - 1500 nm with an integration time of 0.2 sec per point through an 830 nm long-pass filter. Both excitation and emission slits were set to 15 nm bandpass; samples were measured in 3 x 3 mm quartz cuvettes (Starna).

Raman Spectroscopy. The custom built Raman system utilized a PI Acton SP2360i 300 mm spectrograph outfitted with a PI Acton PIXIS 400 BR CCD detector. A Torsana 785XM 785 nm laser diode was utilized for sample excitation and its power density was controlled to 19 mW via a linear neutral density filter wheel. A Semrock Razor Edge Dichroic beamsplitter and a Semrock Razor Edge long-pass laser blocking

optic were employed to direct the excitation light to the sample and filter the laser's Rayleigh scatter from the Raman signal in the collection path to the detector, respectively. As-prepared samples were placed in 1 x 1 cm quartz cuvettes and measured in 180-degree backscattering configuration. All peaks were fit using a Lorentzian fitting package in Igor software; **Figure 25** shows an example fit for the PNES-MeOH sample to determine peak positions.

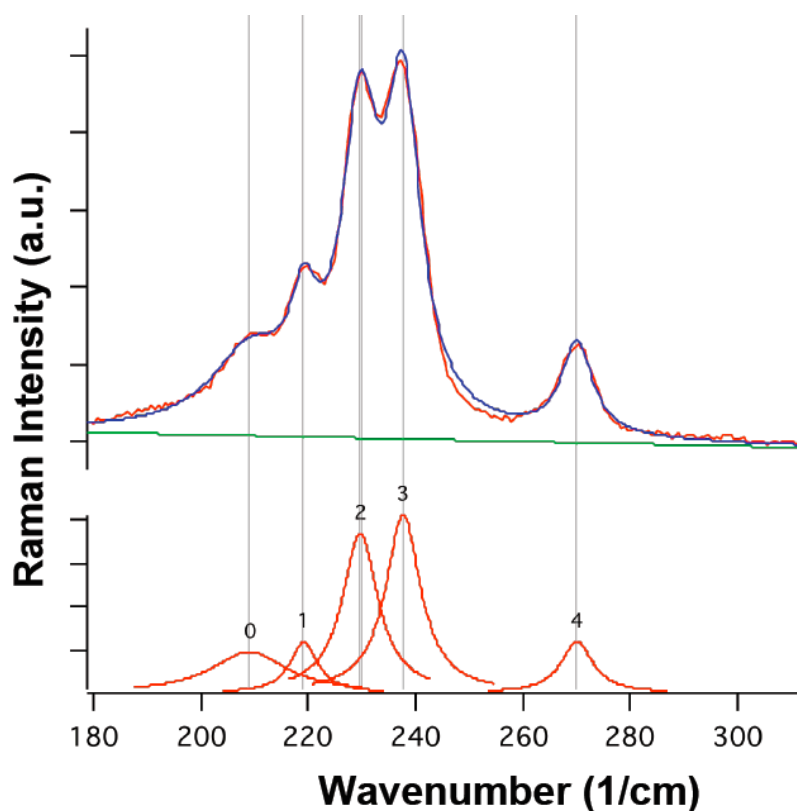


Figure 25: Exemplar Lorentzian fitting of the SWNT radial breathing modes of the PNES-SWNT sample in methanol (PNES-MeOH). The upper plot shows the quality of the fit line (blue) to the recorded data (red) with a linear background baseline (green). The bottom plot shows the individual SWNT radial breath mode fits, whose peak position was utilized for the comparison.

A.3 Results and Discussion

Emission Efficiencies of Re-Suspended Single-Walled Carbon Nanotubes Helically Wrapped by Ionic, Semiconducting Polymers In Different Dielectric and Electrophilic Environments

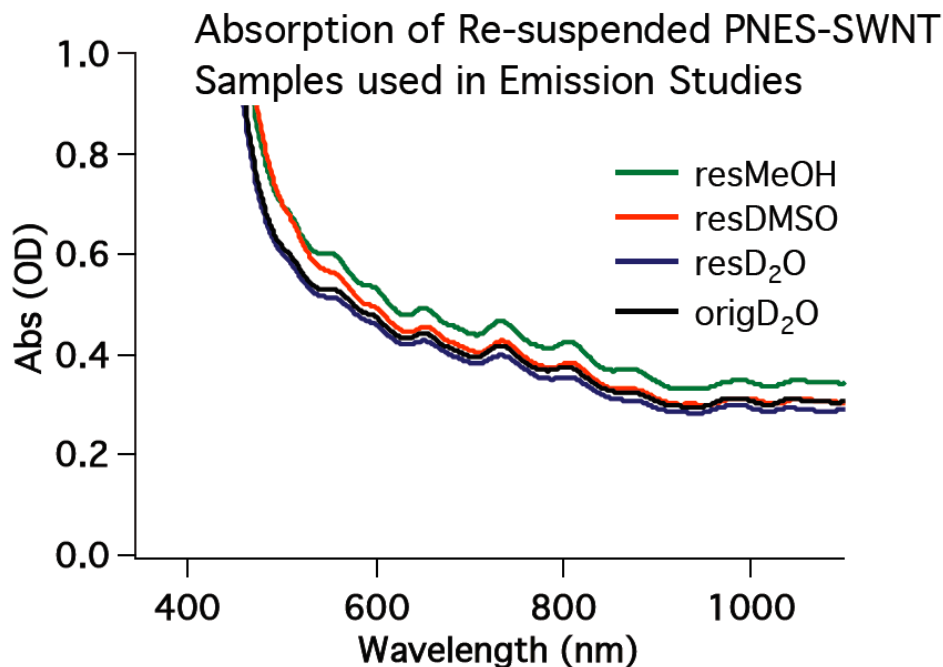


Figure 26: Absorption spectra of the original and re-suspended PNES-SWNT samples used for the two-dimensional excitation-emission mapping.

The absorption spectra of the **origD₂O**, **resD₂O**, **resMeOH**, and **resDMSO** samples are shown in **Figure 26**, and mirror those recorded in the previous detailed study on PNES-SWNTs, showing solvent-induced absorption shifts.¹⁶⁰ The ODs for this study were made nearly identical to assure similar amounts of SWNTs in each solvent for the subsequent fluorescence measurements, and kept at or below 0.6 OD over the SWNT E₂₂ absorption range to minimize inner filter effects. The wavelength region shown in the absorption spectra of **Figure 26** consists of E₂₂ and E₁₁ absorptions at wavelengths greater than 550 nm, with the PNES absorption contributing to the

increased absorbance below 550 nm. Six SWNTs were selected to compare solvent-dependent emission intensities and wavelengths: (7,5), (7,6), (8,4), (9,4), (9,5) and (8,7) SWNTs, whose peak E_{22} absorptions are approximately 650 nm, 655 nm, 595 nm, 735 nm, 685 nm, and 740 nm, respectively. The corresponding SWNT peak OD in each solvent was used to correct the comparative emission intensities for SWNT concentration differences.

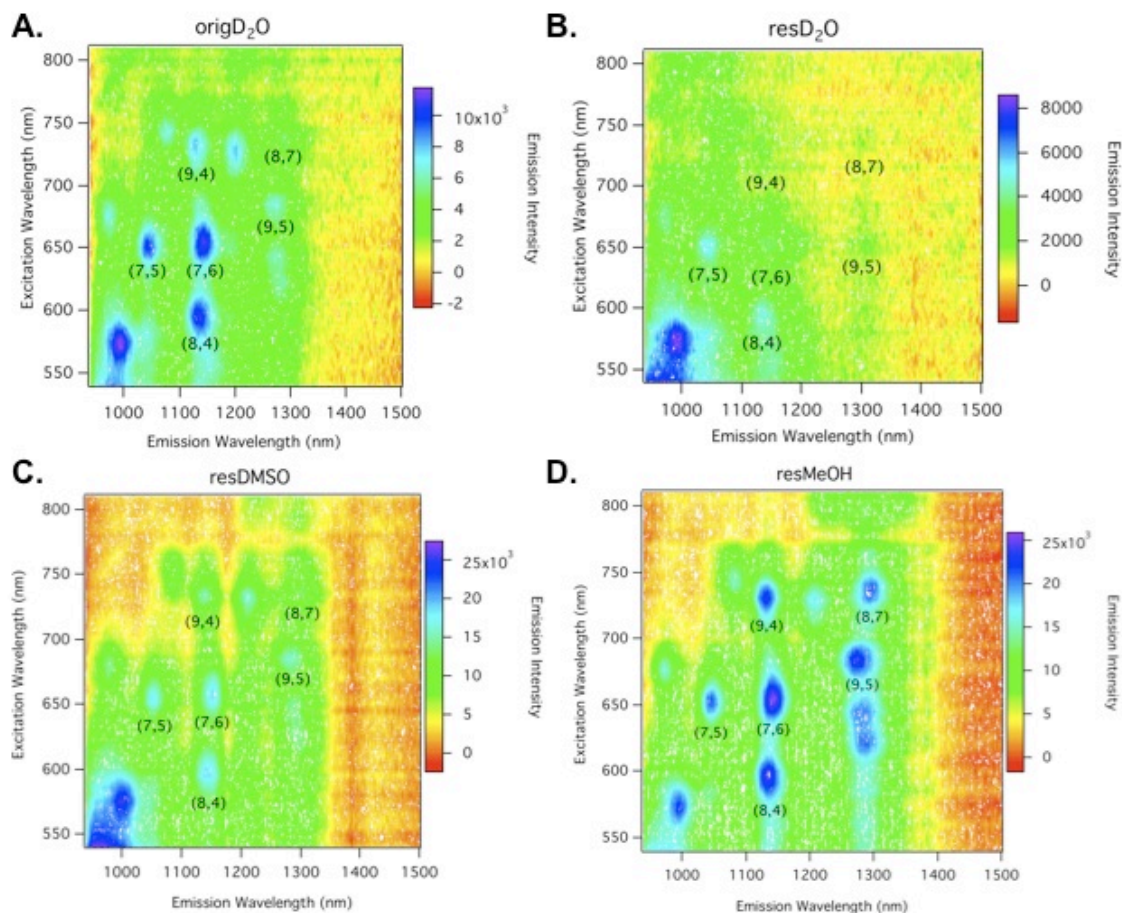


Figure 27: Two-dimensional excitation-emission contour plot mapping of (A) origD₂O, (B) resD₂O, (C) resMeOH, and (D) resDMSO. Individual SWNT species are labeled directly below their peak excitation-emission band. Samples were measured in standard T-geometry luminescence in 3x3 mm cells at room temperature (25 degrees Celsius).

Two-dimensional excitation-emission contour plots of each of the **origD₂O**, **resD₂O**, **resDMSO**, and **resMeOH** samples are shown in **Figure 27A-D**, with individual emission intensity color ranges to highlight the peak positions. Emission spectra were recorded over the range of 940 - 1500 nm as a function of excitation wavelength from 540 - 810 nm, with six SWNTs selected to compare emission intensities labeled directly below their E₂₂-excitation / E₁₁-emission positions. The peak positions and spectral

width are consistent with individualized SWNT emission in solution from surfactant dispersions,¹²¹⁻¹²⁷ with a few nanometer red-shift in peak position from **origD₂O** to other solvents congruent with prior absorption data for PNES-SWNTs in different solvents.¹⁶⁰ From these spectral data, it is clearly seen that the emission from PNES-SWNTs in DMSO and MeOH solutions are markedly more intense than their aqueous counterparts for each of the SWNT species present. **Table 7** shows the data used in further calculations in the comparison of PNES-SWNT solvent-dependent emission efficiency.

Table 7: Tabulated emission efficiencies (I/A) from the excitation (Ex (nm)) and emission (Em (nm)) peaks and their associated optical densities (A (OD)) and emission intensities (Em (I)). Data taken from the absorption spectra and two-dimensional excitation-emission mapping spectra.

resMeOH / SWNT	(7,6)	(7,5)	(8,4)	(9,4)	(9,5)	(8,7)
I/A	1837	3265	4030	9785	1101	4635
Ex (nm)	55	55	95	30	85	35
A (OD)	.49	.49	.536	.466	.454	.466
Em (nm)	146	046	132	132	274	298
Em(I)	5400	1200	3600	3200	3200	0800

resDMSO / SWNT	(7,6)	(7,5)	(8,4)	(9,4)	(9,5)	(8,7)
I/A	0529	0088	7022	4660	8480	0588
Ex (nm)	55	55	95	35	85	30
A (OD)	.454	.454	.497	.427	.421	.425
Em (nm)	146	050	147	136	286	300
Em(I)	8400	8200	8400	4800	6200	3000

resD2O / SWNT	(7,6)	(7,5)	(8,4)	(9,4)	(9,5)	(8,7)
I/A	899	2646	0991	779	557	025
Ex (nm)	50	50	95	35	85	35
A (OD)	.427	.427	.464	.398	.395	.398
Em (nm)	146	042	140	126	298	302
Em(I)	800	400	100	300	800	000

origD2O / SWNT	(7,6)	(7,5)	(8,4)	(9,4)	(9,5)	(8,7)
I/A	4943	2172	2338	8945	7157	3559
Ex (nm)	55	50	95	35	85	40
A (OD)	.441	.442	.479	.417	.408	.413
Em (nm)	142	045	138	130	268	292
Em(I)	1000	800	0700	900	000	600

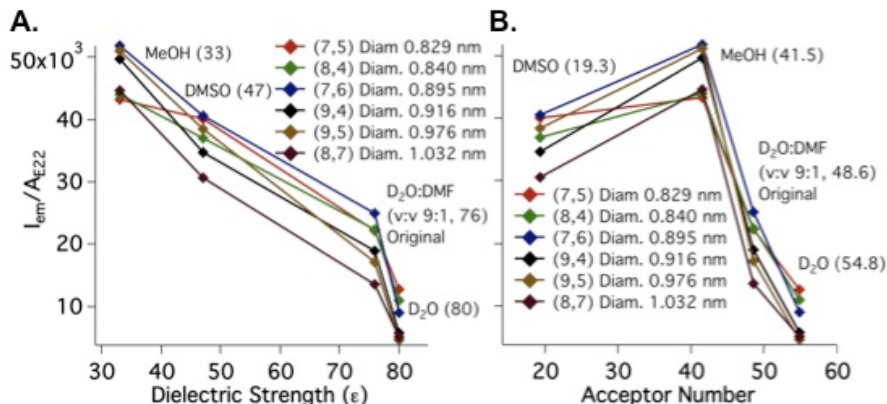


Figure 28: Relative emission efficiencies of the (7,5), (8,4), (7,6), (9,4), (9,5), and (8,7) PNES-SWNTs from the origD₂O, resD₂O, resMeOH, and resDMSO samples plotted as a function of (A) the solvent dielectric constant and (B) the solvent acceptor number. The solid lines in both plots are guides for the eye.

The relative emission efficiencies of the selected SWNT chiralities in each of the origD₂O, resD₂O, resMeOH, and resDMSO samples are presented in **Figure 28** as a function of the solvent dielectric strength and the solvent acceptor number. The emission efficiency is calculated by the ratio of the E₁₁ peak emission intensity to the absorptive optical density at the E₂₂ excitation (I_{em}/A_{E22}) of each SWNT chirality as shown in **Figures 26 and 27, and Table 7**. The general trends of both plots in **Figure 28** show a similar effect on the PNES-SWNT emission efficiencies; as either the solvent dielectric or acceptor number decreases, the PNES-SWNT emission efficiency is significantly augmented. However, neither the solvent dielectric nor the acceptor number of the solvent fully predict the PNES-SWNT dispersion emission efficiency behavior alone, suggesting that multi-mechanism interactions between solvent polarity and electrophilicity play important roles with regard to SWNT emission efficiencies through quenching SWNT photogenerated excited states. These results qualitatively agree with those published for directly suspended PNES-SWNTs in different solvent environments;⁵⁹ though some of the individual PNES-SWNT emission efficiencies as a

function of solvent dielectric and acceptor number do not exactly match point for point with the directly suspended PNES-SWNTs. However, the results presented herein show that the PNES-SWNT supramolecular structure exhibits stability that exceeds the stress of drying and re-suspending from D₂O into different solvents, and follows similar absorption and emission trends to that of directly suspended PNES-SWNTs, maintaining individualized dispersion. The discrepancy between the directly suspended PNES-SWNTs and the re-suspended PNES-SWNTs could be a result of small amounts of residual D₂O leftover in these samples from the drying and re-suspension process that slightly alters parent solvent properties, or from minimal bundling that occurs upon drying and resuspension. Nonetheless, the same mechanisms responsible for the changes in PNES-SWNT emission efficiency as a function of solvent can be deduced.

The enhanced PNES-SWNT emission efficiencies shown by a reduction of solvent dielectric constant are consistent with results previously presented for SWNT-encapsulating micelles in aqueous solution for low (2 - 10) dielectric solvent species.¹³⁷ This solvent dielectric effect has also been seen on other nanoscale materials, such as nanostructured porous silicon.¹⁶¹ In the latter case, the emission intensity decreases with increasing solvent dielectric was ascribed to the increased dielectric screening of the electron-hole Coulombic interaction by solvent molecules that subsequently reduced the emission yields. This same solvent-screening effect is likely the cause of the inverse relationship between PNES-SWNT emission intensity and solvent dielectric, but it is not the only mechanism by which solvents affect the PNES-SWNT emission efficiencies.

It is well published that SWNTs in aqueous dispersions exhibit acid-induced quenching of emission intensity,^{121,153,162,163} ascribed to the electron-withdrawing properties of the present acid. This is caused by protons adsorbed on the SWNT surface that withdraw electron density from the SWNT electronic pi-system, creating defect sites

where nonradiative recombination occurs.¹⁶⁴ **Figure 28B** shows that this effect can also be related to the acceptor number (electrophilicity) of the solvent, and behaves in a similar way to how adsorbed protons on a SWNT surface create surface defects, with the solvent electrophilicity shifting the electron density of the SWNT surface. The solvent dependent dielectric and electrophilic emission efficiency results of the published directly suspended⁵⁹ and re-suspended PNES-SWNTs results herein were the first of their kind to relate these two mechanisms, owing these mechanistic studies to the ability of the PNES polymer to readily individualize SWNTs and, more importantly, for the ability of PNES-SWNTs to be dispersed into multiple dielectric solvents via a phase transfer catalyst.

Raman Spectroscopy of Suspended Single-Walled Carbon Nanotubes Helically Wrapped by Ionic, Semiconducting Polymers In Different Dielectric and Electrophilic Environments

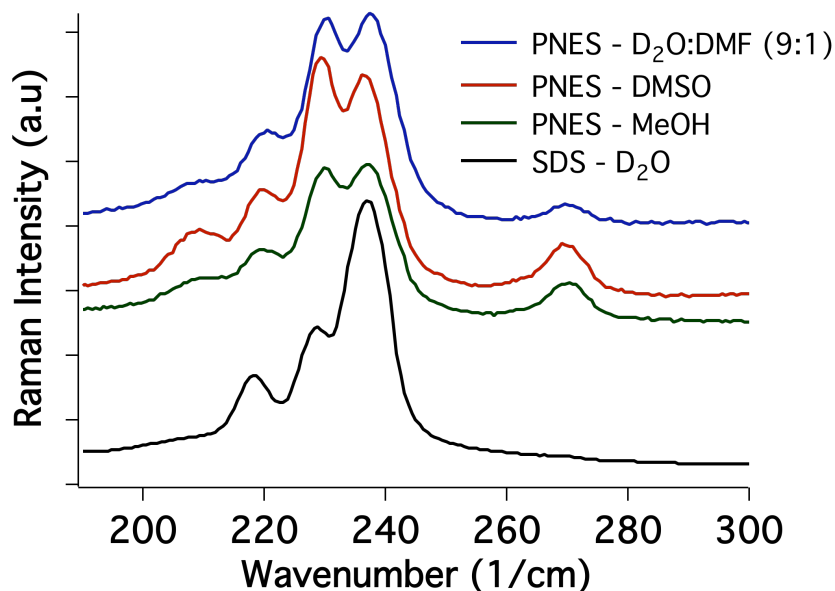


Figure 29: Raman spectra of directly solvent-suspended PNES-SWNTs in D₂O:DMF (PNES-D₂O:DMF), DMSO (PNES-DMSO), and methanol (PNES-MeOH). SDS-surfactant-suspended SWNTs (SDS-D₂O) are also shown and used as the benchmark standard to correlate the radial-breathing mode vibrational frequencies.

Table 8: Solvent-dependent radial-breathing mode (RBM) frequency positions for the 785 nm resonant nanotubes in the PNES and SDS suspended SWNTs. The RBM peak positions show no significant RBM frequency shifts upon PNES wrapping of SWNTs compared to the benchmark SDS surfactant solution, and no further effect on the RBM vibrational frequencies with different solvent environments.

SWNT (n,m)	SDS-D ₂ O RBM (cm ⁻¹)	PNES-D ₂ O RBM (cm ⁻¹)	PNES-DMSO RBM (cm ⁻¹)	PNES-MeOH RBM (cm ⁻¹)
(13,3)	205	208	209	209
(9,7)	218	220	219	219
(10,5)	228	230	229	230
(12,1)	237	238	237	238
(10,2)	269	270	270	270

* +/- 4 cm⁻¹ peak resolution

The Raman spectra of the radial-breathing mode (RBM) vibrational-phonon region of the directly solvent-suspended PNES-SWNTs are shown in **Figure 29**, with the peak positions tabulated in **Table 8**. 785 nm laser excitation was used, as it has sufficient overlap with individualized SWNT E_{22} absorptions,^{145,152} giving a resonance enhancement to those studies in this series. A SDS-SWNT sample prepared in D_2O (**SDS- D_2O**) was utilized as the benchmark standard to interrogate the effect of PNES wrapping on the RBM frequencies. Comparison of the **SDS- D_2O** versus any of the PNES-SWNT samples illustrates that the PNES helical wrapping of SWNTs shows no significant frequency change within the instrument resolution and Lorentzian fitting algorithms upon PNES wrapping versus SDS surfactant dispersion in D_2O , and that there was no further change in the peak positions due to solvent. This Raman data is vitally important to the mechanistic segregation of polymer and solvent effects on the emission efficiency, revealing that the polymer wrapping does not perturb the inherent vibrational SWNT structure and subsequent emission quenching via additional or altered nonradiative vibrational energy loss. These data, exhibiting that the PNES-SWNT supramolecular structure remains constant in different solvent environments, are congruent with the published AFM and TEM results from the initial work on PNES-SWNTs, and further illustrates the PNES-wrapping does not affect inherent vibration-phonons, making the PNES-SWNT structure ideal for conducting fundamental studies on SWNTs, as well as providing individualized SWNTs for potential device applications.

A.4 Conclusion

In conclusion, PNES-SWNTs that were dried and re-suspended in three different solvent environments were interrogated by absorption and two-dimensional excitation-emission spectroscopy. This study served to better understand the stability of the PNES helically wrapped SWNT supramolecular structure and to correlate the emission efficiency as a function of solvent. The PNES-SWNT emission efficiencies were shown to derive from both dielectric (polarity) and acceptor number (electrophilicity), with the solvent-dependent emission efficiencies of re-suspended PNES-SWNT displaying an inverse relationship with regard to both the solvent dielectric and acceptor number. The increase in the solvent dielectric, and subsequent decrease in the PNES-SWNT emission efficiency, can be explained by an increase in dielectric screening of the electron-hole Coulombic interaction and decreasing SWNT emission efficiency, while the increase in acceptor number of the solvent withdraws electron density from the SWNT pi-system, in effect causing defect sites, that reduces the SWNT emission efficiency via nonradiative quenching. While neither of these two solvent property-based quenching mechanisms alone can account for the solvent-dependent PNES-SWNT emission efficiencies, in combination they provide foundational photochemical behavior of individualized SWNTs in solution. The results qualitatively agree with those published for direct solvent-suspended PNES-SWNTs and demonstrate the remarkable stability of these polymer-wrapped SWNTs. Raman spectra comparing directly suspended PNES-SWNTs in D₂O:DMF, DMSO, and MeOH, to a benchmark SDS-SWNT sample, showed no frequency change of the SWNTs radial-breathing mode vibrational-phonon frequency due to polymer wrapping in D₂O:DMF, and no further change in RBM with varying solvents. This data, in addition to previous TEM and AFM results, indicate that the PNES polymer maintains constant wrapping structure in a variety of environments and

does not affect inherent vibrational-phonons, proving it to be superior for conducting fundamental studies on SWNTs as well as provide individualized SWNTs for potential device applications.

Acknowledgement. I would like to thank Mary G. Glesner, Pravas Deria, and Michael J. Therien for their contribution to this work.

Appendix B. Establishing The Absolute Quantum Yield Efficiency of Free Base Tetraphenylporphyrin

The absolute quantum yield determination of free base tetraphenylporphyrin (H_2TPP) in benzene under multiple excitation wavelengths is presented. The results show that the quantum yield values previously measured via the relative method overestimated the quantum yield values for H_2TPP by a factor of 1.6, with the absolute method determining the quantum yield to be 7.0% in aerated benzene at all excitation wavelengths from 405 - 588 nm and 8.7% in de-aerated benzene under 546 nm excitation, establishing H_2TPP as a broad band excitable quantum yield standard. Additionally, solutions of fluorescein, ruthenium tris(2,2'-bipyridyl)ruthenium(II) ($Ru(bipy)_3^{2+}$), and rhodamine 101 were measured to verify that the methods used to measure H_2TPP produce consistent quantum yield results with recent absolute determinations from literature.

B.1 Introduction

The quantum yield efficiency of a molecule, defined as the number of photons emitted versus the number of photons absorbed, is inherently based on the Frank-Condon mediated ground-state and excited-state electronic coupling, manifested through absorptive and emissive oscillator strengths. The significance of a molecule's ability to absorb and emit radiation has unparalleled contributions to almost every field of molecular photonics, from solar cells to medical imaging. As such, quantum yield measurements have been a focus in photophysical characterization for well over half a century,^{65,165-167} and continue to be routinely utilized in the characterization of molecular design and development.

Over this period of research, extensive techniques have been developed to accurately measure the quantum yield of a molecule, which can be separated into direct

(absolute) and relative methods.¹⁶⁷ The relative method has been the most commonly used as it can be done using any fluorescence measurement system, and employs a molecule that has a known quantum yield as the standard to compare to the sample molecule's emission. This method supposes that both molecules absorb about the same amount of incident light at the excitation wavelength as well as emit in the same wavelength regime. By choosing a standard that matches the absorption extinction coefficient of the sample at the incident wavelength, it facilitates a more straightforward quantum yield determination by comparing the integrated emission spectrum of the sample relative to the standard. However, if the standard and sample have vastly different extinction coefficients, concentration effects could cause altered results, either through standard or sample in-homogeneity, such as pi-pi stacking at high concentrations or through self quenching of emission. Further, to enable the best comparison of sample versus standard emissive responses, spectral correction of the instrument's wavelength dependent sensitivity, caused by the instrument's optics and detector response, should be as closely overlapped as possible. This fact is especially true when measuring in wavelength regimes towards the lower sensitivity ranges of the detector in the near-infrared regions, as dark noise from the detector becomes much more apparent. Also, the standard and sample should have quantum yields that are close in efficiency, such that instrument parameters (i.e. slit width, integration time, and excitation intensity) are not changed during the measurements. These previous limitations are typically overcome by the choice of a molecule with known quantum yield that best matches the absorptive and emissive properties of the sample, especially as commercially available fluorescence compounds can be acquired for this purpose. In spite of having a good choice of standard molecules, the relative method's biggest shortcoming is that it relies on the fact that the previous quantum yield measurements of

the standard being used were accurate and precise, as the sample's quantum yield will solely rest on the work of prior research.

Absolute methods of quantum yield determination have been less popular until recently, as they require much more rigor in measurement conditions, system standardization and calibration, advanced system components, and subsequent calculations. The absolute method, however, directly measures the quantum yield through use of an integrating sphere, where every photon transmitted, absorbed, and emitted can be directly accounted for without need of a standard molecule. With the recent advances in integrating sphere technology and coatings, fiber-optics, and compact light sources, all coupled to highly sensitive and broad-band wavelength detection back-thinned CCD (BT-CCD) based spectrometers, absolute quantum yield measurements are now readily accessible with reliable and straightforward data acquisition and processing in a commercially available package from Hamamatsu Photonics.^{60,61} This modern absolute method makes use of a monochromatized Xe-lamp for excitation, fiber-coupled to an integrating sphere as the sample chamber, which is then fiber-coupled to a wavelength intensity corrected BT-CCD based spectrometer for the emission measurement.

Pioneering work by de Mello, Whitmann, and Friend describes a three-position measurement utilized for highly absorbing and scattering samples to accurately account for direct and indirect sample absorption and emission,⁶⁵ which provides the basis for the modern measurements described herein. Given that the measurement of typical fluorescent molecules can be acquired under dilute conditions where scatter and indirect absorption are not significant,^{60,61} only a two-part measurement is needed to accurately measure the quantum yield: a solvent reference, and the sample. First, the reference, composed of just the solvent in the cuvette, is illuminated at the desired excitation

wavelength in the sphere, which provides the integrated intensity of the excitation light with no sample contribution present. Second, the sample, composed of the fluorophore in the same solvent at dilute concentration, is illuminated at the same excitation wavelength and the spectrum is recorded. Absorption by the sample gives rise to a decrease in the integrated excitation relative to the reference, and new peaks are also observed in the spectrum, corresponding to the emission spectrum of the sample. Since the integrating sphere contains all light entered and emitted, the absolute absorption and emission values are directly acquired through spectral separation and integration. Thus, the absolute quantum yield is computed by the difference of the sample's integrated emission to the reference background (absolute emitted photons), divided by the integrated excitation peak of the reference to the integrated excitation peak of the sample (absolute absorbed photons).^{60,61}

Of late, this commercially available method has re-evaluated and confirmed some of the most commonly used relative quantum yield standards; fluorescein, quinine bisulfate, rhodamine 101, anthracene, and 9,10-diphenylanthracene were measured within minimal error to previously published results,^{60,61} and provided a more thorough evaluation of these highly used standards. On the other hand, a universal inorganic molecule for quantum yields, tris(2,2'-bipyridyl)ruthenium(II) ($\text{Ru}(\text{bipy})_3^{2+}$), was shown to have significant deviation from the commonly used value and required correction to its quantum yield.⁶⁰ Wurth *et al.*, from BAM Federal Institute for Materials Research and Testing (the European equivalent of the National Institute of Standards), calculated the error of this commercially available system to be approximately 8% following their own methodology.⁶¹ Some other recent examples that utilized the commercially available absolute quantum yield system are cyclometalated Ir(III) complexes,¹⁶⁸ Ir(III) phenylpyridine derivatives in solution and solid-state films,¹⁶⁹ aromatic hydrocarbon

crystals,¹⁷⁰ and conjugated polymer nanoparticles (pecher),¹⁷¹ further establishing its use across a broad range of materials.

Porphyrins have long been studied due to their biological importance, most notably as active sites in Photosystem-II and as the oxygen-binding heme group in red-blood cells. Consequently, porphyrins have been the topic of a vast amount of research with several books and journals devoted solely to their synthesis and properties (such as “The Porphyrins” by Martin Gouterman, and the *Journal of Porphyrins and Phthalocyanines*). Free base tetraphenylporphyrin (H₂TPP) is among the most notable compounds in the study of porphyrin photophysical properties,^{172,173} as this soluble structure provides the basis for porphyrin related energetics for the further development and interrogation of porphyrin derivatives.¹⁷⁴ Given its stability, solubility, red-shifted fluorescence, commercial availability, and ability to be excited over broad regions of the visible spectrum, it makes an excellent candidate as a quantum yield standard molecule. Seybold and Gouterman measured the quantum yield of H₂TPP at 11% in aerated benzene when excited at 546 nm.¹⁷² Their measurements on H₂TPP were made by the relative method as described in Parker and Rees,¹⁶⁶ using chlorophyll b as the reference standard.¹⁶⁵ Quimby and Longo measured the quantum yield of H₂TPP in de-aerated benzene at 13% under 546 excitation,¹⁷⁵ using the relative method to Seybold and Gouterman’s H₂TPP aerated value of 11% as the standard. For the case of H₂TPP, these same values have been used for over 40 years.¹⁷² While these numbers have now been passed down through literature for years, there has still yet to be an absolute quantum yield determination of this classic fluorescent molecule.

Presented herein is the absolute quantum yield determination of the H₂TPP quantum yield in benzene under multiple excitation wavelengths using a commercially available integrating sphere system. The results show that the quantum yield values

previously measured using the relative method by Seybold and Gouterman overestimated the quantum yield values for H₂TPP by a factor of 1.6, with the absolute method determining the quantum yield to be 7.0% in aerated benzene at all excitation wavelengths from 405 - 588 nm and 8.7% in de-aerated benzene under 546 nm excitation. Additionally, solutions of fluorescein, ruthenium tris(2,2'-bipyridyl)ruthenium(II) (Ru(bipy)₃²⁺), and rhodamine 101 were measured to verify that the methods used produce consistent quantum yield results with recent absolute determinations from literature.^{60,61}

B.2 Experimental

Materials:

H₂TPP in benzene. Free base tetraphenylporphyrin was synthesized using previously described methods.¹⁷⁶ Benzene (Sigma, Chromosolv >99.9%) was freshly passed through basic alumina (Fisher, Brockmann I) before each set of experiments.

Fluorescein in 0.1 N NaOH. Fluorescein (Sigma, free acid) was used without further purification. 0.1 N NaOH was made fresh each day using 99.99% NaOH (Sigma) and HPLC-grade water (Fisher).

Tris(2,2'-bipyridyl)ruthenium(II) (Ru(bipy)₃²⁺) in water. [Ru(bipy)₃](Cl)₂(H₂O)₆ (Sigma, 99.95% Trace Metal Basis) was used without further purification. Fresh [Ru(bipy)₃](Cl)₂(H₂O)₆ was dissolved into HPLC-grade water (Fisher) before each set of experiments.

Rhodamine 101 in ethanol. Rhodamine 101 (Acros, 99% laser grade) was used without further purification. Fresh Rhodamine 101 was dissolved into spectroscopic grade ethanol (Sigma) prior to each measurement.

Instrumentation:

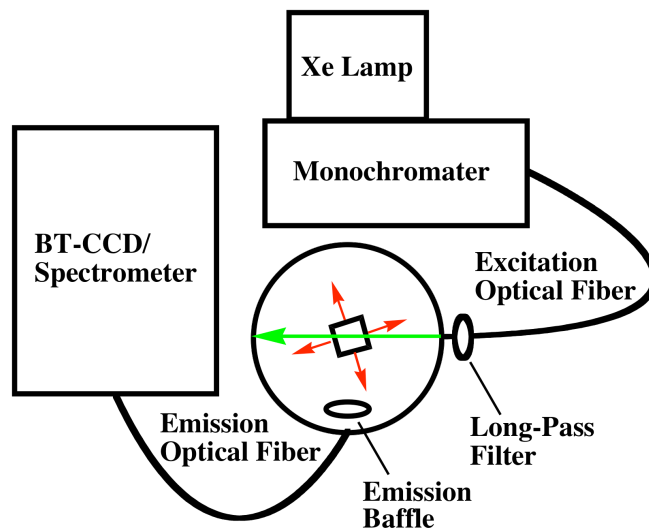


Figure 30: Schematic diagram of the Hamamatsu absolute quantum yield measurement system.

Quantum Yield System. A Hamamatsu C9920-03 Absolute Quantum Yield Measurement System was employed to make the quantum yield measurements. A system diagram is given in **Figure 30**. Excitation initiates from a Xe-lamp, where the wavelength is selected by a monochromator, and passed through a 1 mm optical excitation fiber. If the excitation wavelength used was above 425 nm, a 405 nm long-pass filter was inserted to remove any 2nd order UV light before excitation light entered the sphere (for instance, when exciting H₂TPP at 588 nm, this ensured no 294 nm photons reached the sample for additional excitation). The inside of the sphere is coated with Spectralon (Labsphere, Inc.) that has 99% reflectance from at least 350 – 1650 nm. The light transmitted, light scattered, and emitted light are collected through a second optical fiber protected by a baffle. The baffle ensures that each photon bounces twice within the sphere before being collected, which homogenizes the collected light such that no detected photons are from direct injection of scattered or emitted light into the

fiber. Therefore, the individual signals of the light being detected is truly representative of the distribution of the light within the sphere. The collected light is then sent into a photonic multichannel analyzer (PMA-12) that contains a BT-CCD based spectrometer for light detection. The system response to wavelength and intensity are fully calibrated and corrected based on the output of traceable lamp sources to the National Metrology Institute of Japan.

Quantum Yield Measurement. A dilute stock solution of each sample was made fresh daily. For each sample, at least five sets of four concentrations were measured to show the precision of the methodology. For each set, a low concentration of roughly 0.04 OD at the excitation wavelength was prepared, measured, and subsequently diluted 3 additional times until the final OD was roughly 0.005. Each measurement was checked for absorption prior to measurement to ensure this range. The reference sample of each measurement was a 1 cm cuvette filled with the solvent being used, and the same 1 cm cell was used for the whole set of measurement. **Figure 31** shows a representative set of measurements for 546 nm excitation of H₂TPP.

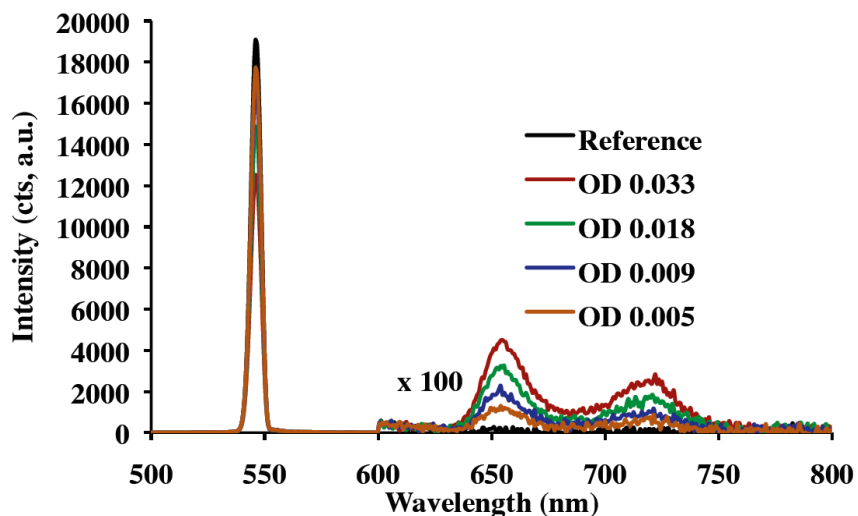


Figure 31: Representative set of measurements for H₂TPP excited at 546 nm. The OD at 546 nm of each sample is listed in the plot. The 600 - 800 nm range has been magnified to easily see the emission and show its decrease in intensity as the concentration decreases. Note that the sample absorption is also evident at 546 nm, as the sample concentration increases, the intensity of light at 546 nm decreases.

Steady State Absorption. Absorption measurements were performed on a Shimadzu UV-1700 spectrophotometer in the same 1 cm quartz cell used for the quantum yield measurements.

Steady State Emission. Steady state emission spectra were recorded on an Edinburgh FLSP920, equipped with a Xe-lamp for excitation and an R2658 PMT (Hamamatsu) for detection, in the same 1 cm quartz cell used for the quantum yield measurements. The emission spectra were corrected for system and detector response using a correction file generated from traceable standard lamps.

B.3 Results and Discussion

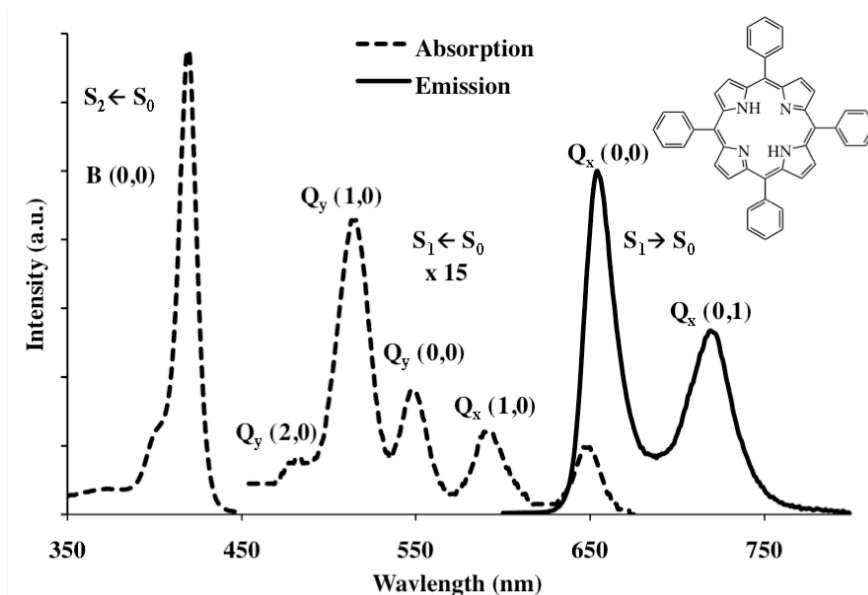


Figure 32: The representative ground state absorption (dashed line) and emission (solid line) spectra synthesized for this study, as well as the molecular structure of H_2TPP . The fluorescence spectra were obtained by 546 nm excitation of the $Q_y(0,0)$ band. The absorption of the Q band region has been magnified by 15 times to show the distinct structure of each Q band.

The representative absorption and emission spectra of H_2TPP are plotted in **Figure 32**. The ground state absorption spectrum of H_2TPP is dominated by two sets of structure, the intense B band (Soret) with a peak centered at 419 nm ($B(0,0)$), and the weaker, highly split Q band, with peak absorptions at 483 nm ($Q_y(2,0)$), 515 nm ($Q_y(1,0)$), 548 nm ($Q_y(0,0)$), 592 nm ($Q_x(1,0)$), and 647 nm ($Q_x(0,0)$), matching well with previously reported values.^{172,173} The large degree of Q band splitting into five peaks is unique to H_2TPP compared to the metalloporphyrins due to the lowering of symmetry into two components of inequivalent energy, Q_x and Q_y , even though both manifest nearly degenerate D_{4h} symmetry. The dominate fluorescent emission in H_2TPP comes from the lowest occupied Q_x band, peaking at 654 nm and 720 nm, corresponding to $Q_x(0,0)$ and $Q_x(0,1)$, respectively, forming the classic mirror image of absorption and

emission spectra. The ultra-fast depopulation to the lowest energy Q bands from higher energy absorptions allows H₂TPP to maintain the same emission regardless of excitation wavelength, as shown by the excitation wavelength independent quantum yields (*vide infra*).

Table 9: Comparisons of quantum yield values of H₂TPP and other standard fluorophores in aerated solvent obtained in this study versus previous literature.

Compound	Solvent	Excitation Wavelength (nm)	Measured Quantum Yield	Literature Reported Quantum Yield
H ₂ TPP	Benzene	546 nm	0.070 (+/- 0.002)	0.11 ¹⁷²
Fluorescein	0.1 N NaOH	460 nm	0.860 (+/- 0.013)	0.88 (+/- 0.03) ⁶⁰
[Ru(bipy) ₃]Cl ₂	Water	436 nm	0.040 (+/- 0.002)	0.04 (+/- 0.002) ⁶⁰
Rhodamine 101	Ethanol	525 nm	0.87 (+/- 0.03)	0.87 - 0.90 ⁶¹

The absolute measured quantum yield of H₂TPP is reported in **Table 9** in comparison to the previous literature results when excited at 546 nm in aerated benzene. To validate our measurement accuracy and repeatability, the absolute quantum yields of fluorescein in 0.1 N NaOH, Ru(bipy)₃²⁺ in water, and rhodamine 101 in ethanol were measured and their values compared to current literature values (**Table 9**). As can be seen, the as measured quantum yield values of 86% for fluorescein, 4% for Ru(bipy)₃²⁺, and 87% for rhodamine 101 agree well with previous work using this system and methodology, and are within experimental error of the literature values. **Figure 33** displays a single concentration example of the absolute quantum yield measurement, showing the reference excitation spectra at 546 nm, as well as H₂TPP absorption at 546 nm and emission from 625 - 775 nm. After much searching, no absolute quantum yield measurements have ever been made on H₂TPP.

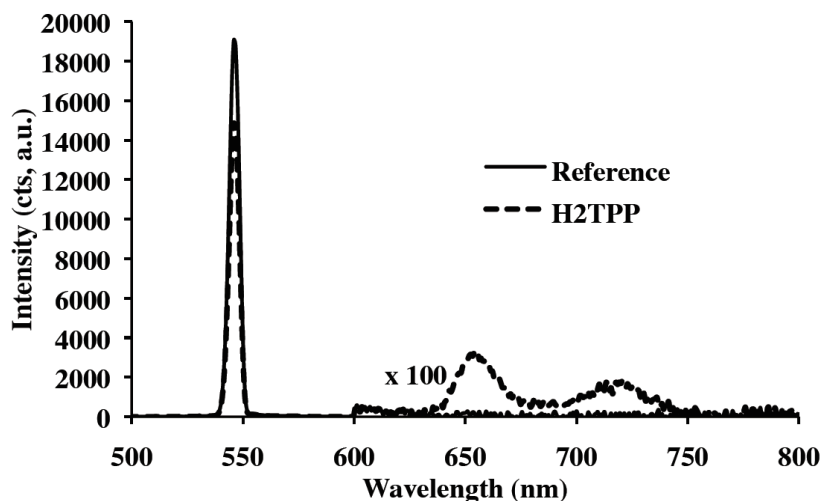


Figure 33: Representative absolute quantum yield measurement of H₂TPP excited at 546 nm. The OD at the excitation wavelength was 0.018. The absorption of H₂TPP at the excitation peak can clearly be seen in the difference of the reference (just benzene solvent) versus the sample, and the region from 600 – 800 nm has been magnified (x 100) to easily see the H₂TPP emission with respect to the background. The high sensitivity of the BT-CCD makes this measurement possible well into the near-infrared.

To establish H₂TPP as a broad-band excitable standard for future use, the absolute quantum yield was measured by exciting into the different absorption bands manifested by this molecule. Excitation wavelengths of 405 nm (B band), 510 nm (Q_y (1,0)), 546 nm (Q_y (0,0)), and 588 nm (Q_x (1,0)) were chosen to demonstrate this property. Since Q_x (0,0) at 647 nm is also the principal emitting state, it does not make good practice to excite into this band for quantum yield purposes to avoid absorption-emission overlap and complicated subtraction techniques. For all of these excitation wavelengths, the quantum yield value remained at 7% (**Table 10**). It is worthwhile to note that while H₂TPP does not display any excitation wavelength quantum yield dependence, the higher symmetry of metalloporphyrins causes different excited state splitting and subsequent relaxation pathways,¹⁷⁷ and excitation wavelength dependent quantum yields have been previously reported even in the simple model metalloporphyrin, zinc tetraphenylporphyrin.¹⁷⁸

Table 10: H₂TPP absolute quantum yields from different excitation wavelengths in aerated benzene.

Excitation Wavelength (nm)	Populated State	Measured Quantum Yield
405	B (0,0)	0.071 (+/- 0.002)
510	Q _y (1,0)	0.069 (+/- 0.001)
546	Q _y (0,0)	0.070 (+/- 0.002)
588	Q _x (1,0)	0.070 (+/- 0.002)
Average		0.070 (+/- 0.002)

The excitation-independent quantum yields of H₂TPP are a result this molecule's ability to rapidly depopulate to the lowest energy excited singlet-state, as clearly shown by Zewail's group using ultrafast upconversion fluorescence and pump-probe spectroscopy on H₂TPP in aerated benzene.¹⁷³ It was found that internal conversion from an initially excited (populated) B band decayed to the Q band within an estimated sub 50 fs timescale, and the subsequent emission from the Q band displayed no detectable rise time within the fluorescence upconversion instrumental resolution of 100 fs, a clear demonstration that internal conversion relaxation from the upper excited B band to the Q band is incredibly rapid. Furthermore, the paralleling transient absorption spectra of the rates and amplitudes of absorption and emission of B band versus Q_y band excitation lead again to the conclusion that the B band depopulation is too rapid to be resolved, and mirrors Q band relaxation. Likewise for any Q_y or Q_x band excitation, vibrational relaxation and solvent-induced relaxation afford a very fast population into the lower lying Q_x states. Since there are no emissive or transient individual lifetimes associated with excitation into each Q band state, it can be predicted that this molecule will display wavelength independent quantum yields, as have been conclusively demonstrated herein.

B.4 Conclusion

In conclusion, the absolute quantum yield of H₂TPP in aerated benzene was measured to be 7.0%. This value is 0.64 times lower than the initially report value over 40 years ago.¹⁷² It is clear that relative methods can propagate error, and these results emphasize the importance of using standards whose quantum yield has been determined or verified through absolute methods. It was also demonstrated that H₂TPP has excitation wavelength independent quantum yields by exciting multiple wavelengths of the B and Q band manifolds. For relative quantum yield methods, this is another necessary consideration when choosing the standard. This study now establishes H₂TPP as a competent standard for use in broad-band relative quantum yield measurements at dilute conditions.

Acknowledgement. I would like to thank Jeff Rawson and Michael J. Therien for their contribution to this work.

References

- (1) Auzel, F. *Chem. Rev.* 2004, 104, 139-173.
- (2) Qian, H. S.; Zhang, Y. *Langmuir* 2008, 24, 12123-12125.
- (3) Kramer, K. W.; Biner, D.; Frei, G.; Gudel, H. U.; Hehlen, M. P.; Luthi, S. R. *Chem. Mater.* 2004, 16, 1244-1251.
- (4) Li, Z. Q.; Zhang, Y. *Nanotechnology* 2008, 19, 345606.
- (5) Mai, H. X.; Zhang, Y. W.; Sun, L. D.; Yan, C. H. *J. Phys. Chem. C* 2007, 111, 13721-13729.
- (6) Renero-Lecuna, C.; Martin-Rodriguez, R.; Valiente, R.; Gonzalez, J.; Rodriguez, F.; Kramer, K. W.; Gudel, H. U. *Chem. Mater.* 2011, 23, 3442-3448.
- (7) Sivakumar, S.; van Veggel, F.; May, P. S. *J. Am. Chem. Soc.* 2007, 129, 620-625.
- (8) Suyver, J. F.; Grimm, J.; Kramer, K. W.; Gudel, H. U. *J. Lumin.* 2005, 114, 53-59.
- (9) Suyver, J. F.; Grimm, J.; van Veen, M. K.; Biner, D.; Kramer, K. W.; Gudel, H. U. *J. Lumin.* 2006, 117, 1-12.
- (10) Boyer, J. C.; van Veggel, F. *Nanoscale* 2010, 2, 1417-1419.
- (11) Auzel, F.; Pecile, D. *J. Lumin.* 1973, 8, 32-43.
- (12) Auzel, F.; Pecile, D. *J. Lumin.* 1976, 11, 321-330.
- (13) Page, R. H.; Schaffers, K. I.; Waide, P. A.; Tassano, J. B.; Payne, S. A.; Krupke, W. F.; Bischel, W. K. *J. Opt. Soc. Am. B* 1998, 15, 996-1008.
- (14) Faulkner, D. O.; Petrov, S.; Perovic, D. D.; Kherani, N. P.; Ozin, G. A. *J. Mat. Chem.* 2012, 22, 24330-24334.
- (15) Wu, S. W.; Han, G.; Milliron, D. J.; Aloni, S.; Altoe, V.; Talapin, D. V.; Cohen, B. E.; Schuck, P. J. *Proc. Natl. Acad. Sci. U. S. A.* 2009, 106, 10917-10921.
- (16) Idris, N. M.; Li, Z. Q.; Ye, L.; Sim, E. K. W.; Mahendran, R.; Ho, P. C. L.; Zhang, Y. *Biomaterials* 2009, 30, 5104-5113.
- (17) Chatterjee, D. K.; Rufaihah, A. J.; Zhang, Y. *Biomaterials* 2008, 29, 937-943.
- (18) Yu, M. X.; Li, F. Y.; Chen, Z. G.; Hu, H.; Zhan, C.; Yang, H.; Huang, C. H. *Anal. Chem.* 2009, 81, 930-935.
- (19) Hilderbrand, S. A.; Shao, F. W.; Salthouse, C.; Mahmood, U.; Weissleder, R. *Chem. Commun.* 2009, 4188-4190.

- (20) Kobayashi, H.; Kosaka, N.; Ogawa, M.; Morgan, N. Y.; Smith, P. D.; Murray, C. B.; Ye, X. C.; Collins, J.; Kumar, G. A.; Bell, H.; Choyke, P. L. *J. Mat. Chem.* 2009, 19, 6481-6484.
- (21) Jalil, R. A.; Zhang, Y. *Biomaterials* 2008, 29, 4122-4128.
- (22) Shan, J. N.; Chen, J. B.; Meng, J.; Collins, J.; Soboyejo, W.; Friedberg, J. S.; Ju, Y. G. *J. Appl. Phys.* 2008, 104, 094308.
- (23) Wang, M.; Abbineni, G.; Clevenger, A.; Mao, C. B.; Xu, S. K. *Nanomed.-Nanotechnol.* 2011, 7, 710-729.
- (24) Xiong, L. Q.; Chen, Z. G.; Yu, M. X.; Li, F. Y.; Liu, C.; Huang, C. H. *Biomaterials* 2009, 30, 5592-5600.
- (25) Xiong, L. Q.; Yang, T. S.; Yang, Y.; Xu, C. J.; Li, F. Y. *Biomaterials* 2010, 31, 7078-7085.
- (26) Jin, J. F.; Gu, Y. J.; Man, C. W. Y.; Cheng, J. P.; Xu, Z. H.; Zhang, Y.; Wang, H. S.; Lee, V. H. Y.; Cheng, S. H.; Wong, W. T. *ACS Nano* 2011, 5, 7838-7847.
- (27) Hu, H.; Xiong, L. Q.; Zhou, J.; Li, F. Y.; Cao, T. Y.; Huang, C. H. *Chem. Eur. J.* 2009, 15, 3577-3584.
- (28) Jiang, S.; Zhang, Y.; Lim, K. M.; Sim, E. K. W.; Ye, L. *Nanotechnology* 2009, 20, 155101.
- (29) Zhou, J.; Liu, Z.; Li, F. Y. *Chem. Soc. Rev.* 2012, 41, 1323-1349.
- (30) Nam, S. H.; Bae, Y. M.; Park, Y. I.; Kim, J. H.; Kim, H. M.; Choi, J. S.; Lee, K. T.; Hyeon, T.; Suh, Y. D. *Angew. Chem. Int. Ed.* 2011, 50, 6093-6097.
- (31) Shan, J. N.; Budijono, S. J.; Hu, G. H.; Yao, N.; Kang, Y. B.; Ju, Y. G.; Prud'homme, R. K. *Adv. Funct. Mater.* 2011, 21, 2488-2495.
- (32) Wang, C.; Tao, H. Q.; Cheng, L.; Liu, Z. *Biomaterials* 2011, 32, 6145-6154.
- (33) Zhou, A. G.; Wei, Y. C.; Wu, B. Y.; Chen, Q.; Xing, D. *Mol. Pharmaceutics* 2012, 9, 1580-1589.
- (34) Salthouse, C.; Hildebrand, S.; Weissleder, R.; Mahmood, U. *Optics Express* 2008, 16, 21731-21737.
- (35) Rodnyi, P. A. *Physical Processes in Inorganic Scintillators* 1ed.; CRC Press, 1997.
- (36) Nikl, M. *Meas. Sci. Technol.* 2006, 17, R37-R54.
- (37) van Eijk, C. W. E. *Phys. Med. Biol.* 2002, 47, R85-R106.
- (38) Ozawa, L.; Itoh, M. *Chem. Rev.* 2003, 103, 3835-3855.

- (39) Duclos, S. J.; Greskovich, C. D.; Lyons, R. J.; Vartuli, J. S.; Hoffman, D. M.; Riedner, R. J.; Lynch, M. J. *Nucl. Instrum. Meth. A.* 2003, 505, 68-71.
- (40) Dai, Q.; Foley, M. E.; Breshike, C. J.; Lita, A.; Strouse, G. F. *J. Am. Chem. Soc.* 2011, 133, 15475-15486.
- (41) Gupta, B. K.; Narayanan, T. N.; Vithayathil, S. A.; Lee, Y.; Koshy, S.; Reddy, A. L. M.; Saha, A.; Shanker, V.; Singh, V. N.; Kaiparettu, B. A.; Marti, A. A.; Ajayan, P. M. *Small* 2012, 8, 3028-3034.
- (42) Wakefield, G.; Holland, E.; Dobson, P. J.; Hutchison, J. L. *Adv. Mater.* 2001, 13, 1557-1560.
- (43) Brown, S. S.; Rondinone, A. J.; Dai, S. In *Antiterrorism and Homeland Defense: Polymers and Materials*; Reynolds, J. G., Lawson, G. E., Koester, C. J., Eds. 2007; Vol. 980, p 117.
- (44) Letant, S. E.; Wang, T. F. *Nano Lett.* 2006, 6, 2877-2880.
- (45) Sun, C.; Pratz, G.; Carpenter, C. M.; Liu, H. G.; Cheng, Z.; Gambhir, S. S.; Xing, L. *Adv. Mater.* 2011, 23, H195-H199.
- (46) Letant, S. E.; Wang, T. F. *Appl. Phys. Lett.* 2006, 88, 103110.
- (47) Dujardin, C.; Amans, D.; Belsky, A.; Chaput, F.; Ledoux, G.; Pillonnet, A. *IEEE T. Nucl. Sci.* 2010, 57, 1348-1354.
- (48) Yoshizumi, T. T.; Goodman, P. C.; Frush, D. P.; Nguyen, G.; Toncheva, G.; Sarder, M.; Barnes, L. *Am. J. of Roentgenol.* 2007, 188, 1332-1336.
- (49) Ehringfeld, C.; Schmid, S.; Poljanc, K.; Kirisits, C.; Aiginger, H.; Georg, D. *Physics in Medicine and Biology* 2005, 50, 289-303.
- (50) Brady, S. L.; Kaufman, R. A. *Med. Phys.* 2012, 39, 3031-40.
- (51) Toncheva, G.; Fredrickson, M.; Yoshizumi, T. T. *Medical Physics* 2010, 37, 3116.
- (52) Pomije, B. D.; Huh, C. H.; Tressler, M. A.; Hintenlang, D. E.; Bolch, W. E. *Health Physics* 2001, 80, 497-505.
- (53) Rowbottom, C. G.; Jaffray, D. A. *Medical Physics* 2004, 31, 609-615.
- (54) Duggan, L.; Budzanowski, M.; Przegietka, K.; Reitsema, N.; Wong, J.; Kron, T. *Radiat. Meas.* 2000, 32, 335-342.
- (55) Yu, C.; Luxton, G. *Medical Physics* 1999, 26, 1010-1016.
- (56) Archambault, L.; Arsenault, J.; Gingras, L.; Beddar, A. S.; Roy, R.; Beaulieu, L. *Medical Physics* 2005, 32, 2271-2278.

- (57) Archambault, L.; Briere, T. M.; Ponisch, F.; Beaulieu, L.; Kuban, D. A.; Lee, A.; Beddar, S. *International Journal of Radiation Oncology Biology Physics* 2010, 78, 280-287.
- (58) Jang, K. W.; Cho, D. H.; Shin, S. H.; Yoo, W. J.; Seo, J. K.; Lee, B.; Kim, S.; Moon, J. H.; Cho, Y. H.; Park, B. G. *Optical Review* 2009, 16, 383-386.
- (59) Larsen, B. A.; Deria, P.; Holt, J. M.; Stanton, I. N.; Heben, M. J.; Therien, M. J.; Blackburn, J. L. *J. Am. Chem. Soc.* 2012, 134, 12485-12491.
- (60) Suzuki, K.; Kobayashi, A.; Kaneko, S.; Takehira, K.; Yoshihara, T.; Ishida, H.; Shiina, Y.; Oishic, S.; Tobita, S. *Phys. Chem. Chem. Phys.* 2009, 11, 9850-9860.
- (61) Wurth, C.; Lochmann, C.; Spieles, M.; Pauli, J.; Hoffmann, K.; Schuttrigkeit, T.; Franzl, T.; Resch-Genger, U. *Appl. Spectrosc.* 2010, 64, 733-741.
- (62) Maestro, L. M.; Rodriguez, E. M.; Vetrone, F.; Naccache, R.; Ramirez, H. L.; Jaque, D.; Capobianco, J. A.; Sole, J. G. *Opt. Express* 2010, 18, 23544-23553.
- (63) Zipfel, W. R.; Williams, R. M.; Webb, W. W. *Nat. Biotechnol.* 2003, 21, 1369-1377.
- (64) Zipfel, W. R.; Williams, R. M.; Christie, R.; Nikitin, A. Y.; Hyman, B. T.; Webb, W. W. *Proc. Natl. Acad. Sci. U. S. A* 2003, 100, 7075-7080.
- (65) deMello, J. C.; Wittmann, H. F.; Friend, R. H. *Adv. Mater.* 1997, 9, 230-232.
- (66) Nyk, M.; Wawrzynczyk, D.; Parjaszewski, K.; Samoc, M. *J. Phys. Chem. C* 2011, 115, 16849-16855.
- (67) *American National Standard for Safe Use of Lasers*, ANSI Z136.1-2000 (American National Standard Institute, Orlando, FL, 2000).
- (68) Ye, T.; Zhao, G. W.; Zhang, W. P.; Xia, S. D. *Materials Research Bulletin* 1997, 32, 501-506.
- (69) Tessari, G.; Bettinelli, M.; Speghini, A.; Ajo, D.; Pozza, G.; Depero, L. E.; Allieri, B.; Sangaletti, L. *Applied Surface Science* 1999, 144-45, 686-689.
- (70) Polizzi, S.; Fagherazzi, G.; Battagliarin, M.; Bettinelli, M.; Speghini, A. *Journal of Materials Research* 2001, 16, 146-154.
- (71) Cho, J. Y.; Do, Y. R.; Huh, Y. D. *Applied Physics Letters* 2006, 89, 131915.
- (72) Bai, X.; Song, H. W.; Pan, G. H.; Lei, Y. Q.; Wang, T.; Ren, X. G.; Lu, S. Z.; Dong, B.; Dai, Q. L.; Fan, L. *J. Phys. Chem. C* 2007, 111, 13611-13617.
- (73) Yi, S. S.; Bae, J. S.; Moon, B. K.; Jeong, J. H.; Park, J. C.; Kim, I. W. *Applied Physics Letters* 2002, 81, 3344-3346.
- (74) Cavouras, D.; Kandarakis, I.; Panayiotakis, G. S.; Evangelou, E. K.; Nomicos, C. *D. Med. Phys.* 1996, 23, 1965-1975.

- (75) Yi, S. S.; Shim, K. S.; Yang, H. K.; Moon, B. K.; Choi, B. C.; Jeong, J. H.; Kim, J. H.; Bae, J. S. *Appl. Phys. A-Mater. Sci. Process.* 2007, 87, 667-671.
- (76) Bae, J. S.; Yoon, J. H.; Park, S. K.; Kim, J. P.; Jeong, E. D.; Won, M. S.; Jeong, J. H.; Shim, K. S.; Yang, H. K.; Yi, S. S. *Surface Review and Letters* 2007, 14, 535-538.
- (77) Buchanan, R. A.; Wickersheim, K. A.; Weaver, J. L.; Anderson, E. E. *J. Appl. Phys.* 1968, 39, 4342-4347.
- (78) Anh, T.; Benalloul, P.; Barthou, C.; Giang, L. T.; Vu, N.; Minh, L. J. *Nanomater.* 2007, 48247.
- (79) Kapoor, R.; Friend, C. S.; Biswas, A.; Prasad, P. N. *Optics Letters* 2000, 25, 338-340.
- (80) Vetrone, F.; Boyer, J. C.; Capobianco, J. A.; Speghini, A.; Bettinelli, M. *Journal of Applied Physics* 2004, 96, 661-667.
- (81) Chen, G. Y.; Liu, H. C.; Liang, H. J.; Somesfalean, G.; Zhang, Z. G. *J. Phys. Chem. C* 2008, 112, 12030-12036.
- (82) Yang, L. M.; Song, H. W.; Yu, L. X.; Liu, Z. X.; Lu, S. H. *Journal of Luminescence* 2006, 116, 101-106.
- (83) Miyakawa, T.; Dexter, D. L. *Phys. Rev. B* 1970, 1, 2961.
- (84) Yamada, N.; Shionoya, S.; Kushida, T. *J. Phys. Soc. Jap.* 1972, 32, 1577-1586.
- (85) Kaur, G.; Singh, S. K.; Rai, S. B. *Journal of Applied Physics* 2010, 107.
- (86) Chen, G. Y.; Liu, H. C.; Somesfalean, G.; Sheng, Y. Q.; Liang, H. J.; Zhang, Z. G.; Sun, Q.; Wang, F. P. *Applied Physics Letters* 2008, 92, 113114.
- (87) Bai, Y. F.; Wang, Y. X.; Peng, G. Y.; Yang, K.; Zhang, X. R.; Song, Y. L. *Journal of Alloys and Compounds* 2009, 478, 676-678.
- (88) Yeh, S. M.; Su, C. S. *Mat. Sci. and Eng., B* 1996, 38, 245-249.
- (89) Yi, S. S.; Bae, J. S.; Shim, K. S.; Jeong, J. H.; Park, J. C.; Holloway, P. H. *Applied Physics Letters* 2004, 84, 353-355.
- (90) Abrams, B. L.; Holloway, P. H. *Chemical Reviews* 2004, 104, 5783-5801.
- (91) Kumar, R.; Nyk, M.; Ohulchanskyy, T. Y.; Flask, C. A.; Prasad, P. N. *Advanced Functional Materials* 2009, 19, 853-859.
- (92) Wickline, S. A.; Lanza, G. M. *Journal of Cellular Biochemistry* 2002, 87, 90-97.
- (93) Prasad, P. N. *Introduction to Biophotonics*; Wiley: New York, 2003.

- (94) Carpenter, C. M.; Sun, C.; Pratz, G.; Rao, R.; Xing, L. *Medical Physics* 2010, 37, 4011-4018.
- (95) Sun, C.; Pratz, G.; Carpenter, C. M.; Liu, H. G.; Cheng, Z.; Gambhir, S. S.; Xing, L. *Advanced Materials* 2011, 23, H195-H199.
- (96) Stanton, I. N.; Ayres, J. A.; Therien, M. J. *Dalton Trans.* 2012, 41, 11576-11578.
- (97) Repelin, Y.; Proust, C.; Husson, E.; Beny, J. M. *J. Solid State Chem.* 1995, 118, 163-169.
- (98) Ray, S.; Pramanik, P.; Singha, A.; Roy, A. *J. Appl. Phys.* 2005, 97, 094312.
- (99) Tallant, D. R.; Seager, C. H.; Simpson, R. L. *J. Appl. Phys.* 2002, 91, 4053-4064.
- (100) Berger, M. J.; Hubbell, J. H.; Seltzer, S. M.; Chang, J.; Coursey, J. S.; Sukumar, R.; Zucker, D. S.; Olsen, K. *XCOM: Photon Cross Section Database (version 1.5)* 2010, Available: <http://physics.nist.gov/xcom>. National Institute of Standards and Technology, Gaithersburg, MD.
- (101) Attix, F. H. *Introduction to Radiological Physics and Radiation Dosimetry*; John Wiley & Sons, Inc., 1986.
- (102) Dawson, L. A.; Jaffray, D. A. *J. Clin. Oncol.* 2007, 25, 938-946.
- (103) Klein, D.; Briere, T. M.; Kudchadker, R.; Archambault, L.; Beaulieu, L.; Lee, A.; Beddar, S. *Radiat. Meas.* 2012, 47, 921-929.
- (104) Archambault, L.; Briere, T. M.; Ponisch, F.; Beaulieu, L.; Kuban, D. A.; Lee, A.; Beddar, S. *Int. J. Radiat. Oncol.* 2010, 78, 280-287.
- (105) Archambault, L.; Arsenault, J.; Gingras, L.; Beddar, A. S.; Roy, R.; Beaulieu, L. *Med. Phys.* 2005, 32, 2271-2278.
- (106) Tao, S. Q.; Jayaprakash, A. *Optics Letters* 2009, 34, 3244-3246.
- (107) De Lin, M.; Toncheva, G.; Nguyen, G.; Kim, S.; Anderson-Evans, C.; Johnson, G. A.; Yoshizumi, T. T. *Radiat. Res.* 2008, 170, 260-263.
- (108) Beddar, A. S.; Mackie, T. R.; Attix, F. H. *Physics in Medicine and Biology* 1992, 37, 925-935.
- (109) Justus, B. L.; Falkenstein, P.; Huston, A. L.; Plazas, M. C.; Ning, H.; Miller, R. W. *Appl. Optics* 2004, 43, 1663-1668.
- (110) Guillot, M.; Gingras, L.; Archambault, L.; Beddar, S.; Beaulieu, L. *Medical Physics* 2011, 38, 2140-2150.
- (111) Bindl, D. J.; Safron, N. S.; Arnold, M. S. *ACS Nano* 2010, 4, 5657-5664.

- (112) Ferguson, A. J.; Blackburn, J. L.; Holt, J. M.; Kopidakis, N.; Tenent, R. C.; Barnes, T. M.; Heben, M. J.; Rumbles, G. *J. Phys. Chem. Lett.* 2010, 1, 2406-2411.
- (113) Ham, M.-H.; Paulus, G. L. C.; Lee, C. Y.; Song, C.; Kalantar-zadeh, K.; Choi, W.; Han, J.-H.; Strano, M. S. *ACS Nano* 2010, 4, 6251-6259.
- (114) Holt, J. M.; Ferguson, A. J.; Kopidakis, N.; Larsen, B. A.; Bult, J.; Rumbles, G.; Blackburn, J. L. *Nano Lett.* 2010, 10, 4627-4633.
- (115) Barone, P. W.; Baik, S.; Heller, D. A.; Strano, M. S. *Nature Mater.* 2005, 4, 86-92.
- (116) Barone, P. W.; Parker, R. S.; Strano, M. S. *Anal. Chem.* 2005, 77, 7556-7562.
- (117) Balasubramanian, K.; Burghard, M. *Small* 2005, 1, 180-192.
- (118) Heller, D. A.; Jin, H.; Martinez, B. M.; Patel, D.; Miller, B. M.; Yeung, T.-K.; Jena, P. V.; Hobartner, C.; Ha, T.; Silverman, S. K.; Strano, M. S. *Nature Nanotech.* 2009, 4, 114-120.
- (119) Park, H.; Afzali, A.; Han, S.-J.; Tulevski, G. S.; Franklin, A. D.; Tersoff, J.; Hannon, J. B.; Haensch, W. *Nature Nanotech.* 2012, 7, 787-791.
- (120) Weisman, R. B.; Bachilo, S. M. *Nano Lett.* 2003, 3, 1235-1238.
- (121) Blackburn, J. L.; McDonald, T. J.; Metzger, W. K.; Engtrakul, C.; Rumbles, G.; Heben, M. J. *Nano Lett.* 2008, 8, 1047-1054.
- (122) Jones, M.; Engtrakul, C.; Metzger, W. K.; Ellingson, R. J.; Nozik, A. J.; Heben, M. J.; Rumbles, G. *Phys. Rev. B* 2005, 71, 115426/1-115426/9.
- (123) Ju, S.-Y.; Kopcha, W. P.; Papadimitrakopoulos, F. *Science* 2009, 323, 1319-1323.
- (124) McDonald, T. J.; Blackburn, J. L.; Metzger, W. K.; Rumbles, G.; Heben, M. J. *J. Phys. Chem. C* 2007, 111, 17894-17900.
- (125) McDonald, T. J.; Engtrakul, C.; Jones, M.; Rumbles, G.; Heben, M. J. *J. Phys. Chem. B* 2006, 110, 25339-25346.
- (126) Nish, A.; Hwang, J.-Y.; Doig, J.; Nicholas, R. J. *Nature Nanotech.* 2007, 2, 640-646.
- (127) Strano, M. S.; Moore, V. C.; Miller, M. K.; Allen, M. J.; Haroz, E. H.; Kittrell, C.; Hauge, R. H.; Smalley, R. E. *J. Nanosci. Nanotechnol.* 2003, 3, 81-86.
- (128) Engtrakul, C.; Davis, M. F.; Gennett, T.; Dillon, A. C.; Jones, K. M.; Heben, M. J. *Proc. SPIE-Int. Soc. Opt. Eng.* 2005, 5929, 59290L/1-59290L/6.
- (129) Hwang, J. Y.; Nish, A.; Doig, J.; Douven, S.; Chen, C. W.; Chen, L. C.; Nicholas, R. J. *J. Am. Chem. Soc.* 2008, 130, 3543-3553.

- (130) Lebedkin, S.; Hennrich, F.; Kiowski, O.; Kappes, M. M. *Phys. Rev. B* 2008, 77, 165429/1-165429/8.
- (131) O'Connell, M. J.; Boul, P.; Ericson, L. M.; Huffman, C.; Wang, Y.; Haroz, E.; Kuper, C.; Tour, J.; Ausman, K. D.; Smalley, R. E. *Chem. Phys. Lett.* 2001, 342, 265-271.
- (132) Star, A.; Stoddart, J. F.; Steuerman, D.; Diehl, M.; Boukai, A.; Wong, E. W.; Yang, X.; Chung, S. W.; Choi, H.; Heath, J. R. *Angew. Chem., Int. Ed.* 2001, 40, 1721-1725.
- (133) Yi, W.; Malkovskiy, A.; Chu, Q.; Sokolov, A. P.; Lebron Colon, M.; Meador, M.; Pang, Y. J. *Phys. Chem. B* 2008, 112, 12263-12269.
- (134) Choi, J. H.; Strano, M. S. *Appl. Phys. Lett.* 2007, 90, 223114.
- (135) Fagan, J. A.; Huh, J. Y.; Simpson, J. R.; Blackburn, J. L.; Holt, J. M.; Larsen, B. A.; Walker, A. R. H. *ACS Nano* 2011, 5, 3943-3953.
- (136) Ohno, Y.; Iwasaki, S.; Murakami, Y.; Kishimoto, S.; Maruyama, S.; Mizutani, T. *Phys. Status Solidi B* 2007, 244, 4002-4005.
- (137) Silvera-Batista, C. A.; Wang, R. K.; Weinberg, P.; Ziegler, K. J. *Phys. Chem. Chem. Phys.* 2010, 12, 6990-6998.
- (138) Arnold, M. S.; Green, A. A.; Hulvat, J. F.; Stupp, S. I.; Hersam, M. C. *Nature Nanotech.* 2006, 1, 60-65.
- (139) Ghosh, S.; Bachilo, S. M.; Weisman, R. B. *Nature Nanotech.* 2010, 5, 443-450.
- (140) Jiang, J.; Saito, R.; Gruneis, A.; Chou, S. G.; Samsonidze, G. G.; Jorio, A.; Dresselhaus, G.; Dresselhaus, M. S. *Phys. Rev. B* 2005, 71.
- (141) Jorio, A.; Pimenta, M. A.; Souza Filho, A. G.; Saito, R.; Dresselhaus, G.; Dresselhaus, M. S. *New J. Phys.* 2003, 5, 1-17.
- (142) Moshhammer, K.; Hennrich, F.; Kappes, M. *Nano. Res.* 2009, 2, 599-606.
- (143) Komatsu, N.; Wang, F. *Materials* 2010, 3, 3818-3844.
- (144) Bachilo, S. M.; Strano, M. S.; Kittrell, C.; Hauge, R. H.; Smalley, R. E.; Weisman, R. B. *Science* 2002, 298, 2361-2366.
- (145) Doorn, S. K.; Heller, D. A.; Barone, P. W.; Usrey, M. L.; Strano, M. S. *Appl. Phys. A* 2004, 78, 1147-1155.
- (146) Dresselhaus, M. S.; Dresselhaus, G.; Jorio, A.; Souza Filho, A. G.; Pimenta, M. A.; Saito, R. *Acc. Chem. Res.* 2002, 35, 1070-1078.
- (147) Heller, D. A.; Barone, P. W.; Swanson, J. P.; Mayrhofer, R. M.; Strano, M. S. *J. Phys. Chem. B* 2004, 6905-6909.

- (148) Izard, N.; Penicaud, A.; Anglaret, E. *Mater. Res. Soc. Symp. Proc.* 2005, 858E, HH11.1.1.
- (149) Kalbac, M.; Kavan, L.; Dunsch, L. *J. Phys. Chem. C* 2009, 113, 1340-1345.
- (150) Luo, Z. T.; Papadimitrakopoulos, F.; Doorn, S. K. *Phys. Rev. B* 2007, 75.
- (151) Luo, Z. T.; Papadimitrakopoulos, F.; Doorn, S. K. *Phys. Rev. B* 2008, 77, 035421.
- (152) O'Connell, M. J.; Sivaram, S.; Doorn, S. K. *Phys. Rev. B* 2004, 69, 235415.
- (153) O'Connell, M. J.; Bachilo, S. M.; Huffman, C. B.; Moore, V. C.; Strano, M. S.; Haroz, E. H.; Rialon, K. L.; Boul, P. J.; Noon, W. H.; Kittrell, C.; Ma, J. P.; Hauge, R. H.; Weisman, R. B.; Smalley, R. E. *Science* 2002, 297, 593-596.
- (154) Htoon, H.; O'Connell, M. J.; Doorn, S. K.; Klimov, V. I. *Phys. Rev. Lett.* 2005, 94.
- (155) Chen, J.; Hamon, M. A.; Hu, H.; Chen, Y. S.; Rao, A. M.; Eklund, P. C.; Haddon, R. C. *Science* 1998, 282, 95-98.
- (156) Guo, Z.; Du, F.; Ren, D.; Chen, Y.; Zheng, J.; Liu, Z.; Tian, J. *J. Mater. Chem.* 2006, 16, 3021-3030.
- (157) Zhang, X.-F.; Cui, X.; Liu, Q.; Zhang, F. *ChemPhysChem* 2008, 9, 1514-1518.
- (158) Karousis, N.; Tagmatarchis, N.; Tasis, D. *Chem. Rev.* 2010, 110, 5366-5397.
- (159) Kang, Y. K.; Lee, O.-S.; Deria, P.; Kim, S. H.; Park, T.-H.; Bonnell, D. A.; Saven, J. G.; Therien, M. J. *Nano Lett.* 2009, 9, 1414-1418.
- (160) Deria, P.; Sinks, L. E.; Park, T.-H.; Tomezsko, D. M.; Brukman, M. J.; Bonnell, D. A.; Therien, M. J. *Nano Lett.* 2010, 10, 4192-4199.
- (161) Fellah, S.; Ozanam, F.; Gabouze, N.; Chazalviel, J. N. *Phys. Status Solidi A* 2000, 182, 367-372.
- (162) Dukovic, G.; White, B. E.; Zhou, Z. Y.; Wang, F.; Jockusch, S.; Steigerwald, M. L.; Heinz, T. F.; Friesner, R. A.; Turro, N. J.; Brus, L. E. *J. Am. Chem. Soc.* 2004, 126, 15269-15276.
- (163) Strano, M. S.; Huffman, C. B.; Moore, V. C.; O'Connell, M. J.; Haroz, E. H.; Hubbard, J.; Miller, M.; Rialon, K.; Kittrell, C.; Ramesh, S.; Hauge, R. H.; Smalley, R. E. *J. Phys. Chem. B* 2003, 107, 6979-6985.
- (164) Wang, F.; Dukovic, G.; Knoesel, E.; Brus, L. E.; Heinz, T. F. *Phys. Rev. B* 2004, 70, 1-4.
- (165) Weber, G.; Teale, F. W. J. *Trans. Faraday Soc.* 1957, 53, 646-655.
- (166) Parker, C.; Rees, W. *Analyst* 1960, 85, 587-600.

- (167) Demas, J. N.; Crosby, G. A. *J. Phys. Chem.* 1971, 75, 991-1024.
- (168) Sajoto, T.; Djurovich, P. I.; Tamayo, A. B.; Oxgaard, J.; Goddard, W. A.; Thompson, M. E. *J. Am. Chem. Soc.* 2009, 131, 9813-9822.
- (169) Endo, A.; Suzuki, K.; Yoshihara, T.; Tobita, S.; Yahiro, M.; Adachi, C. *Chem. Phys. Lett.* 2008, 460, 155-157.
- (170) Katoh, R.; Suzuki, K.; Furube, A.; Kotani, M.; Tokumaru, K. *J. Phys. Chem. C* 2009, 113, 2961-2965.
- (171) Pecher, J.; Huber, J.; Winterhalder, M.; Zumbusch, A.; Mecking, S. *Biomacromolecules* 2010, 11, 2776-2780.
- (172) Seybold, P. G.; Gouterman, M. *J. Mol. Spectrosc.* 1969, 31, 1-13.
- (173) Baskin, J. S.; Yu, H. Z.; Zewail, A. H. *J. Phys. Chem. A* 2002, 106, 9837-9844.
- (174) Duncan, T. V.; Susumu, K.; Sinks, L. E.; Therien, M. J. *J. Am. Chem. Soc.* 2006, 128, 9000-9001.
- (175) Quimby, D. J.; Longo, F. R. *J. Am. Chem. Soc.* 1975, 97, 5111-5117.
- (176) Adler, A. D.; Longo, F. R.; Finarelli, J. D.; Goldmacher, J.; Assour, J.; Korsakoff, L. *J. Org. Chem.* 1967, 32, 476-476.
- (177) Yu, H. Z.; Baskin, J. S.; Zewail, A. H. *J. Phys. Chem. A* 2002, 106, 9845-9854.
- (178) Karolczak, J.; Kowalska, D.; Lukaszewicz, A.; Maciejewski, A.; Steer, R. P. *J. Phys. Chem. A* 2004, 108, 4570-4575.

Biography

I was born in Plattsburgh, N.Y., to Hal and Mary Ellen Stanton, on November 5th, 1984. I graduated from Plattsburgh Senior High School in 2003, and pursued a Bachelor of Science degree in Chemistry, with a Physics minor, at St. Michael's College in Burlington, Vermont. Upon undergraduate graduation in 2007, I began my graduate studies in Chemistry at the University of Pennsylvania in Philadelphia, Pennsylvania, under Prof. Dr. Michael J. Therien, who moved his research group to Duke University in Durham, North Carolina, in 2008, where I conducted the work presented in this dissertation. While at Duke University, I was awarded the Paul M. Gross and Kathleen Zielek Fellowships, and the Duke Chemistry Departmental Award for "...whose efforts serve as an example of how graduate students can work together to share and spread knowledge throughout the department," by Warren S. Warren, Departmental Chair at the time. The scientific articles and patents I have published or contributed to, to date, include;

Publications

1. **Stanton, I. N.**; Ayres, J. A.; Therien, M. J., Dual Energy Converting Nano-Phosphors; Upconversion Luminescence and X-Ray Excited Scintillation from a Single-Composition of Lanthanide-doped Yttrium Oxide. *Dalton Transactions* 2012, 41, 11576.
2. Larsen, B. A.; Deria, P.; Holt, J. M.; **Stanton, I. N.**; Heben, M. J.; Therien, M. J.; Blackburn, J. L. Effect of Solvent Polarity and Electrophilicity on Quantum Yields and Solvchromatic Shifts of Single-Walled Carbon Nanotube Photoluminescence. *Journal of the American Chemical Society* 2012, 134, 12485 - 12491.
3. Badea, C. T.; **Stanton, I. N.**; Johnston, S. M.; Johnson, G. A.; Therien, M. J., Investigations on x-ray luminescence CT for small animal imaging. *Proc. SPIE Medical Imaging* 2012, 8313, 83130T
4. Lebedeva, N. V.; Schmidt, R. D.; Concepcion, J. J.; Brennaman, M. K.; **Stanton, I. N.**; Therien, M. J.; Meyer, T. J.; Forbes, M. D. E., Structural and pH Dependence of Excited State PCET Reactions involving Reductive Quenching of the MLCT Excited State of $[\text{Ru-II}(\text{bpy})_2(\text{bpz})]^{2+}$ by Hydroquinones. *Journal of Physical Chemistry A* 2011, 115, 3346-3356.

Selected Patents

1. Linear-Response Nanocrystal Scintillators and Methods of Using the Same. **I. N. Stanton**, T. T. Yoshizumi, M. J. Therien. US2013/031372, *International Patent Application*, March 2013.
2. Phosphors and Scintillators for Light Stimulation within a Medium. Z. Fathi, H. Walder, F. A. Bourke, Jr., **I. N. Stanton**, J. A. Ayres, M. J. Therien, M. W. Dewhirst, J. A. Herbert, D. R. Fels, *United States Patent Applied For*, March 2012.
3. Adhesive Bonding Composition and Method of Use. Z. Fathi, H. Walder, F. A. Bourke, Jr., **I. N. Stanton**, J. A. Ayres, J. T. Stecher, M. J. Therien, E. Toone, D. Gooden, M. W. Dewhirst, J. A. Herbert, D. R. Fels, K. S. Hansen, *United States Patent Applied For*, May 2011.
4. Up and Down Conversion Systems for Improved Solar Cell Performance or Other Energy Conversion. F. A. Bourke, Jr., H. Walder, Z. Fathi, **I. N. Stanton**, and M. J. Therien, *United States Patent Applied For*, September 2010.
5. Plasmon-Enhanced Photospectral Therapy. T. Vo-Dinh, J. P Scaffidi, V. G. R. Chada, B. Lauly, Y. Zhang, M. K. Gregas, **I. N. Stanton**, J. T. Stecher, M. J. Therien, F. A. Bourke, Jr., Z. Fathi, J. A. Ayres, Z. Zhang, J. H. Simmons, and S. J. Norton, *United States Patent Applied For*, April 2010.
6. Up and Down Conversion Systems for Production of Emitted Light from Various Energy Sources Including Radio Frequency, Microwave Energy, and Magnetic Induction Sources for Upconversion. T. Vo-Dinh, J. P Scaffidi, V. G. R. Chada, B. Lauly, Y. Zhang, M. K. Gregas, **I. N. Stanton**, J. T. Stecher, M. J. Therien, F. A. Bourke, Jr., Z. Fathi, J. A. Ayres, Z. Zhang, and J. H. Simmons, *United States Patent Applied For*, March 2010.
7. Up and Down Conversion Systems for Production of Emitted Light from Various Energy Sources Including Radio Frequency, Microwave Energy, and Magnetic Induction Sources for Upconversion. T. Vo-Dinh, J. P Scaffidi, V. G. R. Chada, B. Lauly, Y. Zhang, M. K. Gregas, **I. N. Stanton**, J. T. Stecher, M. J. Therien, F. A. Bourke, Jr., and Z. Fathi, *United States Patent Applied For*, November 2009.
8. Up and Down Conversion Systems for Production of Emitted Light from Respective Lower and Higher Energy Activation Sources. T. Vo-Dinh, J. P Scaffidi, V. G. R. Chada, B. Lauly, Y. Zhang, M. K. Gregas, **I. N. Stanton**, J. T. Stecher, M. J. Therien, and F. A. Bourke, Jr., *United States Patent Applied For*, March 2009.

Two oral presentations, and one poster presentation, was also presented during my graduate studies;

Oral Presentations

1. *Material and Device Properties of a Nanocrystal Based Radiation Detector*, Domestic Nuclear Detection Office - National Science Foundation Academic Research Initiative Meeting, Washington, DC, 2012
2. *Upconversion Luminescence and X-Ray-Excited Optical Luminescence (XEOL) of Lanthanide-Doped Yttrium Oxide Nanocrystals*, American Chemical Society National Meeting, Boston, 2010

Poster Presentation

1. *A sub-millimeter, nano-material based fiber-optic device for in/ex vivo radiation dosimetry; linear accelerator x-ray and electron beam validation*, Joint Workshop - Technology for Innovation in Radiation Oncology, Natcher Conference Center, National Institutes of Health, Bethesda, MD, June, 2013